AlO_x Based Thin Films Synthesized by Mist-CVD and Applied as a Gate Insulating Layer in the Field-Effect Transistors

(Mist-CVD 法によるAlO_x膜の合成と電界効果トランジスタゲート絶縁膜への応用)

A Dissertation Submitted to the Graduate School of Science and Engineering of Saitama University in Candidacy for the Degree of Doctor of Philosophy

By

Arifuzzaman Rajib

Recommended for Acceptance by the Department of Functional Materials Science

Supervisor: Hajime Shirai

September 2021

© Copyright by Arifuzzaman Rajib, 2021

All rights Reserved

Dedication

When I came to Japan as a doctoral student, the world was calm but busy. But, when I am writing this thesis, the COVID 19 pandemic has covered our community. It was really burdensome to do anything when you get such a piece of news every moment that thousands of people are dying globally due to the Corona virus.

I dedicate this work to the healthcare workers and researchers who are still working to defeat the pandemic. No "thank you" could ever be enough for what you all are doing at this time of difficulty by dedicating your own lives for the sake of others, for the betterment of the world. All the gratitude to you, the Heroes the Frontliners…..

Abstract

Mist chemical vapor deposition (Mist-CVD) deposited metal oxide thin films as dielectric materials and wide-bandgap semiconductors have been extensively studied. This study was carried out toward reducing the driving voltage and high transconductance in metal-oxide-semiconductor field-effect transistor (MOS-FET) devices and for their relevance in power electronics, solar cells, and photodetectors. Because mist-CVD takes the benefits of solution process and CVD system, facilitating the production of a well-controlled thin film using an environmental-friendly mist-CVD technique. In this thesis, AlO_x was chosen as a model metal oxide as dielectric layer for such applications because of its wide bandgap, high breakdown field, high passivation ability of c-Si, and good thermal stability. The bandgap and dielectric constant also can be controlled by adding guest metal oxide. In this study, TiO_2 was added as a guest metal oxide with AlO_x formed $Al_{1-x}Ti_xO_y$ to improve the dielectric constant but let off some barrier height for the application of metal insulator semiconductor field effect transistors (MIS-FET).

Most studies of thin films using the mist-CVD focus on the synthesis of crystalline thin films on sapphire by adjusting the deposition condition and device performance. On the other side, the amorphous metal oxide thin film as an insulating layer is more preferable to fabricate MIS-FET. However, few studies on the growth mechanism and role of solvent in the synthesis of metal oxide thin films using mist CVD have been performed. To this aim, the following items have been studied in this thesis.

a) Role of H_2O in the synthesis of amorphous AlO_x using mist-CVD

In this work, the effect of H_2O in the synthesis of amorphous AlO_x using atmospheric pressure mist-CVD from aluminum acetylacetonate $Al(acac)_3$ as source material and CH_3OH/H_2O as the solvent system has been studied. The incorporation of -OH groups into the AlO_x network that is fabricated from $Al(acac)_3$ and using solely methanol as a solvent, generates both malformed Al(OH) network and nonuniformity. But the addition of a small amount of water in the solvent during film growth, though decreases the deposition rate due to the hydrogen bond in water molecules but markedly removes -OH groups from the growth surface of the AlO_x network and improves the surface uniformity and refractive index. The effect of exposing these films to H_2O or

CH_3OH mists after fabrication was also assessed to understand the surface chemistry on the growth surface. The feature is that the Al(OH) absorption peaks, for AlO_x films with CH_3OH solvent alone, decreased markedly together with increase AlO_6 octahedron related peaks by increasing the H_2O mist exposure period, suggesting that H_2O mist removed OH bonds near the surface with etched several mono layers. On the other side, no change appeared in the FT-IR and AFM for the AlO_x with CH_3OH:H_2O ratio of 7:3 even after 40 minutes H_2O exposure. For the case of CH_3OH mist exposure, the OH absorption band appeared together with larger surface roughness for AlO_x with CH_3OH:H_2O ratio of 7:3, suggesting that the CH_3OH mist is the source of OH group and the H_2O mist acts as a scavenger to the OH near the growing surface of AlO_x network. The AlO_x thin films grown with CH_3OH:H_2O ratio of 7:3 at 400 °C exhibits a recombination velocity of 16 cm/s, a breakdown field of 6.9 MV/cm, and the interface trap density of 4.2×10^{10} $cm^{-2}eV^{-1}$ which is compatible with the AlO_x grown by the other vacuum-based method.

b) Synthesis of AlO_x thin films monitored by a fast-scanning mobility particle analyzer

In this topic, the effect of deposition parameters on the film properties of mist-CVD a-AlO_x films from aluminum acetylacetonate ($Al(acac)_3$) and CH_3OH/H_2O mixture (=7:3 volume ratio) is demonstrated. Different deposition parameters, such as the flow rate of dilution gas (N_2) (F_d), furnace temperature (T_f), solution concentration, and mesh bias (V_m) were optimized via the analysis of the size distribution of mist precursors using a fast-scanning mobility particle analyzer. The film morphology, the rigidity of the AlO_x network, and junction property at the AlO_x/n-type crystalline Si (n-Si) were dominated by the size distribution of the mist precursors determined by the deposition parameters. Further, the mesh bias supply during film growth promoted the miniaturization of the size distribution of the charged mist particles. Consequently, a marked increase in the number density of the mist particles resulted in an increased refractive index (n) of the AlO_x thin films with small surface roughness values. Furthermore, such property of the AlO_x films improved the junction property at the AlO_x/n-Si interface. In this study, the correlation between the size distribution of mist particles, which is dependent on the deposition parameters, and the film and interface properties, is presented together with MIS-FET performance for the AlO_x thin films obtained by mist-CVD. By adjusting the mesh bias of 9 kV, the interface trap density

for AlO_x/n-Si metal-oxide-semiconductor capacitor can be reduced to 9.5×10^9 $cm^{-2}eV^{-1}$, and the fixed charge density can be increased by 5.1×10^{12} $cm^{-2}eV^{-1}$. Field-effect mobility of 41.4 cm^2/(V s) was obtained, with a threshold voltage of 2.75 V and an on/off ratio of 10^7, using a mechanically exfoliated $MoSe_2$ flake as a channel layer, which is compatible with the AlO_x grown by the other vacuum-based method.

c) Synthesis of mist-CVD $Al_{1-x}Ti_xO_y$ thin films improved the dielectric properties

The large bandgap dielectric material is essential to suppress the charge injection from electrodes into dielectrics that cause leakage current. On the other side, the dielectric material with a high dielectric constant is important to scall down the device size. The trade-off between these two properties is clearly noticed. One effective proposal for balancing between κ and E_g is employing aluminum titanium oxide [$((Al_2O_3)_{1-x}TiO_2)_x$] ($Al_{1-x}Ti_xO_y$) with intermediate properties of Al_2O_3(κ ~9, E_g~ 7 eV) and TiO_2(κ ~50, E_g ~3 eV). As a third topics, we investigated the synthesis of amorphous aluminum titanium oxide $Al_{1-x}Ti_xO_y$ thin films from Al(acac)$_3$ and Ti(acac)$_4$ mixture using CH_3OH/H_2O as a solvent by mist chemical vapor deposition (mist CVD) for application as a high dielectric material. The Ti composition ratio x in the $Al_{1-x}Ti_xO_y$ thin films depends on the Al(acac)$_3$ and Ti(acac)$_4$ mixing ratios as well as CH_3OH/H_2O volume ratio. A bandgap energy of $Al_{1-x}Ti_xO_y$ films was decreased from 6.38 to 4.25 eV and the surface roughness also decreased when the Ti composition ratio was increased from 0 to 0.54. The capacitance-voltage plot revealed that the dielectric constant of $Al_{1-x}Ti_xO_y$ thin films increased from 6.23 to 25.12. Consequently, $Al_{1-x}Ti_xO_y$ thin films with a bandgap energy of 5.12 eV and a dielectric constant of 13.8 were obtained by adjusting the ratio x of 0.26. This $Al_{0.74}Ti_{0.26}O_y$ layer was applied as a gate dielectric layer for the metal-insulator-semiconductor field-effect transistors (MIS-FETs) using a mechanically exfoliated two-dimensional (2D) transition metal dichalcogenide (TMDC), $MoSe_2$, and As-doped WSe_2 flakes as a channel layer. The $MoSe_2$ based MIS-FETs with source/drain gold electrodes exhibit n-channel behavior with a field-effect mobility of 85 cm^2/ (V·s), a threshold voltage of 0.92 V, and an on/off ratio of ~10^6. As-doped WSe_2 based MIS-FETs with source/drain platinum electrodes also showed an ambipolar behavior, which was applied for use in logic applications. These findings suggest that $Al_{0.74}Ti_{0.26}O_y$ by mist CVD is promising as a high-k material for TMDC based MIS-FETs.

Acknowledgments

First, I would like to express my profound gratitude to my supervisor, Professor Hajime Shirai who selected me as a doctoral student and gave me the chance to make this thesis under his supervision. I am very much thankful for his scholastic guidance, advice, and countless discussions throughout the research work.

Besides my supervisor, I express my deepest thank from the core of my heart to Professor Keiji Ueno for the fruitful suggestion, discussion, and take me as his own student when I used his laboratory during this tenure.

I would like to thank the rest of my thesis committee: Professor Masamichi Sakai, Professor Keiji Ueno, and Professor Kenji Kamishima for reviewing my thesis.

I would like to thank all former and current members of Prof. Shirai and Ueno lab: A. T. M. Saiful Islam, Enamul Karim, Takanori Kuroki, daisuke Harada, Rayato Takahashi, Yuma Moriya, Koki Kawamura, Yuki Nasuno, Koki Imai, Kazusi Shimomura, Kojun Yokoyama, Ryota Sato, Ryuichi Ukai, Yoshikazu Ikeno, Yuya Urushido, Ryotaro Kizaki, Sora Sakai, Hirotaka Tokuta, Tomohiro Hirai for their support and create a nice environment for research. I also want to thank Mrs. Tomohiro Shida and Daisuke Akane for helping me to fabricate Metal Insulator Semiconductor Field Effect Transistor (MIS-FET) and Mr. Yosuke Machida for Atomic Force Microscope (AFM) measurement. Besides them, no thank could be enough for Abdul kuddus for how much help he has given during my research journey.

I am also indebted to Assistant Professor Dr. Ryo Ishikawa for his suggestions during my experiment and weekly meeting. I am also thankful to all staff of the Department of Functional Materials Science, Saitama University for their support. Especial thank goes to Izumi Inomori, Foreign Student Office (FSO) for conveying any information about pandemic or university facilities during my staying in Saitama.

I must acknowledge the generosity of all funding agencies. This study was partially supported by a Japan Science and Technology Agency (JST) grant, a Grant-in-Aid for Scientific Research from the Ministry of Education, Culture, Sports, Science and

Technology (MEXT) of Japan. I am also grateful to MEXT for the scholarship for my Ph.D. program at Saitama University.

I would like to thank Assistant Professor Shunji Kurosu, Toyo University (present Osaka University), Kawagoe campus, for allowing me to use SEM and EDS machines and teach me how to analyze and characterize. A deep thanks to K. Funato of Tokyo Direc. Co. Ltd. For allowing me to use their Fast-Scanning Mobility Particle Analyzer.

In the end, I want to acknowledge my family members from the bottom of my heart. No gratitude could not be enough to express their dedication that they have been given to look after me from the day I came to this universe. Finally, I would like to thank my all friends and well-wishers who live in Japan or Bangladesh, or anywhere in the world for their support and share my bad time during my research.

List of Publications and Presentations

Article Publications

1) **A. Rajib**, A. Kuddus, K. Yokoyama, T. Shida, K. Ueno, and H. Shirai, "*Mist chemical vapor deposition of $Al_{1-x}Ti_xO_y$ thin films and their application to a high dielectric material*" ACS Applied Materials and Interfaces, under review, 2021.

2) A. Kuddus, **A. Rajib**, K. Yokoyama, T. Shida, K. Ueno, and H. Shirai, "*Mist Chemical Vapor Deposition of Crystalline MoS2 Atomic Layer Films for Field-Effect Transistors*" Nanotechnology, under review, 2021.

3) **A. Rajib**, A. Kuddus, T. Shida, K. Ueno, and H. Shirai, "*Mist Chemical Vapor Deposition of AlO_x Thin Films Monitored by a Scanning Mobility Particle Analyzer and its Application to the Gate Insulating Layer of Field-effect Transistors*" ACS Applied Electronic Materials **3**, 2, 658-667 (2021) https://dx.doi.org/10.1021/acsaelm.0c00758

4) **A. Rajib**, M. E. Karim, T. Ukai, S. Kurosu, M. Tokuda, Y. Fujii, Y. Nakajima, T. Hanajiri, R. Ishikawa, K. Ueno, and H. Shirai, "*Synthesis of AlO_x thin films by atmospheric-pressure mist chemical vapor deposition for effects on junction properties at the AlO_x/Si interface*" Journal of Vacuum Science and Technology **A 38**, 033413 (2020).

5) A.T.M. S. Islam, M. E. Karim, **A. Rajib,** Y. Nasuno, T. Ukai, S. Kurosu, M. Tokuda, Y. Fujii, Y. Nakajima, T. Hanajiri, H. Shirai, "*Chemical mist deposition of organic for efficient front- and back- PEDOT:PSS/crystalline Si heterojunction solar cells*", Applied Physics Letters**, 114**, 193901 (2019). https://doi.org/10.1063/1.5096579

Conference Presentations

1) A. Kuddus, **A. Rajib**, R. Kizaki, K. Yokoyama, K. Ueno, H. Shirai "*Synthesis of 2D* MoS_2 *and* $WS_{1-x}Se_x$ *thin films by Mist-CVD*" The 82nd JSAP Autumn Meeting, September 10-13, 2021, Online, Japan.

2) K. Yokoyama, **A. Rajib**, A. Kuddus, T. Shida, K. Ueno, and H. Shirai "*Effect of mesh bias supply during synthesis of AlOx and TiOx thin films by a mist chemical vapor deposition*" The 82nd JSAP Autumn Meeting, September 10-13, 2021, Online, Japan.

3) **A. Rajib**, A. Kuddus, T. Shida, K. Yokoyama, K. Ueno, and H. Shirai "$Al_{1-x}Ti_xO_y$ Thin Films Synthesized by Mist-CVD and Applied as a Gate Insulating Layer" The 68th JSAP Spring Meeting, March 16-19, 2021, Tokyo, japan.

4) A. Kuddus, **A. Rajib**, K. Shimomura, K. Yokoyama, K. Ueno, H. Shirai "*Digitalized Mist-Chemical Vapor Deposition of atomic-layer Molybdenum Disulfide* (MoS_2) *Flakes at Low Temperatures*" The 68th JSAP Spring Meeting, March 16-19, 2021, Tokyo, japan.

5) **A. Rajib**, A. Kuddus, K. Enamul, S. Kurosu, T. Ukai, M. Tokuda, Y. Fujii, T. Hanajiri, R. Ishikawa, K. Ueno, and H. Shirai, "*The role of water in the synthesis of* AlO_x *thin films by a mist chemical vapor deposition*", The 67th JSAP Spring Meeting, March 12-15, 2020, Tokyo, japan.

6) **A. Rajib**, A. Kuddus, T. Shida, K. Ueno, and H. Shirai, "Mist-CVD of AlO_x thin films monitored by fast scanning mobility particle analyzer and its application to FETs" The 30th Materials Research Meeting, December 9-11, 2020, Yokohama, Japan.

7) **A. Rajib**, T. Shida, A. Kuddus, K. Ueno, and H. Shirai, "*Synthesis of* AlO_x *thin films by mist-CVD and its application to dielectric layer for MIS-FET*" The 51st The Society of Chemical Engineers SCEJ Autumn Meeting, September 24-26, 2020, Japan.

8) Md E. Karim, **A. Rajib**, Y. Nasuno, T. Ukai, S. Kurosu, M. Tokuda, Y. Fujii, T. Hanajiri, R. Ishikawa, K. Ueno, H. Shirai, "*Effect of the tunnel oxide/*AlO_x

stacked hole-selective contacts on the junction properties at PEDOT: PSS/n-type Si interface", The 67th JSAP Spring Meeting, March 12-15, 2020, Tokyo, japan.

9) **A. Rajib**, E. Karim, K. Imai, S. Kurosu, T. Ukai, M. Tokuda, Y. Fujii, T. Hanajiri, R. Ishikawa, K. Ueno, and H. Shirai "*Role of water additive in the synthesis of AlO_x thin films by atmospheric-pressure mist chemical vapor deposition*" The 29th Materials Research Meeting, November 27-29, 2019, Yokohama, Japan.

10) **A. Rajib**, T. Kuroki1, K. Imai, S. Kurosu, T. Ukai, Y. Fujii, M. Tokuda, T. Hanajiri, R. Ishikawa, K. Ueno, H. Shirai, "*Role of water additive in the synthesis of AlO_x by mist-CVD*" The 80th JSAP Autumn Meeting, September 18-21, 2019, Hokkaido, Japan.

11) **A. Rajib**, T. Kuroki, S. Kurosu, T. Ukai, Y. Fujii, M. Tokuda, T. Hanajiri, R. Ishikawa, H. Shirai, "*PEDOT: PSS mist transport into Si nanopillar hole using Nafion as a mediator*." The 80th JSAP Autumn Meeting, September 18-21, 2019, Hokkaido, Japan.

12) Md. E. Karim, **A. Rajib**, M. Tokuda, S. Kurosu, T. Ukai, Y. Fujii, T. Hanajiri, R. Ishikawa, H. Shirai, "*PEDOT: PSS/n-Si heterojunction solar cells with ALD-AlO_x/n-Si field effective inversion layer*" The 80th JSAP Autumn Meeting, September 18-21, 2019, Hokkaido, Japan.

Table of Contents

Abstract I

Acknowledgments IV

List of Publications and Presentations VI

List of Tables XII

List of Figures XIII

List of Abbreviation XIX

Chapter 1: Introduction and Motivation 2

1.1 Thin film 2

1.2 Metal oxide and transition metal oxide thin films 5

1.3 Benefit of Al_2O_3 as insulating/dielectric layer 6

1.4 Thin-film fabrication method and benefits of mist-CVD 8

1.5 Motivation of this study 11

1.6 Structure of this dissertation 13

References: 14

Chapter 2: Experimental and Analytic methodologies 24

2.1 Mist-CVD system 24

2.1.1 Mist generation unit 25

2.1.2 Mist transport unit 27

2.1.3 Reaction unit 28

2.2 $MoSe_2$-based MIS-FET fabrication 29

2.2.1 Deposition of AlO_x thin films by mist-CVD 29

2.2.2 Preparation of $MoSe_2$ and As-doped WSe_2 flakes and transferred on to AlO_x/p+-Si by mechanically exfoliation technique *31*

2.2.3 Electrodes pattering and forming on $MoSe_2$-based MIS-FET *34*

2.3 Analytic methodology **35**

2.3.1 Chemical Structure by Fourier Transform Infrared (FT-IR) Spectroscopy *35*

2.3.2 Optical parameters by Spectroscopic Ellipsometry *37*

2.3.3 Morphological study by Atomic Force Microscope (AFM) *42*

2.3.4 Minority carrier lifetime utilize by Micro-photoconductive decay (μ-PCD) *44*

2.3.5 Surface observation by Optical microscope *46*

2.3.6 Elemental Composition and chemical bonding analysis by X-ray photoelectron spectroscopy (XPS) *47*

2.3.7 Crystallographic structure by X-ray diffraction *48*

2.3.8 Size distribution of mist precursors by the particle counter *49*

2.3.9 Van der Pauw method for Hall measurement *53*

2.3.10 Junction properties analysis by C-V measurement *55*

2.3.10 Carrier transport parameters of MIS-FET *62*

References **64**

Chapter 3: Results and Discussions **68**

3.1 Role of H_2O in the synthesis of amorphous AlO_x using mist-CVD from $Al(acac)_3$ and CH_3OH/H_2O system for surface passivation and electrical insulator layers **68**

3.1.1 Synthesis of AlO_x by mist-CVD with $Al(acac)_3$ and CH_3OH/ H_2O *69*

3.1.2 Post-fabrication exposure of Al(OH) and AlO_x network to H_2O and CH_3OH *73*

3.1.3 Role of H_2O as an additive during the growth of mist-CVD of AlO_x thin films *75*

3.1.4 Junction properties at the mist-CVD AlO_x/p-Si interface *77*

3.2 Synthesis of AlO_x thin films monitored by a fast-scanning mobility particle analyzer and applied as a gate insulating layer in the field-effect transistors **80**

3.2.1 Film properties of AlO_x thin films at different deposition parameters *80*

3.2.2 Effect of V_m on the film deposition of AlO_x thin films by mist-CVD *86*

3.2.3 Size distribution of mist particles monitored by scanning mobility particle analyzer *88*

3.2.4 Effect of V_m on the junction properties at the AlO_x/n+-Si interface and FET performance *94*

3.3 Synthesis of mist chemical vapor deposited $Al_{1-x}Ti_xO_y$ thin films and their application to a high dielectric material **100**

3.3.1 Synthesis of $Al_{1-x}Ti_xO_y$ thin films by mist-CVD *100*

3.3.2 Junction property at the $Al_{1-x}Ti_xO_y$/n-Si interface *105*

3.3.3 $Al_{1-x}Ti_xO_y$ as a gate insulator layer for MIS-FETs *112*

References **120**

Chapter 4: Conclusion and Future Work **126**

4.1 Summary of Results **126**

4.2 Future Work **128**

List of Tables

Table 1. 1. Various metal oxides and their applications. 6

Table 2. 1. AlO_x thin film deposition conditions. 30

Table 3.1. 1. Local vibration modes of AlO_x related FTIR peaks..............................70

Table 3.2. 1. Extracted parameters for Al/AlO_x (thickness = ~50 nm)/n^+-Si capacitor fabricated at different V_m values...98

Table 3.3. 1 Extracted parameters to utilize conduction band offset at the $Al_{1-x}Ti_xO_y$/n-Si interface as determined from C-V characteristics for different x values..............110

Table 3.3. 2 Electrical characteristics of $MoSe_2$-based n-channel MIS-FETs with $Al_{1-x}Ti_xO_y$ for different x values. 113

Table 3.3. 3 Covalent bond radius and atomic radius of W, Se, and As..................116

Table 3.3. 4 Electrical characteristics of As-doped WSe_2 based ambipolar MIS-FET where $Al_{0.74}Ti_{0.26}O_y$ used as dielectric layer. 118

List of Figures

Figure 1. 1. (a) CMOS for switching purposes. (b) CMOS as a memory device. 3
Figure 1. 2 Physical structure of an RGB OLED cell. 3
Figure 1. 3. Structure of solar cell. 4
Figure 1. 4. Thin-film is used for all daily necessities. 5
Figure 1. 5. Bandgap and dielectric constant trade-off of different metal oxides.........7
Figure 1. 6. Classification diagram of functional thin-film fabrication method. 9
Figure 1. 7. Chemical structure of aluminum and titanium acetylacetonate and its favorable solvents. 10

Figure 2. 1. Schematic image of mist deposition. 25
Figure 2. 2. Droplet generator using the ultrasonic vibrator. 26
Figure 2. 3. Disturbance of liquid cylinder which leads to break-up as predicted by Rayleigh. 27
Figure 2. 4. (a) Mist transport unit including carrier gas flow and mesh bias supply. **(b)** High-speed camera images at the inlet of the tubular furnace for different values of mesh bias V_m. 28
Figure 2. 5. Schematic diagram of reaction unit. 29
Figure 2. 6. Schematic diagram of the mist-CVD system. 30
Figure 2. 7. (a) Illustration of a typical CVT. (b) $MoSe_2$ quartz ampoule after crystal growth. (c) $Mose_2$ bulk crystal grown in the quartz ampoule. 32
Figure 2. 8. Microscopic image of mechanically exfoliated $MoSe_2$ flakes onto AlO_x/p^{++}-Si substrate. 33
Figure 2. 9. Microscopic image of $MoSe_2$ flake after patterning. 34
Figure 2. 10. 3D view and the microscopic image of $MoSe_2$ based MIS-FET where AlO_x is used as a dielectric layer. 35
Figure 2. 11. Schematic diagram of an FT-IR. 36
Figure 2. 12. Beam geometry for light with its electric field. 37
Figure 2. 13. (a) Basic procedure used in ellipsometry measurements to determine optical constant and layer thickness from experimental spectra. (b) Two-layer model used for the spectra analysis. 42
Figure 2. 14. Schematic diagram of AFM. 43

Figure 2. 15. Force curve of AFM. 44
Figure 2. 16. Principle of micro-photoconductive decay (μ-PCD) system.................45
Figure 2. 17. Schematic of a compound microscope. 46
Figure 2. 18. Schematic for the generation of energy difference by photoemission. .48
Figure 2. 19. Schematic of XRD...49
Figure 2. 20. The function of a particle counter. (b) Picture of Fast Scanning Mobility Particle Analyzer, Model-3091...50
Figure 2. 21. Schematic of a cascade impactor...51
Figure 2. 22. Schematic illustration of differential mobility analyzer. 52
Figure 2. 23. Schematics of continuous flow condensation particle counter (CPC). .53
Figure 2. 24. Experimental setup for Van-der-Pauw measurement...........................54
Figure 2. 25. Sample configuration for the Hall coefficient measurement using Van-der-Pauw method, with an applied magnetic field perpendicular to the sample surface. 55
Figure 2. 26. MOS capacitor structure with its equivalent circuit. 56
Figure 2. 27. Energy-band diagram of the three components of a MOS capacitor; (a) metal (aluminum), (b) Aluminum oxide, and (c) n-type silicon.................................57
Figure 2. 28. (a) AC and DC voltage of C-V sweep measurement. (b) Capacitance-voltage diagram of an Al/AlO_x/n-Si/Al MOS capacitor with the frequency of 1 MHz. 58
Figure 2. 29. Energy band diagram for flat band condition.......................................59
Figure 2. 30. Energy band diagram for accumulation condition with their schematic. 60
Figure 2. 31. Energy band diagram for depletion condition with their schematic......61
Figure 2. 32. Energy band diagram for inversion condition with their schematic......62
Figure 2. 33. Transfer characteristics of MIS-FET to evaluate the key parameters. ..63

Figure 3.1.1. Deposition rates for AlO_x films during mist-CVD as functions of the CH_3OH: H_2O ratio at a tabular furnace temperature of 350 and 400 ºC. (b) Deposition rates for AlO_x films at a CH_3OH: H_2O volume ratio of 9:1 as a function of the inverse of T_f. 69
Figure 3.1. 2. (a) FTIR spectra of AlO_x thin films fabricated by mist-CVD using various CH_3OH: H_2O ratios at 400 ºC, (b) FTIR spectra related to Al-O and O-Al-O between 500 and 1200 cm^{-1}, (c) AFM images of the corresponding AlO_x films. 72

Figure 3.1. 3. The n spectra of AlO_x thin films produced using mist-CVD with different CH_3OH: H_2O ratios at 400 ℃. 73
Figure 3.1. 4. (a) FTIR spectra of an Al(OH) thin-film fabricated at 400 ℃. (b) AFM images of the corresponding films. Variation in the (c) n spectra and (d) film thickness of Al(OH) films during exposure to a H_2O mist. 74
Figure 3.1. 5. (a) FTIR spectra of an AlO_x thin film fabricated at a T_f of 400 ℃ exposed to a CH_3OH mist. Changes in the (b) n spectra and (c) AFM images of the film before and after CH_3OH mist exposure. 75
Figure 3.1. 6. (a) High-speed camera images of CH_3OH/H_2O mist at the inlet and outlet positions of the tubular furnace at different CH_3OH to H_2O ratios. (b) Schematic of the fine structure of the CH_3OH/H_2O solution at lower and higher H_2O mixing conditions. 76
Figure 3.1. 7. Schematic diagram of the growth surface of AlO_x films for CH_3OH: H_2O ratios of (a) 10:0 and (b) 7:3. 77
Figure 3.1. 8. Effective minority carrier lifetime, τ_{eff}, and carrier recombination velocity, S, values for AlO_x films generated by mist-CVD with various CH_3OH: H_2O ratios. 78
Figure 3.1. 9. (a) J-E curves obtained from $Al/AlO_x/p^{++}$-Si/Al capacitors with films produced at various CH_3OH: H_2O ratios. (b) Q_f and D_{it} values for $Al/AlO_x/p^{++}$-Si/Al capacitors as functions of CH_3OH: H_2O ratio. 80

Figure 3.2. 1. (a) Deposition rate for AlO_x thin films through mist-CVD as a function of F_d, in an CH_3OH:H_2O ratio of 7:3 at a T_f of 400 ℃. (b) RMS roughness and (c) n spectra of the corresponding AlO_x thin films. 82
Figure 3.2. 2. (a) Deposition rate for AlO_x thin films by mist-CVD fabricated at different values of T_f, with a 0.025M $Al(acac)_3$, a CH_3OH:H_2O ratio of 7:3, and an F_d of 2400 sccm. (b) RMS roughness and (c) n spectra of the corresponding AlO_x thin films. 84
Figure 3.2. 3. (a) Deposition rate and (b) RMS value for AlO_x thin films by mist-CVD fabricated at different solution concentrations of $Al(acac)_3$ with a CH_3OH/H_2O ratio of 7:3 volume ratio, a T_f of 550 ℃, and an F_d of 2400 sccm. (c) n spectra of the corresponding AlO_x thin films. 85

Figure 3.2. 4. (a) Deposition rate for AlO_x thin films through mist-CVD fabricated at different values of V_m, using a 0.015M $Al(acac)_3$ solution and a $CH_3OH:H_2O$ mixture (7:3 volume ratio), at a T_f of 550 ℃, and an F_d of 2400 sccm. (b) AFM image and (c) n spectra of the corresponding ~50 -nm -thick AlO_x thin films....................................87

Figure 3.2. 5. Size distribution of CH_3OH and H_2O separately, and CH_3OH/H_2O solvent of (7:3 volume ratio) at an F_d of 2400 sccm at the inlet position **A** of the tubular furnace...89

Figure 3.2. 6. Size distribution of $Al(acac)_3/CH_3OH/H_2O$ mist particle at the (a) inlet and (b) outlet of the tubular furnace, **A** and **B**, for different F_d values using a 0.025 mol/L $Al(acac)_3$ solution and a CH_3OH/H_2O mixture (7:3 volume ratio) at a T_f of 400 ℃. The inset value is the integrated area of the total number density of mist for each deposition condition..90

Figure 3.2. 7. Size distribution of $Al(acac)_3/CH_3OH/H_2O$ mist particles (CH_3OH/H_2O= 7:3) measured with different (a) T_f for 0.025 mol/L $Al(acac)_3$ and (b) V_m for 0.015 mol/L $Al(acac)_3$ at the outlet **B** of the tubular furnace for an F_d of 2400 sccm. (c) High-speed camera images at the inlet of the tubular furnace for different values of mesh bias V_m...92

Figure 3.2. 8. (a) Deposition rate for AlO_x thin films by mist-CVD summarized as a function of the area ratio of $1-(A_{in}/A_{out})$ for varied F_d, T_f, and V_m conditions (**Figures. 3.2.1-3.2.4**) obtained from the size distributions of mist precursor at the inlet and outlet positions (**Figures 3.2.6 and 3.2.7**). **(b)** Refractive index (n) vs $(A_M/A_{out}) \times 100\%$ for varied F_d, T_f, and V_m. The average particle size of the mist precursor at its highest number density corresponding A_M is given on the horizontal axis. (c) $S_{q/rms}$ vs average size of mist precursor for varied F_d, T_f, and V_m...93

Figure 3.2. 9. (a) J-E curves in the $Al/AlO_x/n^+$-Si MOS capacitor with AlO_x grown by mist-CVD at different V_m values. (b) Recombination velocity S_{eff}, (c) Minority carrier lifetime τ_{eff} of AlO_x thin films fabricated using mist-CVD with different values of V_m. 95

Figure 3.2.10. (a) Capacitance-voltage (C-V) hysteresis behavior of the AlO_x thin films fabricated through mist-CVD at different V_m for a measurement frequency of 1 MHz. 96

Figure 3.2. 11. Relative dielectric constant κ for AlO_x thin films with a thickness of 50 nm deposited under different values of V_m using mist-CVD on n-Si.........................97

Figure 3.2. 12. (a) Optical image and schematic of the device structure of corresponding FETs. The channel length and width are 8.39 μm and 4.87 μm, respectively. (b) Transfer characteristics of the $MoSe_2$ based FET, (c) √ I_SD- Vg plots where AlO_x is used as a gate insulator fabricated at different Vm values. (d) Transfer charateristics of the $MoSe_2$ based FET hysteresis behavior; AlO_x thin films were fabricated by mist-CVD at different V_m. 99

Figure 3.3. 1. Ti composition ratio x in the $Al_{1-x}Ti_xO_y$ films plotted as a function of ratio γ for different CH_3OH/H_2O solvent mixing ratios. 101

Figure 3.3. 2. (a) Deposition rate for $Al_{1-x}Ti_xO_y$ thin films fabricated by mist-CVD plotted against different CH_3OH/H_2O solvent ratios for a γ of 70/30, an F_d of 2400 sccm, and a T_f of 550 ℃. (b) High-speed camera image of $Al(acac)_3/Ti(acac)_4$ mist precursors with different CH_3OH/H_2O ratios monitored at the outlet position of the tabular furnace. 102

Figure 3.3. 3. (a) Size distribution of $Al(acac)_3/Ti(acac)_4$ composite mist particle for an γ ratio of 70/30 mist particles for different CH_3OH/H_2O solvent ratios monitored at the outlet position of the tabular furnace., (b) Arrangement of mist-CVD system for the monitoring of mist droplets size by particle counter at the outlet position B at the tabular furnace. *(c)* Size distribution of solely $Al(acac)_3/Ti(acac)_4$ mist particles monitored at the outlet position of the tabular furnace for CH_3OH/H_2O of 70/30, an F_d of 2400 sccm, and a T_f of 550 ℃. 104

Figure 3.3. 4. AFM image of the corresponding ~40-nm- thick $Al_{1-x}Ti_xO_y$ thin films synthesized for different γ values at a CH_3OH/H_2O ratio of 90/10 where a linear relation between γ and *x* was observed. 105

Figure 3.3. 5. (a) Capacitance-voltage curve with a schematic representation in the inset of the $Al/Al_{1-x}Ti_xO_y/n^+$-Si MIS capacitors fabricated at different x values for a measurement frequency of 1 MHz. (b) $(C_{ox}/C_{MOS})^2$-1 vs gate voltage curve to determine flat band voltage V_{FB} for $Al_{1-x}Ti_xO_y$ thin films with a thickness of 40 nm deposited under different values of x. 107

Figure 3.3. 6. Interface state density D_{it} as a function of x in the $Al_{1-x}Ti_xO_y$ thin films. 107

Figure 3.3. 7. (a) XPS spectra of O(1s) core energy level region for $Al_{1-x}Ti_xO_y$ thin films for different x values. Schematic showing the conceptual structural features of (b) AlO_x and (c) $Al_{1-x}Ti_xO_y$. 109
Figure 3.3. 8. C^{-2}-V plot for different x values in $Al_{1-x}Ti_xO_y$ thin films to determine built-in potential. 109
Figure 3.3. 9. (a) Dielectric constant, κ, and electronic bandgap E_g plotted as a function of x. (b) Energy band diagram of $Al_{1-x}Ti_xO_y$ thin films as a function of Ti compositions ratio x. 111
Figure 3.3. 10. (a) Transfer characteristics of the $MoSe_2$-based FETs where $Al_{1-x}Ti_xO_y$ is used as a gate dielectric layer for different x values at a V_{DS} of 0.2 V. (b) Optical image and schematic of the device structure of corresponding FETs. The channel length and width are 10.4 and 6.8 μm, respectively. 113
Figure 3.3. 11. (a) Crystal structure of the hexagonal shaped As-doped WSe_2 layer, (b) Wide scan XPS spectrum for as-synthesized bulk As-doped WSe_2 crystals, (c) AFM image of an As-doped WSe_2 flake transferred onto a $Al_{0.74}Ti_{0.26}O_y$/Si substrate, which thickness was estimated to be about 25 nm corresponding to the number of ~20 layers stacked. 116
Figure 3.3. 12. (a) Transfer characteristics of a 25-nm-thick As-doped WSe_2 transistor under different V_{DS} values on a linear and a logarithmic scale, Output characteristics of the As-doped WSe_2 transistors under different V_{DS} values in the positive V_{DS} regime (b) and in the negative V_{DS} regime (c). 118
Figure 3.3. 13. (a) Schematic of a complementary inverter circuit comprising two ambipolar transistors, one which operated as an n-type channel transistor whereas the other was conducted as a p-channel transistor. (b) Inverter characteristics where V_{IN} and V_{DD} were both positively biased (1st quadrat), (c) Inverter characteristics where V_{IN} and V_{DD} were both negatively biased (3rd quadrat). (d) The corresponding voltage gain of the complementary inverter ($\Delta V_{OUT}/\Delta V_{IN}$). 119

List of Abbreviation

AlO_x or Al_2O_3	Aluminum oxide
Mist-CVD	Mist Chemical Vapor Deposition
CH_3OH	Methanol
H_2O	Water
$Al(acac)_3$	Aluminum Acetylacetonate
$Ti(acac)_4$	Titanium Acetylacetonate
c-Si	Crystalline Silicon
MOS	Metal Oxide Semiconductor
FET	Fieled Effect Transistor
MIS-FET	Metal Insulator Semiconductor FET
CMOS	Complementary MOS
OLED	Organic Light Emitting Diode
FeRAM	Ferroelectric Random-Access Memory
RGB OLED	Red Green Blue OLED
PET	Polyethylene Terephthalate
In_2O_3	Indium Oxide
SnO2	Tin Oxide
ZnO	Zinc Oxide
$SrTiO_3$	Strontium Titanate
HfO_2	Hafnium Oxide
$ZrHfO_2$	Zirconium Hafnium Oxide
$Al:HfZrO_2$	Aluminum doped Zirconium Hafnium Oxide
Fe_3O_4	Iron oxide
Cr_2O_3	Chromium Oxide
GaN	Gallium Nitride
TiO_2	Titanium Oxide
GaO	Gallium Oxide
Y_2O_3	Yttrium Oxide
κ	Dielectric Constant
ITO	Indium Tin Oxide
Cu_2O	Cupric Oxide

CuO	Copper Oxide
$CuAlO_2$	Copper doped Aluminum Oxide
NiO	Nickel Oxide
MgO	Magnesium Oxide
CPU	Central Processing Unit
DRAM	Dynamic Random-access Memory
SiO_2	Silicon Oxide
E_g	Bandgap
PVD	Physical Vapor Deposition
MBE	Molecular Beam Epitaxy
PLD	Pulsed Laser Deposition
CVD	Chemical Vapor Deposition
PECVD	Plasma Enhanced CVD
MOCVD	Metal-Organic CVD
ALD	Atomic Layer Deposition
N_2	Nitrogen
T_f	Tabular Furnace Temperature
F_d	Dilution Gas Flow Rate of N_2
FMPS	Fast Mobility Particle Sizer
n-Si	n-type Silicon
p-Si	P-type Silicon
$MoSe_2$	Molybdenum di-selenide
WSe_2	Tungsten di-selenide
As-doped WSe_2	Arsenic doped WSe_2
Ta_2O_5	Tantalum Oxide
$Al_{1-x}Ti_xO_y$	Aluminum Titanium Oxide
γ	$Ti(acac)_4/Al(acac)_3$
C-V measurement	Capacitance vs Voltage Measurement
d_p	Droplet Size
nm	Nanometer
µm	Micrometer
cm	Centimeter
V_m	Mesh Bias Voltage

kV	Kilo-volt
Mol/L	Mole/Littre
sccm	Standard cubic centimeter per minute
MHz	Mega Hertz
FT-IR Spectroscopy	Fourier Transform Infrared Spectroscopy
SE	Spectroscopic Ellipsometry
AFM	Atomic Force Microscope
M-PCD	Micro-photoconductive Decay
τ_{eff}	Minority Carrier Lifetime
S_{eff}	Recombination Velocity
XPS	X-ray Photoelectron Spectroscopy
XRD	X-ray Diffraction
DMA	Differential Mobility Analyzer
CPC	Condensation Particle Counter
MOSCAP	Metal Oxide Semiconductor Capacitor
E_f	Fermi Level
E_i	Intrinsic Level
μ_{lin}	Linear Mobility
μ_{sat}	Saturation Mobility
C_{ox}	Oxide capacitance
I_{DS}	Drain to Source Current
V_g	Gate Voltage
V_{DS}	Drain to Source Voltage
L	Length of Channel
W	Width of the Channel
V_{th}	Threshold Voltage
$N_{trap.charge}$	The Trapped Charge Density
C_i	Insulator Capacitance
SS	Subthreshold Voltage
ΔE_a	Thermal Activation Energy
RMS	Root Means Square
n	Refractive Index
J-E	Current Density vs. Electric Field

Q_f	Negative Fixed Charge density
D_{it}	Interface Trap Density
φ_{MS}	Al-Si Work Function Difference
DI	De-ionized
Ψ_s	Surface Potential
K	Boltzmann Constant
Na	Carrier density of Si substrate
CVT	Chemical Vapor Transport
TMDCs	Transition Metal Dichalcogenides
QSSPC	Quasi-Steady-State Photoconductance
C-MOS	Complementary Metal Oxide Semiconductor

Chapter 1
Introduction and Motivation

Chapter 1: Introduction and Motivation

1.1 Thin film

Though the definition of thin-film is not absolutely correct. But someone described the thin film as a thin layer of material ranging from fractions of a nanometer to several micrometers is deposited onto a metal, ceramic, or semiconductor.[1.1] The thin films for optical purposes which was the first application of thin films can be dated to exactly 1912. Pohl and Pringsheim fabricated the mirrors using an evaporation process of metals like Ag and Al out of a MgO crucible in high vacuum. Nowadays, thin films have become an integral part of the micro-and nano electronics and photonics industry with applications ranging from gate dielectrics for high-performance integrated circuits, Superconductor, Complementary Metal Oxide Semiconductor (CMOS), Metal Insulator Semiconductor Field Effect Transistor (MIS-FET), Ferroelectric Random-access Memory (FeRAMs), solar cell, OLED displays to smart sensors. Applications of thin films may be grouped under the following generic areas:

- **Electronic components and display.** The product of electronic components such as semiconductors, single and multilayer metal conductor film, and microelectronic integrated circuits have obtained enormous and vast applications for thin film deposition. Superconducting technology has also taken more consideration for high-film magnets, power cables, rotating machines, and water purification. The fabrication of CMOS for logic and integrated circuit or memory application requires dielectric material and semiconductors (shown in **Figure 1.1**).[1.2] The fabrication of electronic displays requires conductive and transparent films, luminescent or fluorescent film as well as dielectric and insulating layers.[1.3] A schematic of RGB organic light-emitting diode illustrated in **Figure 1.2**.

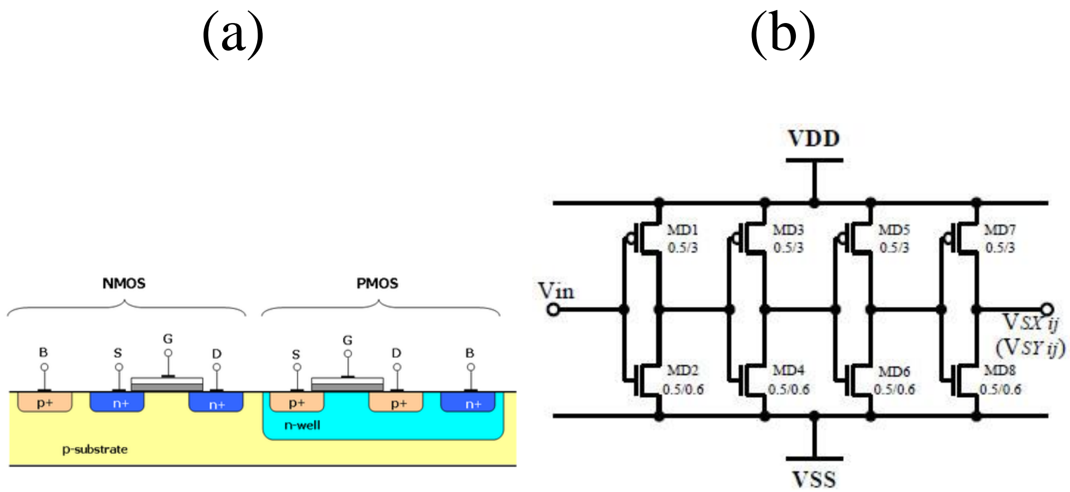

Figure 1. 1. (a) CMOS for switching purposes. (b) CMOS as a memory device.

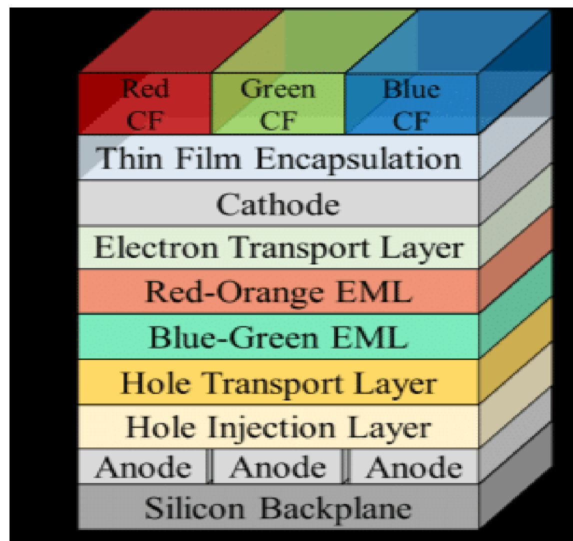

Figure 1. 2 Physical structure of an RGB OLED cell.

❖ **Solid surface coating and biomedical.** The tribology resistance and corrosion performance of components can be improved by coating the surface of the component with thin-film coatings of carbides, silicide, nitrides, and borides respectively. These coatings are being used in tools production, an area with sliding friction like bearing and machine parts. In recent times, more attention and interest has been given to films of diamond-like carbon because of this capability to dissipate heat, hardness, electrical insulation, and respectable resistance to high-temperature and high-energy radiation.1.3 It is also used for biomedical application to enhance proper osteointegration and adhesion properties.

- **Energy and optoelectronic applications.** Thin film coating is essential for optical coating. It is used to filter interference on solar panels and acts as antireflection purpose (shown in **Figure 1.3**). Thin films with appropriate refractive index gradients are being used on optical fibers to improve refraction and absorption coefficient performance. High reflective coatings that can withstand the extremely high radiation intensities without being degraded and failed when in use are needed for laser optics and are being achieved by deposition of thin films metal reflective coating with excellent properties. Infrared reflecting coatings are applied to filament lamps to increase the luminous flux intensity. Commercial demand for thin film coating is also on the rise in the optical data storage devices like computer memory and storage disk. They serve as a protective coating on the surface to and act as a shield against temperature rise. Thin film has also been used extensively in coating window glass and mirror to prevent heat from passing through.[1.4]

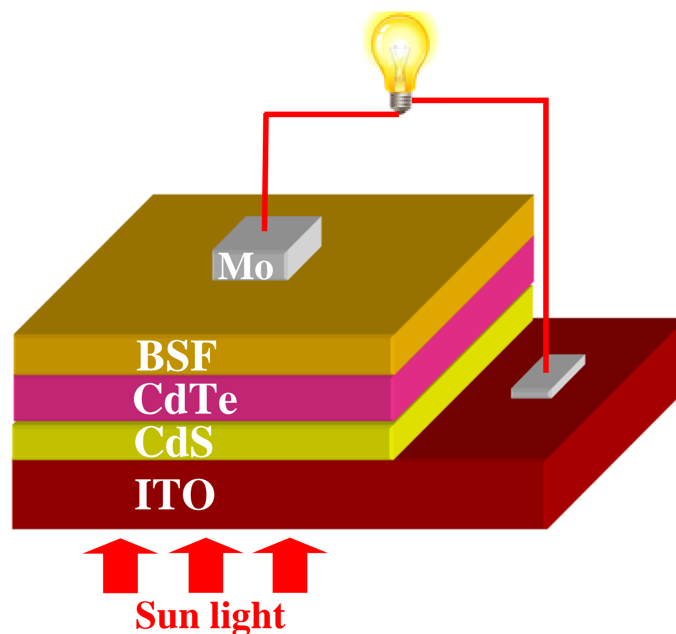

Figure 1. 3. Structure of solar cell.

Besides these, thin film has a lot of applications around us in modern society. For example, the anti-reflective coating is used in eyeglasses and camera lenses. Protective films are used for bags and PET bottles. Reflective film is utilized for displays and touch panels, which protect from dirt. Heat resistant membranes are usually applied in the space industry, on the other side, thermal control membranes and photocatalytic

membranes are useful for environmental protection. **Figure 1.4** represents some of the applications of the thin film that are useful in daily necessities.

Figure 1. 4. Thin-film is used for all daily necessities.

1.2 Metal oxide and transition metal oxide thin films

Since more than 20% of oxygen in the atmosphere on the earth, all substances are finally oxidized. As a consequence of oxidization, different types of metal oxide and transition metal oxide are formed, some of them are stable those are ideal for the grown thin film. These metal oxides and transition metal oxides have been studied in various fields as shown in **Table 1.1**. Transparent conducting film (In_2O_3, SnO_2, ZnO, etc.), ferroelectric film (HfO_2, $ZrHfO_2$, Al:$HfZrO_2$), ferromagnetic film (Fe_3O_4, Cr_2O_3, etc.) have been also extensively studied. On the other side, some of the metal oxides and transition metal oxides such as ZnO, GaN, SnO_2, TiO_2, GaO, Al_2O_3, HfO_2, ZrO_2, and Y_2O_3 have received considerable attention as dielectric materials (having high dielectric constant (k)) and wide-bandgap semiconductors. They have been studied toward reducing the driving voltage and high transconductance in metal-oxide-semiconductor field-effect transistor (MIS-FET) devices and for their relevance in power electronics, solar cells, and photodetectors.

Table 1. 1. Various metal oxides and their applications.

Properties	Materials	Application (example)	Ref
Transparent conductive film	ZnO, ITO, SnO_2	Touch panel, Display, Solar cells, TFT	1.5- 7
Semiconductor film	Cu_2O, CuO, $CuAlO_2$	Thin film transistor, Sensor, Varistor	1.8- 10
Insulating film	ZnO, GaN, SnO_2, TiO_2, GaO, Al_2O_3, HfO_2, ZrO_2, and Y_2O_3	The electronic device, MIS-FET, Solar cell, Capacitor, Protector.	1.11-19
Ferroelectric film	HfO_2, $AlHfO_2$, ZrO_2, $ZrHfO_2$	Memory device	1.20-23
Magnetic material	Fe_2O_4,	Recording device, Spin control device	1.24
Photocatalyst	TiO_2	Energy source, air purification, surface protection	1.25
Anti-reflective coating	MgO, ZrO_2, Al_2O_3	Optical parts, glasses, UV protection glass	1.26-28
Surface treatment film	Cr_2O_3, Y_2O_3, TiO_2	Surface protection	1.29-31

1.3 Benefit of Al_2O_3 as insulating/dielectric layer

The dielectric insulator is a key component in microelectronic devices such as the central processing unit (CPU), dynamic random-access memory (DRAM), and flash memory. The enhancement of the capacitive coupling between adjacent metals and semiconductors is the basic function of the dielectric material, although suppression of leakage current between electrodes has also been considered, which undermines the energy consumption (in CPU and DRAM) or long-term reliability (in flash memory). In past decades, silicon dioxide (SiO_2) has been considered a dielectric material because it shows defect-free, high-quality thin-film growth. As the integration level of microelectronic devices is currently exponentially increasing, scaling down of device

geometry has become inevitable. Any scaling can't be possible without the thinning of the gate dielectric. However, if the thickness of the SiO_2 layer becomes lower than ~ 1 nm, the leakage current due to the quantum tunneling effect starts to dominate,[1.32] which causes serious problems in power consumption and device performance. To overcome this physical obstacle new insulators that possess high dielectric constant have been investigated.[1.32-33] Currently, HfO_2/Al_2O_3 (as the dielectric in CPU),[1.33] ZrO_2 (as the capacitor dielectric in DRAM),[1.34] and Al_2O_3/TiO_2 (as the blocking oxide in charge trap flash memory)[1.35] have been extensively studied.

In addition to a large dielectric constant, the insulator material with a large bandgap is also required to suppress the charge injection from electrodes into dielectrics that cause the leakage current. Therefore, the ideal high-κ dielectrics should possess both large Eg and κ. The bandgap and dielectric constant of well-known oxides are plotted in **Figure 1.5**, the trade-off is clearly noticeable. Among the dielectric or insulating metal oxides, AlO_x is a promising candidate for such applications because of its wide bandgap, high breakdown field, high passivation ability of c-Si, and good thermal stability. The bandgap and the dielectric constant of AlO_x can be controlled by introducing guest metal oxide. TiO_2 is one of the possible guest metal oxides as its dielectric constant is high enough over 60 (**Figure 1.5**).

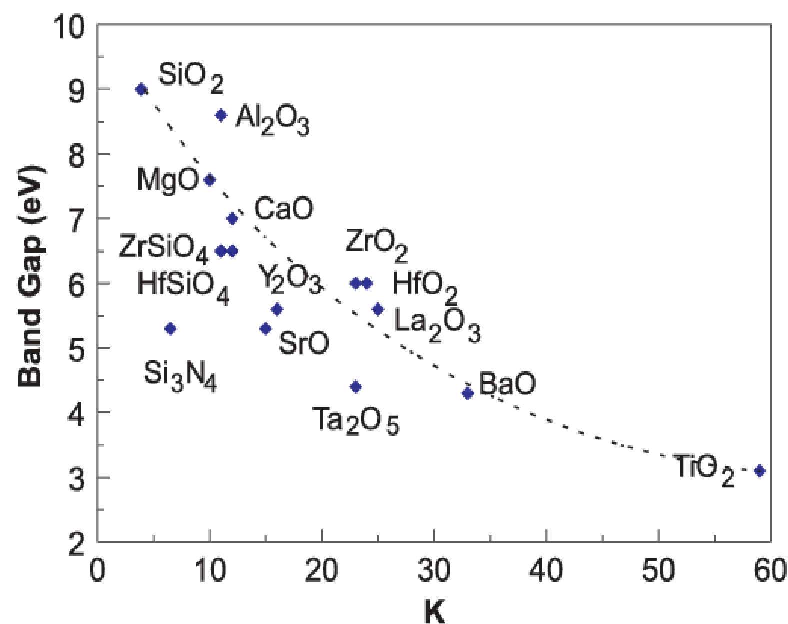

Figure 1. 5. Bandgap and dielectric constant trade-off of different metal oxides.[1.36]

1.4 Thin-film fabrication method and benefits of mist-CVD

These metal oxides and transition metal oxides thin films, especially AlO_x and TiO_x and their alloy, discussed in the previous section have been extensively studied using various film deposition methods shown in **Figure 1.6**. It can be classified into gas phase deposition and solution process. The former process is a mainly non-equilibrium process such as all physical vapor deposition (PVD), i.e, vacuum evaporation,[1.37-38] Molecular Beam Epitaxy (MBE),[1.39-40] Pulsed Laser Deposition (PLD),[1.41-43] Sputtering,[1.44-46] Plasma Enhanced Chemical Vapor Deposition (PECVD),[1.47] at low-pressure condition. On the other side, all solution-based processes such as sol-gel,[1.48] spray coating,[1.49], etc., and most of the CVD methods such as Metal-Organic CVD (MOCVD),[1.50] Atomic Layer Deposition (ALD),[1.51-54] mist-CVD,[1.55-58,] etc. are classified as equilibrium reaction systems. In the non-equilibrium systems, uniform and high-quality thin-films are grown by controlling the growth conditions of precursor composition, gas species, pressure, temperature, and incident power; but no need to control the chemical reaction. However, stress-free and damage-less thin films can be easily obtained using the equilibrium reaction systems.

CVD such as thermal CVD and MOCVD belong to the equilibrium process. In this method, highly active and high vapor pressure material is kept under a vacuum or in an inactive gas environment, resulting in chemical reactions to form thin films at the substrate surface in the vapor phase. On the other side, the solution process of the sol-gel, spray method, spin coat, etc. belongs to the latter category. In this method, stable materials under the standard condition are coated or injected on the substrate surface and thin films are fabricated with arbitrarily assisting energy such as heat and electric field. Therefore, in the CVD system, high-quality thin films with few impurities can be obtained, although the apparatus configuration and their system design are complicated and need to focus on the safety of the hazardous materials. On the other side, solution process using standard environment at atmospheric pressure, although the possibility of remaining of inert ingredients in the solution to thin films, the possibility of contains cracks during the formation of solid from the liquid during annealing, and the controlling of thickness is another issue.

Among them, mist-CVD is classified as the equilibrium process from solution as a starting material at atmospheric pressure. It takes the benefits of CVD and the solution

processes, facilitating the production of a well-controlled thin film using a simple method. Though mist-CVD is a solution-based method, it can be capable to deposit from the liquid source without the inherent limitations of spin coating or other solution-based techniques. As the mist droplet of the mist deposition system has no initial force, the force due to the N_2 supply carries the mist into the chamber, which facilitates uniformly coalesces on the substrate surface. As a result, mist-CVD is independent of the shape of the substrate and allows controlled deposition of thin films as thin as ~ 2 nm. In the mist-CVD system, the film deposition rates and film properties are determined by the deposition parameters of the mist-CVD system, including atomization frequency and power, the N_2 flow rate for mist generation and carrier, solution concentration, tabular furnace temperature, mesh bias supply during film deposition, etc. To obtain a smooth surface, fine mist droplets are one of the challenges. It is very possible to obtain fine mist particles by optimizing the above deposition parameters of the mist-CVD system.

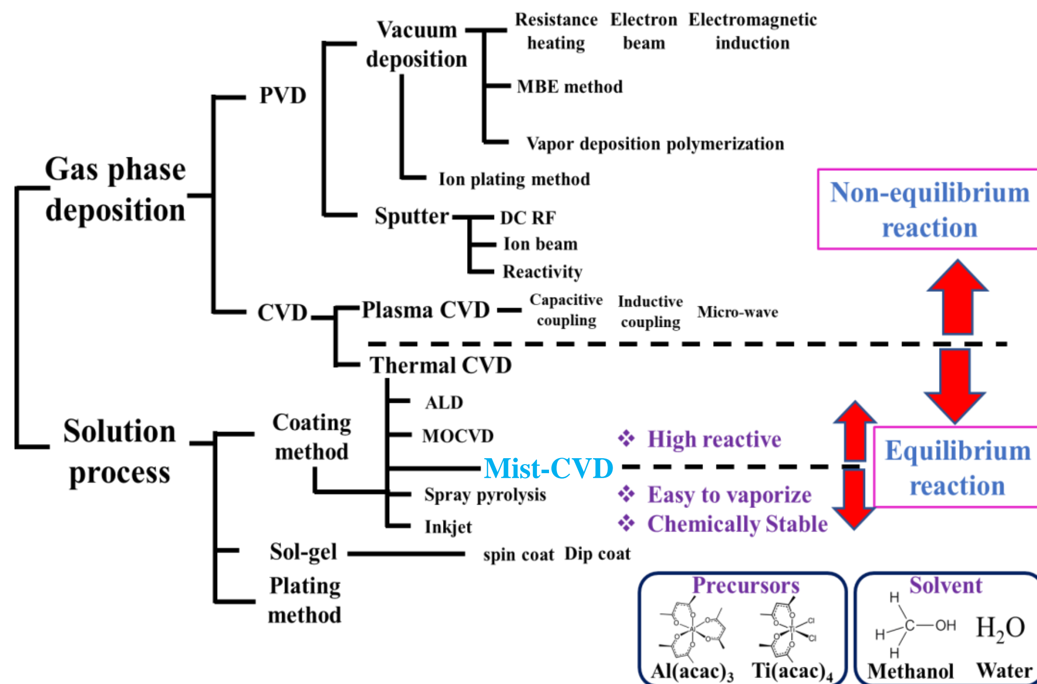

Figure 1. 6. Classification diagram of functional thin-film fabrication method.[1,60]

Additionally, mist-CVD can be employed to prepare metal-oxide-alloy thin films using metal acetylacetonates such as aluminum acetylacetonate ($Al(acac)_3$) or titanium

acetylacetonate (Ti(acac)$_4$, which are cost-effective, chemically stable, and low-vapor-pressure materials. The chemical structure of Al(acac)$_3$ and Ti(acac)4 are shown in **Figure 1.7**. The crucial point in Al(acac)$_3$ is the initiation of hydrolysis and control of condensation. During chelation either one of the alkoxy bonds of [Al(OR)$_3$] is replaced by acac, or there can be a polymeric form such as [Al(OR)$_2$(acac)$_n$]. The metal oxide-like aluminum oxide formation reaction proceeds via a novel pathway involving a cascade of reaction steps. Solvolysis of acetylacetonate involving a C-C bond cleavage results in the formation of N-benzyl acetamide and enolate ligands. The enolate ligands mainly undergo a ketimine condensation reaction, which finally induces the formation of metal oxide such as AlO_x, GaO_x, SnO_2, ZnO, MgO, NiO, TiO_2, and so on.[1.60] In mist-CVD, the film is grown via thermal decomposition of the source material, which is dissolved in a solvent such as Toluene, acetone, ethyl acetate, low molecular weight alcohol (shown in **Figure 1.7**).[1.61]

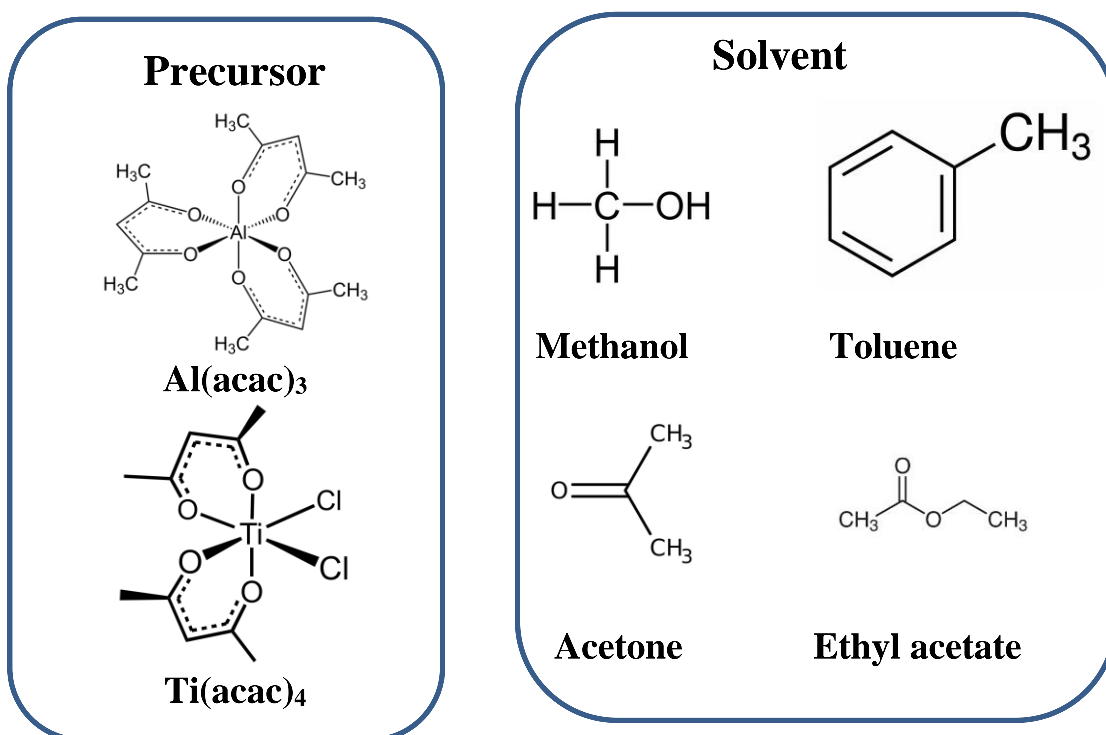

Figure 1. 7. Chemical structure of aluminum and titanium acetylacetonate and its favorable solvents.

1.5 Motivation of this study

More recently, the epitaxial growth of many types of metal oxides such as GaO_x, SnO_2, ZnO, MgO, NiO, TiO_2, etc. has been extensively studied.[1.62-65] To improve the crystallinity, some guest materials are also injected into the subjected metal oxide thin film have been studied.[1.66-68] Among them, the high-quality epitaxial growth of GaO_x and some metal oxide like Al, Mg, etc. doped GaO_x on the sapphire substrate has been extensively studied by mist CVD, which is expected for the power device in the next generation.[1.65, 1.69-70] Most studies of thin films using the mist-CVD focus on the synthesis of crystalline thin films on sapphire by adjusting the deposition condition and device performance. On the other side, the amorphous metal oxide thin film as an insulating layer is more preferable to fabricate MIS based device, which is much uniform, crack-free, fewer interface defects, and able to suppress leakage current. However, few studies on the growth mechanism and role of solvent in the synthesis of metal oxide films using mist CVD have been performed. Recently, Zhang, Q.; et. al. fabricated pure anatase phase TiO_2 thin films by mist-CVD by adjusting the CH_3OH to H_2O mixing ratio as the solvent and obtained the intensity of anatase phase TiO_2 peaks increased with the increase of H_2O mixing ratio.[1.62] Kim, D.-H.; et al. studied the effect of solvent H_2O content on the dielectric properties of Al_2O_3 films grown by mist-CVD and attained improved dielectric properties by adjusting the CH_3OH to the H_2O mixing ratio.[1.55, 1.71] However, the role of H_2O in the synthesis of Al_2O_3 thin films by mist-CVD is still not clear. To this aim, we have studied the role of H_2O added as a solvent during the synthesis of AlO_x thin films from $Al(acac)_3$ and CH_3OH by using atmospheric pressure mist-CVD. The effect of exposing these films to H_2O or CH_3OH mists after synthesis was also assessed to understand the surface chemistry the growth surface.

Recently, several groups have been concentrated on the synthesis of smooth, conformal, amorphous AlO_x thin films by mist-CVD as a dielectric layer.[1.54, 1.56, 1.72] However, the correlation among the size distribution of the negatively charged $Al(acac)_3$ mist precursor, film property, and junction property at the AlO_x/n-Si interface are still unclear. To this aim, we have also studied the synthesis of AlO_x thin films from $Al(acac)_3$ and CH_3OH/H_2O ratio with a ratio of 7:3, was investigated using mist-CVD for different deposition parameters, i.e., dilution gas flow rate of N_2 F_d, tabular furnace

temperature T_f, solution concentration, and mesh bias V_m via the analysis of the size distribution of mist particles by using a scanning mobility particle analyzer.

On the other side, Two-dimensional transition metal dichalcogenides (TMDCS) have received considerable attention as an active layer of MIS-FET due to their layered structure and direct and indirect bandgap transition. $MoSe_2$ has a wide band-gap that ranges from 1.55 eV to 1.1 eV according to the number of layers; in detail, bulk $MoSe_2$ shows an indirect band-gap of 1.1 eV, while the monolayer $MoSe_2$ has a direct band-gap of 1.55 eV. On the other sense, $MoSe_2$ is layered materials with strong in-plane interactions enabling mechanical exfoliation into two-dimensional layers of single unit cell thickness. Therefore, mechanically exfoliated molybdenum di-selenide ($MoSe_2$) flakes as a channel were used to investigate the potentiality of fabricated AlO_x films to act as a gate insulator layer in MIS-FETs.

A gate dielectric material with a high dielectric constant (high-k) and a wide bandgap has been received considerable attention for high-performance metal-oxide-semiconductor field-effect transistor (MIS-FET).[1.73-77] Here, high-k insulators are desirable for high transconductance corresponding to high mobility and also to scall down the device size, on the other hand, a wide bandgap and large conduction band offset are necessary for sufficient suppression of the charge injection from electrodes into dielectrics that cause gate leakage current even at the forward bias of MIS-FET.[1.78-81] However, there is a trade-off between these two properties.[1.82,1.83] One effective proposal for balancing between dielectric constant, κ and bandgap energy, E_g is employing aluminum titanium oxide $[(Al_2O_3)_{1-x}TiO_2)_x]$ ($Al_{1-x}Ti_xO_y$) with intermediate properties of Al_2O_3 (κ ~9, E_g~ 7 eV) and TiO_2 (κ ~50, E_g ~3 eV).[1.84-86] To this objective, we have studied the effect of the $Ti(acac)_4$ addition as a guest element on the synthesis of $Al_{1-x}Ti_xO_y$ thin films by mist-CVD from $Al(acac)_3$ using various CH_3OH/H_2O solvent ratio for different precursor mixing ratios γ [=$Ti(acac)_4/Al(acac)_3$] under the optimized deposition condition of AlO_x thin films provided in the previous study. The junction properties at the corresponding $Al_{1-x}Ti_xO_y$/n-Si interface and examining the potential of $Al_{1-x}Ti_xO_y$ obtained through mist-CVD to act as a high dielectric gate material for metal-insulator-semiconductor field-effect transistors (MISFETs) are also investigated by using mechanically exfoliated molybdenum di-selenide ($MoSe_2$) and Arsenic (As)-doped tungsten di-selenide (WSe_2) flakes as an active layer including the assembly of the complementary metal-oxide-semiconductor (C-MOS) inverter.

1.6 Structure of this dissertation

In this work, mist-CVD deposited AlO_x thin films were synthesized and applied as a gate dielectric layer for MIS-FET. Further, to improve the dielectric properties, guest metal oxide such as TiO_2 was carried out to form $Al_{1-x}Ti_xO_y$ thin films as its dielectric constant is over 50.

In **chapter 2**, a brief discussion of the mist-CVD system has been conducted, including every part of the system. The effect of each parameter has also been discussed. The device such as Al/AlO_x or $Al_{1-x}Ti_xO_y$/n-Si/Al MOS capacitor and exfoliated $MoSe_2$ based MIS-FET, fabrication steps were described in this chapter. The instruments used throughout this study have been discussed at the end of this chapter.

Chapter 3 describes the results obtained in this work. In particular, the first part of this chapter focuses on the effect of H_2O in the synthesis of amorphous AlO_x thin film using mist-CVD from Al(acac)$_3$ and the CH_3OH/H_2O system. The effects of exposing these films to H_2O or CH_3OH mists after synthesis to understand the surface chemistry of the growth surface is also carefully discussed in this part. As a second topic, the effect of deposition parameters, including carrier gas flow, furnace temperature, precursor concentration, and mesh bias supply, on the film properties of AlO_x thin film is discussed. The size distribution of mist particles monitored by particle counter at both inlet and outlet positions A and B for each deposition condition are also discussed in this section. The latter of this chapter focus on the effect of the addition of Ti(acac)$_4$ during the synthesis of $Al_{1-x}Ti_xO_y$ thin films by mist-CVD from Al(acac)$_3$, using various CH_3OH/H_2O solvent mixing ratio for different precursor mixing ratios γ [=Ti(acac)$_4$/Al(acac)$_3$] is examined under the optimized deposition condition of AlO_x thin films provided in the first part of this chapter.

In **chapter 4**, the study on the synthesis of AlO_x based thin films by using the mist-CVD system by optimizing the deposition parameters monitored by the particle counter, aim to use as a dielectric layer for MIS-FET are summarized including some remaining issues to further improve and understand the dielectric properties of MIS-FET.

References:

1.1 Abegunde, O. o.; Akinlabi, E. T.; Oladijo, O. P.; Akinlabi, S.; and Ude, A. U. "Overview of thin film deposition techniques" *AIMS Mater. Science* **6(2)**, 174-199, (2019).

1.2 Shanmugasundaram, K. "*A study of the mist deposition and patterning of liquid precursors thin films*", The Pennsylvania State University (2008).

1.3 Seshan, K. "*Handbook of thin film deposition*", William Andrew, (2012).

1.4 Martin, P. M. "*Handbook of deposition technologies for films and coatings: science, applications and technology*", William Andrew (2009).

1.5 Sahu, D.R.; and Huang, J.L. "Development of ZnO-based transparent conductive coatings", *Solar Energy Materials and Solar Cells* **93**, 1923-1927 (2009).

1.6 Gao, J.; Chen, R.; Li, D. H.; Jiang, L.; Ye, J. C.; Ma, X. C.; Chen, X. D.; Xiong, Q. H.; Sun H. D.; and Wu, T. "UV light-emitting transparent conducting tin-doped indium oxide (ITO) nanowires" *Nanotechnology* **22**, 195706, (2011).

1.7 Hoel, C. A.; Mason, T. O.; Gaillard, J. F.; and Poeppelmeier, K. R. "Transparent Conducting Oxides in the ZnO-In_2O_3-SnO_2 System" *Chem. Mater.* 22, 3569-3579 (2010).

1.8 Yao, Z. Q.; Liu, S. L.; Zhang, L.; He, B.; Kumar, A.; Jiang, X.; Zhang, W.J.; and Shao, G. "Room temperature fabrication of p-channel Cu_2O thin-film transistors on flexible polyethylene terephthalate substrates" *Appl. Phys. Lett.* **101**, 042114, (2012).

1.9 Sung, S. Y.; Kim, S. Y.; Jo, K. M.; Lee, J. H.; Kim, J. J.; Kim, S. G.; Pearton, S. J.; Norton, D. P.; and Heo, Y. W. "Fabrication of p-channel thin-film transistors using CuO active layers deposited at low temperature" *Appl. Phys. Lett.* **97**, 222109, (2010).

1.10 Yao, Z. Q.; He, B.; Zhang, L.; Zhuang, C. Q.; Ng, T. W.; Liu, S. L.; Vogel, M.; Kumar, A.; Zhang, W. J.; Lee, C. S.; Lee, S. T.; and Jiang, X. "Energy band engineering and controlled p-type conductivity of $CuAlO_2$ thin films by nonisovalent Cu-O alloying" *Appl. Phys. Lett.* **100**, 062102, (2012).

1.11 Kälblein, D.; Weitz, R. T.; Böttcher, H. J.; Ante, F.; Zschieschang, Y.; Kern, K.; Klauk, H. Top-Gate ZnO Nanowire Transistors and Integrated Circuits with

Ultrathin Self-Assembled Monolayer Gate Dielectric. *Nano Lett.* **11**, 5309-5315, (2011).

1.12 Zhang, Z.; Cao, R.; Wang, C.; Li, H. -B.; Dong, H.; Wang, W. -H.; Lu, F.; Cheng, Y.; Xie, X.; Liu, H.; Cho, K.; Wallace, R.; Wang, W. GaN as an Interfacial Passivation Layer: Tuning Band Offset and Removing Fermi Level Pinning for III−V MOS Devices. *ACS Appl. Mater. Interfaces* **7**, 5141-5149, (2015).

1.13 Dattoli, E. N.; Wan, Q.; Guo, W.; Chen, Y.; Pan, X.; Lu, W. Fully Transparent Thin-Film Transistor Devices Based on SnO_2 Nanowires. *Nano Lett.* **7(8)**, 2464-2469, (2007).

1.14 Wang, G.; Moses, D.; Heeger, A. J. Poly(3-Hexylthiophene) Field-Effect Transistors with high Dielectric Constant Gate Insulator. *J. Appl. Phys.* **95**, 316, (2004).

1.15 Xu, W.; Cao, H.; Liang, L.; and Xu, J. Aqueous Solution-Deposited Gallium Oxide Dielectric for Low-Temperature, Low-Operating-Voltage Indium Oxide Thin-Film Transistors: A Facile Route to Green Oxide Electronics. *ACS Appl. Mater. & Interfaces* **7**, 14720-14725, (2015).

1.16 Bergeron, H.; Sangwan, V. K.; McMorrow, J. J.; Campbell, G. P.; Balla, I.; Liu, X.; Bedzyk, M. J.; Marks, T. J.; Hersam, M. C. Chemical Vapor Deposition of Monolayer MoS_2 Directly on Ultrathin Al_2O_3 for Low-Power Electronics. *Appl. Phys. Lett.* **110**, 053101, (2017).

1.17 Wang, Y; Wang, H.; Ye, C.; Zhang, J.; Wang, H.; Jiang, Y. Interfacial Reaction and Electrical Properties of HfO_2 Film Gate Dielectric Prepared by Pulsed Laser Deposition in Nitrogen: Role of Rapid Thermal Annealing and Gate Electrode. *ACS Appl. Mater. Interfaces* **3**, 3813-3818 (2011).

1.18 Park.Y. M.; Desai, A.; Salleo, A. Solution-Processable Zirconium Oxide Gate Dielectrics for Flexible Organic Field Effect Transistors Operated at Low Voltages. *Chem. Mater.* **25**, 2571-2579, (2013).

1.19 Cho, M. -H.; Ko, D. -H.; Choi, Y. G.; Jeong, K.; Lyo, I. W.; Noh, D. Y.; Kim, H. J.; Whang, C. N. Structural and Electrical Characteristics of Y_2O_3 Flms Grown on Oxidized Si(100) Surface. *J. Vac. Sci. Technol. A* **19**, 192, (2001).

1.20 Aizawa, K.; Park, B. -E.; Kawashima, Y.; Takahashi, K.; Ishiwara, H. Impact of HfO_2 Buffer Layers on Data Retention Characteristics of Ferroelectric-Gate Field-Effect Transistors. *Appl. Phys. Lett.* **85(15)**, 3199-3201, (2004).

1.21 Shen, P. C.; Lin, C.; Wang, H.; Teo, K. H.; and Kong, J. "Ferroelectric memory field-effect transistors using CVD monolayer MoS_2 as resistive switching channel" *Appl. Phys. Lett.* **116**, 033501, (2020).

1.22 Pintilie, L.; and Lisca, M. "Polarization reversal and capacitance-voltage characteristic of epitaxial $Pb(Zr,Ti)O_3$ layers" *Appl. Phys. Lett.* **86**, 192902, (2005).

1.23 Mueller, S.; Mueller, J.; Singh, A.; Riedel, S.; Sundqvist, J.; Schroeder, U.; and Mikolajick, T. "Incipient Ferroelectricity in Al-Doped HfO_2 Thin Films" *Adv. Func. Mater.* **22**, 2412-2417, (2012).

1.24 Daniel, E. D.; Mee, C. D.; Clark, M. H. "*Magnetic Recording The First 100 Years*" *IEEE Press.* (1999).

1.25 Duan, Y.; Liang, L.; Lv, K.; Li, Q.; Li, M. "TiO_2 faceted nanocrystals on the nanofibers: Homojunction TiO_2 based Z-scheme photocatalyst for air purification" *Appl. Surface Science* **456**, 817-826, (2018).

1.26 Ingel, R. P.; Lewis, D.; bender, B. A.; Rice, R. W. "Temperature Dependence of Strength and Fracture Toughness of ZrO_2 Single Crystals" *Journal of American Ceramic Society* **65**, c150-c152, (1982).

1.27 Du, Y.; Frischat, G. H. "Atomic force microscopy study on the anatase crystallization of long term stored Al_2O_3-TiO_2-SiO_2 coatings on glass" *J. Mater. Science* **35**, 2561-2564, (2000).

1.28 Li, X.; He, J.; and Liu, W. "Broadband anti-reflective and water-repellent coatings on glass substrates for self-cleaning photovoltaic cells" *Materials Research Bulletin* **48**, 2522-2528, (2013).

1.29 Traina, C. A.; and Schwartz, J. "Surface Modification of Y_2O_3 Nanoparticles" *Langmuir* **23(18)**, 9158-9161, (2007).

1.30 Yaghoubi, H.; Taghavinia, N.; and Alamdari, E. K. "Self cleaning TiO_2 coating on polycarbonate: Surface treatment, photocatalytic and nanomechanical properties" *Surface and Coating Technology* **204**, 1562-1568, (2010).

1.31 Popoola, A. P. I.; Aigbodion, V. S.; and Fayomi, O. S. I. "Anti-corrosion coating of mild steel using ternary Zn-ZnO-Y_2O_3 electro-depositon" *Surface and Coating Technology* **306(B)**, 448-454, (2016).

1.32 Kingon, A. I., Maria, J.-P.; and Streiffer, S. K. "Alternative dielectrics to silicon dioxide for memory and logic devices", *Nature* **406**, 1032–1038, (2000).

1.33 Robertson, J. "High dielectric constant gate oxides for metal oxide Si transistors" *Rep. Prog. Phys.* **69**, 327–396, (2006).

1.34 Kim, S. K., Lee, S. W., Han, J. H., Lee, B., Han, S.; and Hwang, C. S. "Capacitors with an equivalent oxide thickness of o0.5 nm for nanoscale electronic semiconductor memory", *Adv. Funct. Mater.* **20**, 2989–3003, (2010).

1.35 Lee, C.-H., Hur, S.-H., Shin, Y.-C., Choi, J.-H., Park, D.-G.; and Kim, K. "Charge-trapping device structure of SiO_2/SiN/high-k dielectric Al_2O_3 for high-density flash memory", *Appl. Phys. Lett.* **86**, 152908, (2005).

1.36 Robertson, J. "Band offsets of wide-band-gap oxides and implications for future electronic devices" *J. Vac. Sci. Technol. B*, **18(3)**, 1785-1791, (2000).

1.37 Rodríguez-Castañeda, C. A.; Moreno-Romero, P. M.; Corpus-Mendoza, A. N.; Suarez-Campos, G.; Miranda- Hernandez, M.; Sotelo-Lerma, M.; Hu, H. "Thermal Evaporation−Oxidation Deposited Aluminum Oxide as an Interfacial Modifier to Improve the Performance and Stability of Zinc Oxide-Based Planar Perovskite Solar Cells", *ACS Appl. Energy Mater.* **3**, 9618-9627, (2020).

1.38 Yang, C.; Fan, H.; Xi, Y.; Chen, J.; and Li, Z. "Effects of depositing temperatures on structure and optical properties of TiO_2 film deposited by ion beam assisted electron beam evaporation", *Applied Surface Science* **254**, 2685-2689, (2008).

1.39 Shahjahan, M.; Takahashi, N.; Sawada, K.; and Ishida, M. "Fabrication and Electrical Characterization of Ultrathin Crystalline Al_2O_3 Gate Dielectric Films on Si(100) and Si(111) by Molecular Beam Epitaxy", *Jpn. J. Apl. Phys.* 41, 1474-1477, (2002).

1.40 Fisher, P.; Maksimov, O.; Du, H.; Heydemann, V. D.; Skowronski, M.; and Salvador, P. A. "Growth, structure, and morphology of TiO_2 films deposited by molecular beam epitaxy in pure ozone ambients", *Microelectronics Journal* **37**, 1493-1497, (2006).

1.41 Shi, L.; Xia, Y. D.; Xu, B.; Yin, J.; and Liu, Z. G. "Thermal stability and electrical properties of titanium-aluminum oxide ultrathin films as high-k gate dielectric materials" *J. Appl. Phys.* **101**, 034102, (2007).

1.42 Rao, M. C.; Ravindranadh, K.; and Shekhawat, M. S. "Structural and electrical properties of TiO_2 thin films" *J. Appl. Phys.* **1728**, 020077, (2016).

1.43 Serna R.; and Afonso, C. N. "In situ growth of optically active erbium doped Al_2O_3 thin films by pulsed laser deposition", *Appl. Phys. Lett.* **69**, 1541, (1996).

1.44 Andersson, J. M.; Wallin, E.; Helmersson, U.; Kreissig, U.; Münger, E. P. "Phase Control of Al_2O_3 Thin Films Grown at Low Temperatures" *Thin Solid Films* **513**, 57, (2006).

1.45 Alberti, A.; Smecca, E.; Sanzaro, S.; Bongiorno, C.; Giannazzo, F.; Mannino, G.; Magna, A. L. "Nanostructured TiO_2 Grown by Low-Temperature Reactive Sputtering for Planar Perovskite Solar Cells" *ACS Appl. Energy Mater.* **2**, 6218-6229, (2019).

1.46 Auciello, O.; Fan, W.; Kabius, B.; Saha, S.; Carlisle, J. A.; Chang, R. P. H.; Lopez, C.; Irene, E. A.; and Baragiola, R. A. "Hybrid titanium–aluminum oxide layer as alternative high- gate dielectric for the next generation of complementary metal–oxide–semiconductor devices" *Appl. Phys. Lett.* **86**, 042904, (2005).

1.47 Chrysson, C. E.; Pitt, C.W. "Al_2O_3 Thin Films by Plasma-Enhanced Chemical Vapour Deposition Using Trimethyl-Amine alane (TMAA) As the Al Precursor" *Appl. Phys. A* **65**, 469-475, (1997).

1.48 Perkins, C. Y.; Mansergh, R. H.; Ramos, J. C.; Nanayakkara, C. E.; Park, D. -H.; Ferron, S. G.; Fullmer, L. B.; Arens, J. T.; Gutierrez-Higgins, M. T.; Jones, Y. R.; Lopez, J. I.; Rowe, T. M.; Whitehurst, D. M.; Nyman, M.; Chabal, Y. J.; Keszler, D. A. "Low-index, Smooth Al_2O_3 Films by Aqueous Solution Process" *Optical Material Express* **7**, 273-278, (2017).

1.49 Shamala, K. S.; Murthy, L. C. S.; Radhakrishna, M. C.; Rao, K. N. "Characterization of Al_2O_3 Thin Films Prepared by Spray Pyrolysis Method for Humidity Sensor" *Sens. Actuators A* **135**, 552-557, (2007).

1.50 Lei, L.; Chu, H. P.; Hu, X.; Yue, P. -L. "Preparation of Heterogeneous Photocatalyst (TiO2/Alumina) by Metallo-Organic Chemical Vapor Deposition" *Ind. Eng. Chem. Res.* **38**, 3381-3385, (1999).

1.51 Sechrist, Z. A.; Schwartz, B. T.; Lee, J. H.; McCormick, J. A.; Piestun, R.; Park, W.; George, S. M. "Modification of Opal Photonic Crystals Using Al_2O_3 Atomic Layer Deposition" *Chem. Mater.* **18**, 3562-3570, (2006).

1.52 Nguyen, D. D.; and Suzuki, T.-K. "Interface charge engineering in AlTiO/AlGaN/GaN metal–insulator–semiconductor devices" *J. Appl. Phys.* **127**, 094501, (2020).

1.53 Jõgi, I.; Ritala, M.; and Leskelä, M. "Electrical Characterization of $Al_xTi_yO_z$ Mixtures and Al_2O_3-TiO_2-Al_2O_3 Nanolaminates", *J. Appl. Phys.* **102**, 114114, (2007).

1.54 Kawaharamura, T.; Uchida, T.; Sanada, M.; Furuta, M. "Growth and Electrical Properties of AlO_x Grown by Mist Chemical Vapor Deposition" *AIP Adv.* **3**, 032135, (2013).

1.55 Kim, D. -H.; Jeong, H. -J.; Park, J.; Park, J. -S. "The Effect of Solvent Water Content on the Dielectric Properties of Al_2O_3 Films Grown by Atmospheric Pressure Mist-CVD" *Ceram. Int.* **44**, 459-463, (2018).

1.56 Yatabe, Z.; Nishiyama, K.; Tsuda, T.; Nishimura, K.; and Nakamura, Y. "Synthesis and characterization of mist chemical vapor deposited aluminum titanium oxide films", *Jpn. J. Appl. Phys.* **58**, 070905, (2019).

1.57 Low, R. S.; Asubar, J. T.; Baratov, A.; Kamiya, S.; Nagase, I.; Urano, S.; Kawabata, S.; Tokuda, H.; Kuzuhara, M.; Nakamura, Y.; Naito, K.; Motoyama, T.; and Yatabe, Z. "GaN-based MIS-HEMTs with Al_2O_3 dielectric deposited by low-cost and environmental-friendly mist-CVD technique" *Appl. Phys. Express* **14**, 031004, (2021).

1.58 Kim, B.-H.; Lee, J.-Y.; Choa, Y.-H.; Higuchi, M.; Mizutani, N. "Preparation of TiO_2 thin film by liquid sprayed mist CVD method", *Materials Science and Engineering: B* **107**, 289-294, (2004).

1.59 Kawaharamura, T. "Physics on development of open-air atmospheric pressure thin film fabrication technique using mist droplets: Control of precursor flow", *Jpn. J. Appl. Phys.* **53**, 05FF08, (2014).

1.60 Pinna, N.; Garnweitner, G.; Antonietti, M.; and Niederberger, M. "A General Nonaqueous Route to Binary Metal Oxide Nanocrystals Involving a C-C Bond Cleavage", *J. AM. CHEM. SOC.* 127, 5608-5612, (2005).

1.61 Czech, Z.; Wojciechowicz, M. "The crosslinking reaction of acrylic PSA using chelate metal acetylacetonates", *European Polymer Journal* 42, 2153-2160, (2006).

1.62 Zhang, Q.; and Li, C. "Pure Anatase Phase Titanium Dioxide Films Prepared by Mist Chemical Vapor Deposition", *Nanomaterials* **8**, 827, (2018).

1.63 Win, T. Z.; Katsuhiko Inaba, K.; Kobayashi, S.; Furukawa, T.; Kanetake, Y.; Miwa, S.; Hashishin, T.; and Nakamura, Y. "Improvement of tin oxide single

crystal on an m-plane sapphire substrate by mist chemical vapor deposition", Jpn. *J. Appl. Phys.* **59**, 095503, (2020).

1.64 Nishinaka, H.; Kamada, Kameyama, N; and Fujita, S. "Epitaxial ZnO Thin Films on a-Plane Sapphire Substrates Grown by Ultrasonic Spray-Assisted Mist Chemical Vapor Deposition", *Jpn. J. Appl. Phys.* **48**, 121103, (2009).

1.65 Xu, Y.; An, Z.; Zhang, L.; Feng, Q.; Zhang, J.; Zhang, C.; and Hao, Y. "Solar blind deep ultraviolet β-Ga_2O_3 photodetectors grown on sapphire by the Mist-CVD method", *Optical Materials Express* **8**, 2941-2947, (2018).

1.66 Scott, J. I.; Martinez-Gazoni, R. F.; Allen, M. W.; and Reeves, R. J. "Optical and electronic properties of high-quality Sb-doped SnO_2 thin films grown by mist chemical vapor deposition", *J. Appl. Phys.* **126**, 135702, (2019).

1.67 Park, J.; Oh, K.-T.; Kim, D.-H.; Jeon, H.-J.; Park, Y. C.; Kim, H.-S.; and Park, J.-S. "High-Performance Zinc Tin Oxide Semiconductor Grown by Atmospheric-Pressure Mist-CVD and the Associated Thin-Film Transistor Properties", *ACS Appl. Mater. Interfaces* **9**, 20656-20663, (2017).

1.68 Ikenoue, T.; Inoue, J.; Miyake, M.; and Hirato, T. "Epitaxial growth of undoped and Li-doped NiO thin films on α-Al_2O_3 substrates by mist chemical vapor deposition", *J. Cryst. Growth* **507**, 379-383, (2019).

1.69 Horie, R.; Nishinaka, H.; Tahara, D.; Yoshimoto, M. "Epitaxial growth of γ-$(Al_xGa_{1-x})_2O_3$ alloy thin films on spinel substrates via mist chemical vapor deposition", *J. Alloys Comp.* **851**, 156927, (2021).

1.70 Chen, Z.; Arita, M.; Saito, K.; Tanaka, T.; and Guo, Q. "Epitaxial growth of $(Al_xGa_{1-x})_2O_3$ thin films on sapphire substrates by plasma assisted pulsed laser deposition", *AIP Adv.* **11**, 035319, (2021).

1.71 Oha, K.-T.; Kim, H.-Y.; Kim, D.-H.; Han, J. H.; Park, J.; and Park, J.-S. "Facile synthesis of AlO_x dielectrics via mist-CVD based on aqueous solutions", *Ceram. Int.* **43**, 8932-8937, (2017).

1.72 Uchida, T.; Kawaharamura, T.; Shibayama, K.; Hiramatsu, T.; Orita, H.; and Fujita, S. "Mist chemical vapor deposition of aluminum oxide thin films for rear surface passivation of crystalline silicon solar cells", *Appl. Phys. Express* **7**, 021303, (2014).

1.73 Aoki, Y.; Kunitake, T.; Nakao, A. "Sol-Gel Fabrication of Dielectric HfO_2 Nano-Films; Formation of Uniform, Void-Free Layers and Their Superior Electrical Properties", *Chem. Mater.* **17 (2)**, 450–458, (2005).

1.74 Lee, H. J.; Moon, T.; Kang, S.; Kim, W.; Hwang, C. S. “Threshold Voltage Modulation in a Transistor with a Two-Dimensional Electron Gas Channel at the Interface between $Al_2O_3$and Sub-5 Nm ZnO Films”, *ACS Appl. Electron. Mater.* **3**, 3247-3255, (2021).

1.75 Lee, S.; Song, E. B.; Kim, S.; Seo, D. H.; Seo, S.; Won Kang, T.; Wang, K. L. “Impact of Gate Work-Function on Memory Characteristics in $Al_2O_3/HfO_x/Al_2O_3$/Graphene Charge-Trap Memory Devices”, *Appl. Phys. Lett.* **2012**, *100* (2), 1–5.

1.76 Song, J. G.; Kim, S. J.; Woo, W. J.; Kim, Y.; Oh, I. K.; Ryu, G. H.; Lee, Z.; Lim, J. H.; Park, J.; Kim, H. “Effect of Al_2O_3 Deposition on Performance of Top-Gated Monolayer MoS_2-Based Field Effect Transistor”, *ACS Appl. Mater. Interfaces* **8 (41)**, 28130–28135, (2016).

1.77 Bergeron, H.; Sangwan, V. K.; McMorrow, J. J.; Campbell, G. P.; Balla, I.; Liu, X.; Bedzyk, M. J.; Marks, T. J.; Hersam, M. C. “Chemical Vapor Deposition of Monolayer MoS_2 Directly on Ultrathin Al_2O_3 for Low-Power Electronics”, *Appl. Phys. Lett.* **110**, 053101, (2017).

1.78 Wang, Y.; Wang, H.; Ye, C.; Zhang, J.; Wang, H.; Jiang, Y. “Interfacial Reaction and Electrical Properties of HfO_2 Film Gate Dielectric Prepared by Pulsed Laser Deposition in Nitrogen: Role of Rapid Thermal Annealing and Gate Electrode”, *ACS Appl. Mater. Interfaces* **3** (10), (2011)

1.79 Choi, C. H.; Kim, T.; Ueda, S.; Shiah, Y. S.; Hosono, H.; Kim, J.; Jeong, J. K. “High-Performance Indium Gallium Tin Oxide Transistors with an Al_2O_3 Gate Insulator Deposited by Atomic Layer Deposition at a Low Temperature of 150 °c: Roles of Hydrogen and Excess Oxygen in the Al_2O_3Dielectric Film”, *ACS Appl. Mater. Interfaces* **13 (24)**, 28451–28461, (2021).

1.80 He, G.; Gao, J.; Chen, H.; Cui, J.; Sun, Z.; Chen, X. “Modulating the Interface Quality and Electrical Properties of HfTiO/InGaAs Gate Stack by Atomic-Layer-Deposition-Derived Al_2O_3 Passivation Layer”, *ACS Appl. Mater. Interfaces* **6 (24)**, 22013–22025, (2014).

1.81 Hashizume, T.; Ootomo, S.; Inagaki, T.; Hasegawa, H. “Surface Passivation of GaN and GaN/AlGaN Heterostructures by Dielectric Films and Its Application to Insulated-Gate Heterostructure Transistors”, *J. Vac. Sci. Technol. B Microelectron. Nanom. Struct.* **21 (4)**, 1828, (2003).

1.82 Khan, M. A.; Hu, X.; Tarakji, A.; Simin, G.; Yang, J.; Gaska, R.; Shur, M. S. "AlGaN/GaN metal–oxide–semiconductor heterostructure field-effect transistors on SiC substrates", *Appl. Phys. Lett.* **77 (9)**, 1339–1341, (2000).

1.83 Robertson, J. "High Dielectric Constant Gate Oxides for Metal Oxide Si Transistors", *Reports Prog. Phys.* **69 (2)**, 327–396, (2006).

1.84 Robertson, J. "Band Offsets of Wide-Band-Gap Oxides and Implications for Future Electronic Devices", *J. Vac. Sci. Technol. B Microelectron. Nanom. Struct.* **18 (3)**, 1785, (2000).

1.85 Mahata, C.; Mallik, S.; Das, T.; Maiti, C. K.; Dalapati, G. K.; Tan, C. C.; Chia, C. K.; Gao, H.; Kumar, M. K.; Chiam, S. Y.; Tan, H. R.; Seng, H. L.; Chi, D. Z.; Miranda, E. "Atomic Layer Deposited $(TiO_2)_x(Al_2O_3)_{1-x}/In_{0.53}Ga_{0.47}As$ Gate Stacks for III-V Based Metal-Oxide-Semiconductor Field-Effect Transistor Applications", *Appl. Phys. Lett.* **100 (6)**, 2–6, (2012).

1.86 Mallik, S.; Mahata, C.; Hota, M. K.; Dalapati, G. K.; Chi, D. Z.; Sarkar, C. K.; Maiti, C. K. "$HfAlO_x$ High-k Gate Dielectric on SiGe: Interfacial Reaction, Energy-Band Alignment, and Charge Trapping Properties", *Microelectron. Eng.* **87 (11)**, 2234–2240, (2010).

1.87 Lima, A. F.; Dantas, J. M.; Lalic, M. V. "An Ab-Initio Study of Electronic and Optical Properties of Corundum Al_2O_3 Doped with Sc, Y, Zr, and Nb", *J. Appl. Phys.* ***112*** **(9)**, (2012).

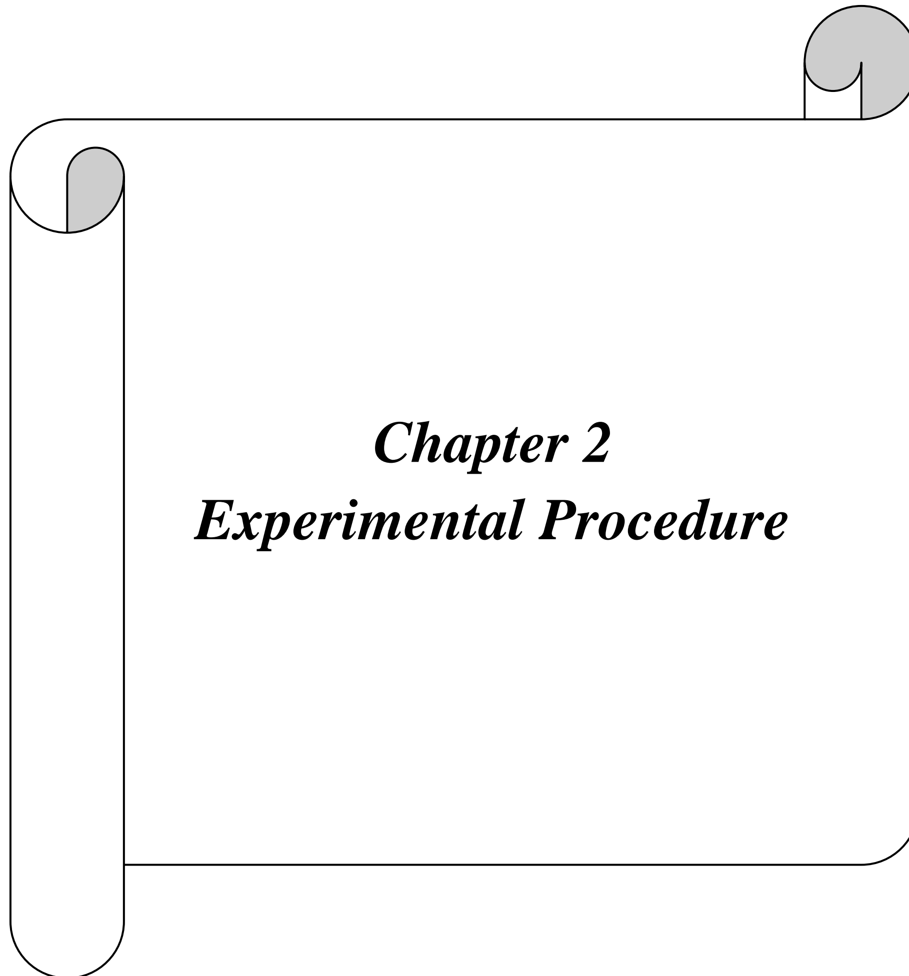

Chapter 2
Experimental Procedure

Chapter 2: Experimental and Analytic methodologies

In this chapter, the mist-CVD system is briefly discussed, including each part of the mist-CVD system. A brief discussion over the fabrication steps of $MoSe_2$ based MIS-FET where AlO_x as the dielectric layer is also assembled. The $MoSe_2$ and As-doped WSe_2 flakes formation procedure by chemical vapor transport and direct vapor transport, respectively are also discussed. The instrument and its measurement procedure are included. The MOS capacitor structure and the important parameters extracted from C-V measurement are also discussed in the latter of this chapter. The MIS-FET parameter and their extracted phenomenon are also considered at the end of this chapter.

2.1 Mist-CVD system

Mist-CVD is one of the well-known fabrication techniques, classified as an equilibrium process, for functional thin films from solution is a starting material under open-air atmospheric pressure. First, K. Shanmugasundaram et al. utilized the mist deposition technique for patterning of liquid precursors thin films.[2.1] H. Shirai et. al. also used the chemical mist deposition (CMD) method to synthesis transparent conductive poly(3,4-ethylene dioxythiophene):poly(styrene sulfonate) (PEDOT:PSS) polymers on textured n-type crystalline (n-)Si substrates to fabricate Si photovoltaics showing improved light management.[2.2-4] Mist-CVD is the upgraded version of the CMD system by adding a furnace in the reaction unit. The basic concept of the mist-CVD system is shown in **Figure 2.1.** The mist-CVD system is usually classified into three parts, that is, a mist generation unit, a mist transport section, and a reaction unit. In addition, the reaction unit consists of a reaction chamber and a heater. The carrier gas of N_2 and the mesh bias supply belong to the transport unit. The ultrasonic transducer made from piezoelectric material plays the main role to generate mist droplets.

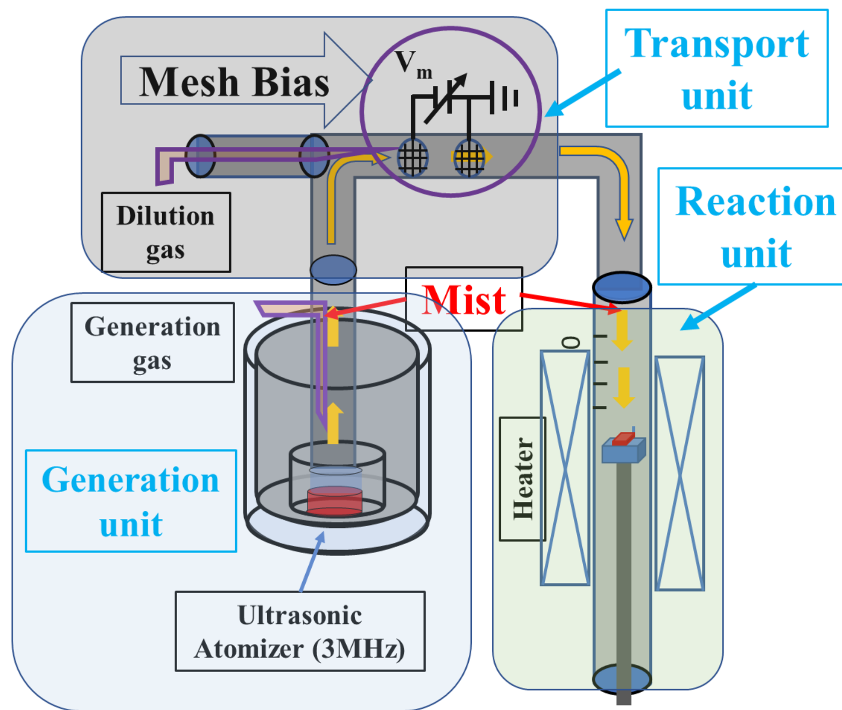

Figure 2. 1. Schematic image of mist deposition.

2.1.1 Mist generation unit

Mist particle is the key element of the mist-CVD technique. Thus, the generation of fine mist particles is the most important task to build up the mist-CVD system. One schematic of the mist generation unit is shown in **Figure 2.2**. An ultrasonic atomizer was used to generate mist particles. When a beam of ultrasound of sufficient energy is passed through a liquid and directed at an air interface, atomization of the liquid occurs according to the Rayleigh formula.[2.5] Rayleigh attributed the instability to a statistical distribution of capillary disturbance of amplitude α and wavelength λ. According to the Rayleigh formula, if $\lambda > 2\pi R$ is achieved, the particle phase breaks it up (shown in **Figure 2.3**). Liquid droplets are ejected from the surface into the surrounding. n. The first description of this phenomenon was by Wood and Loomis,[2.6] who observed fog formation from an ultrasonic fountain and also off thin liquid films on a vibrating glass bulb. Two major hypotheses have been proposed to explain the mechanism of liquid disintegration during ultrasonic atomization, namely the capillary wave hypothesis and cavitation hypothesis. The capillary wave hypothesis is based on Taylor's instability criteria.[2.7] The strong correlations between mean droplet size and capillary wavelength favor the capillary wave theory. Lang[2.8] measured the surface disturbances by

photographing the peaks of the capillary waves on the vibrating surface. The cavitation hypothesis is generally applied to high frequency (16 kHz–2 MHz) and high-energy intensity (W/m^2) systems. When the liquid film is sonicated, cavitation bubbles are formed in the liquid film provided the liquid film on the vibrating surface has some minimum thickness. During the implosive collapse of these cavities, especially cavities near the surface of the liquid, high-intensity hydraulic shocks are generated. These hydraulic shocks initiate the disintegration of the liquid film and cause direct ejection of the droplets.

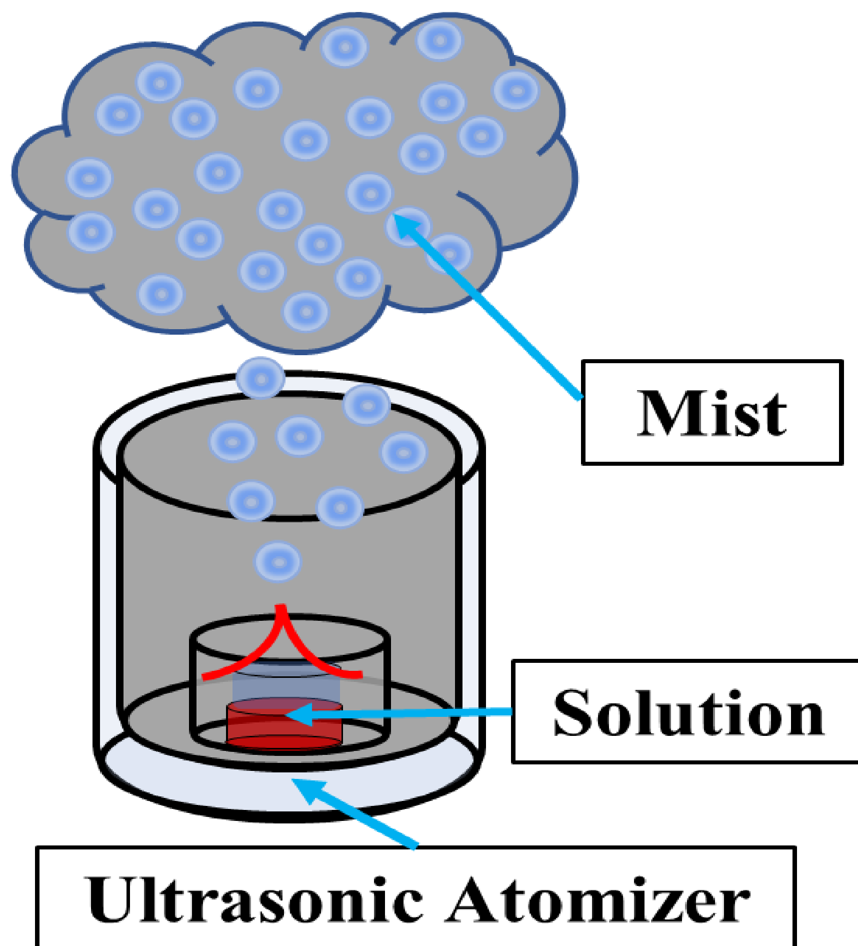

Figure 2. 2. Droplet generator using the ultrasonic vibrator.

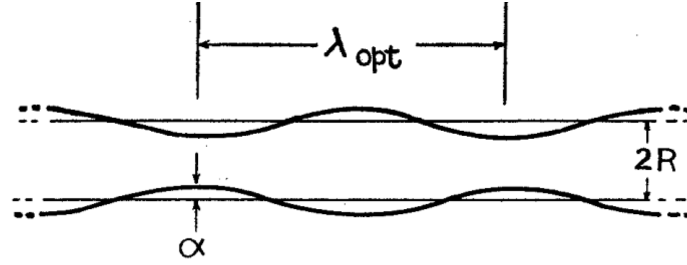

Figure 2. 3. Disturbance of liquid cylinder which leads to break-up as predicted by Rayleigh.[2.5]

Topp and Eisenklam[2.9] have listed the effect of the different frequencies but there has been no concrete information about the effect of liquid phase viscosity, density, and flow rates. Finally, Lang[2.8] establishes an equation and found that the drop size depends on the frequency of the surface standing wave at the liquid interface, which is due to the piezoelectric element. The Lang equation expressed as;

$$d_p = 0.34\left(\frac{8\pi\sigma}{\rho f^2}\right)^{1/3} \qquad (2.3)$$

where d_p is denoted by the droplet size, σ is the surface tension in the liquid surface, ρ is the density of the liquid, *f* is the excitation frequency.

2.1.2 Mist transport unit

In order to obtain high-quality and uniform thin films, the control of the precursor flow is essential. The flow of mist droplets is very essential to control as the mist droplets have no initial velocity and are floating in the air. This is the marked difference from the spray method, in which the mist droplets have a high velocity making it difficult to control the flow. In this work, the flow of N_2 gas and mesh bias supply is employed to transport the mist droplets (shown in **Fig. 2.4 (a)).**

The flow of N_2 supply is determined by the residence time of mist precursors which enhances the diffusivity of mist precursors and found that a higher flow of N_2 supply capable to decrease the mist size. On the other side, mesh DC bias supply between two mesh electrodes with a 2 cm distance for charging mist precursors. A high-speed camera image revealed a marked increase in the traveling speed with a decrease in the density of the mist precursors (**Figure 2.4 (b)**. These results originate from that some

of the charged mists were trapped at the negatively dc biased front electrode and untrapped mist particles after passing the front electrode were collided with each other because of their acceleration due to high electric field, resulting in suppressing the mist flux but enhance the traveling speed.

(a) (b)

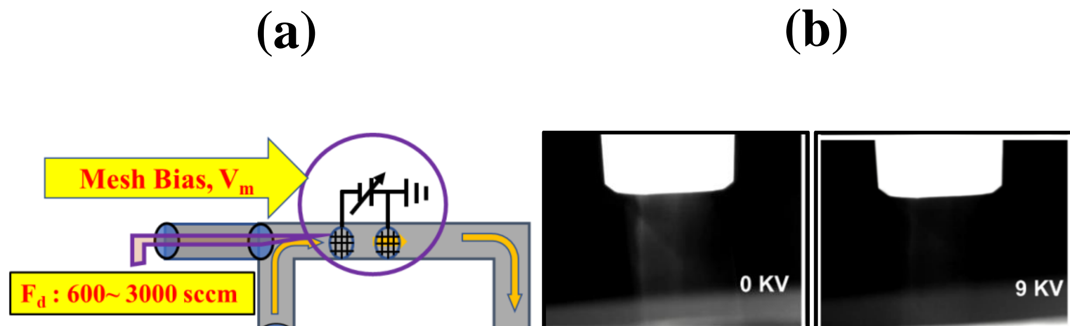

Figure 2. 4. **(a)** Mist transport unit including carrier gas flow and mesh bias supply. **(b)** High-speed camera images at the inlet of the tubular furnace for different values of mesh bias V_m.

2.1.3 Reaction unit

The reaction unit is one of the main sections of the mist-CVD system which consists of a reaction chamber where film deposition has been taken place, a heater to carry thermal energy for decompose the precursors and facilitate the absorbance of the mist droplets on the substrate in the growth regimes, and an exhaust system used to away the unreacted precursors. A schematic of reaction unit with different reaction scheme shown in **Figure 2.5**. During the transportation of mist precursors in the reaction chamber, the average size of the mist droplets decreased from 40-500 nm to a few nanometers under the influence of heat, evapotranspiration, and burst. Due to gravity and absorption, the mist precursors moved effectively onto the substrate which was set on the growth zone.

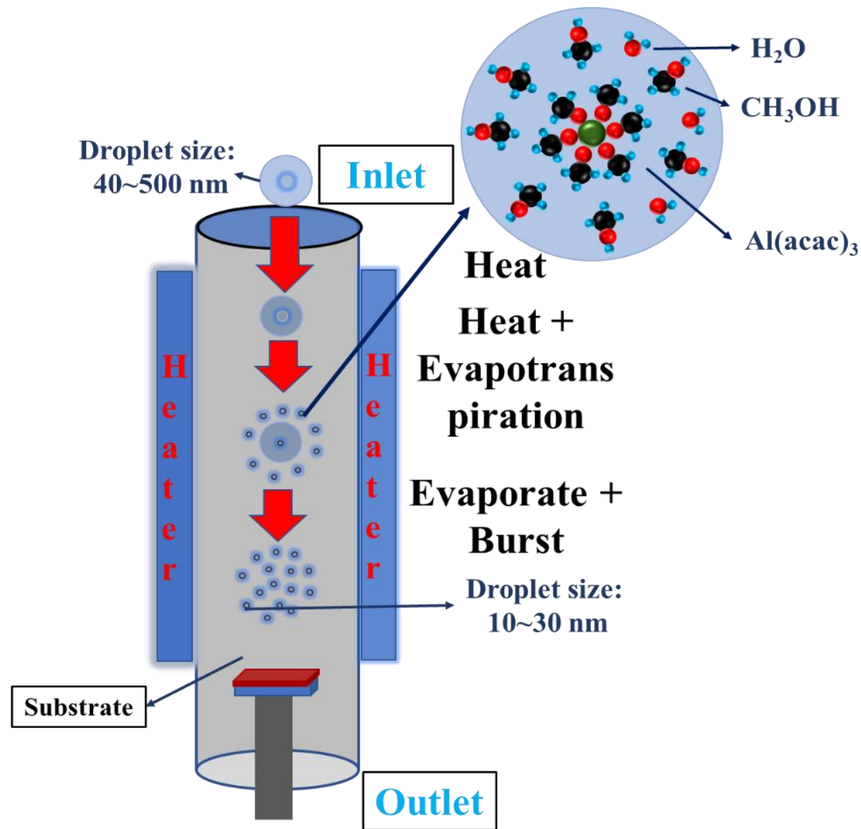

Figure 2. 5. Schematic diagram of reaction unit.

2.2 $MoSe_2$-based MIS-FET fabrication

2.2.1 Deposition of AlO_x thin films by mist-CVD

A schematic presentation of the apparatus of the mist-CVD system used in this study is shown in Figure 2.6. The deposition system consisted of an ultrasonic atomizer (operating at a frequency of 3 MHz and duty ratio of 50:50), a quartz tube, a tubular furnace, and a substrate holder. Additionally, an n-Si(100) substrate having a thickness of 250±5 μm and a donor density of 3.9×10^{16} cm^{-3} was used in this study. The substrate holder was placed at a distance of 14 cm from the inlet of the tubular furnace; the maximum temperature was attained such a placement. $Al(acac)_3$ was used as the starting material, which was dissolved in a CH_3OH/H_2O mixture (7:3 volume ratio). The $Al(acac)_3$ mist generated by the atomizer was transported to a glass tube with two mesh electrodes (SUS304, 400 mesh). The electrodes were placed at a distance of 2 cm from each other and used to supply DC bias (V_m) to obtain negatively charged mist precursors. Furthermore, N_2 was employed as a mist generation and dilution gas. The

growth conditions are summarized in Table 1. AlO_x film deposition was assessed by varying F_d, T_f, solution concentration, and V_m. The flow of N_2 for mist generation (F_s) was constant at 500 sccm. A mist was generated at 40 V and 0.37 A, with a duty ratio of 50:50.

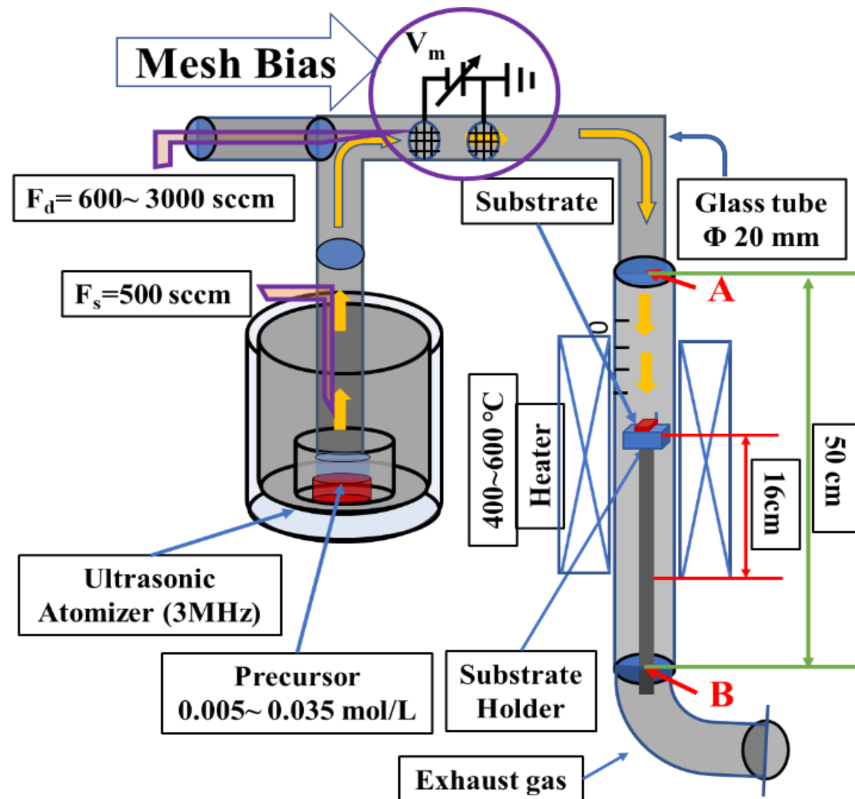

Figure 2. 6. Schematic diagram of the mist-CVD system.

Table 2. 1. AlO_x thin film deposition conditions.

Solute	:	$Al(acac)_3$
Solvent (mixing ratio)	:	CH_3OH: H_2O (7:3)
Solution concentration	:	0.005-0.035 mol/L
Furnace temperature, T_f	:	400- 600 °C
Mesh bias supply	:	0-9 kV
Substrate	:	n-Si
Solution gas/ flow rate, F_s	:	N_2, 500 sccm
Carrier gas/ flow rate, F_d	:	N_2, 600- 3000 sccm
Ultrasonic transducer	:	3 MHz, 40V, 0.37 A
Duty ratio	:	50:50

2.2.2 Preparation of $MoSe_2$ and As-doped WSe_2 flakes and transferred on to $Al_{1-x}Ti_xO_y$/p+-Si by mechanically exfoliation technique

$MoSe_2$ and arsenic (As)-doped WSe_2 thin layers were exfoliated from their bulk single crystals, which were grown by chemical vapor transport (CVT) and direct vapor transport processes, respectively. **Figure 2.7** (a) shows the setup of a typical CVT method. For the growth of $MoSe_2$ flakes, molybdenum (Mo) and selenium (Se) powders were introduced into a quartz ampoule with iodide (I_2), which works as the transport agent. The outer diameter of the ampoule is 2.5 cm, the wall thickness is 0.15 cm, and the length is about 19 cm. The ampoule was evacuated to the pressure about 1×10^{-4} Pa with cooling source materials by liquid N_2. Then the ampoule was sealed and set in a horizontal electric tube furnace having three (source, middle and sink) heating zones. First, the quartz ampoule was heated for 3 days with a reverse temperature gradient of 850 °C (source), 950 °C (middle), and 950 °C (sink) to make the middle and sink zones free from souce Mo particles. The temperature was raised by 1 °C/min. Then, the ampoule was heated for 7 days with a positive temperature gradient of 950 °C (source), 850 °C (middle), and 850 °C (sink). After the heating, the quartz ampoule was naturally cooled and taken out of the furnace, as shown in **Figure 2.7 (b). Figure 2.7 (c)** shows the $MoSe_2$ bulk crystal that grew around the middle zone of the ampoule.

(a)

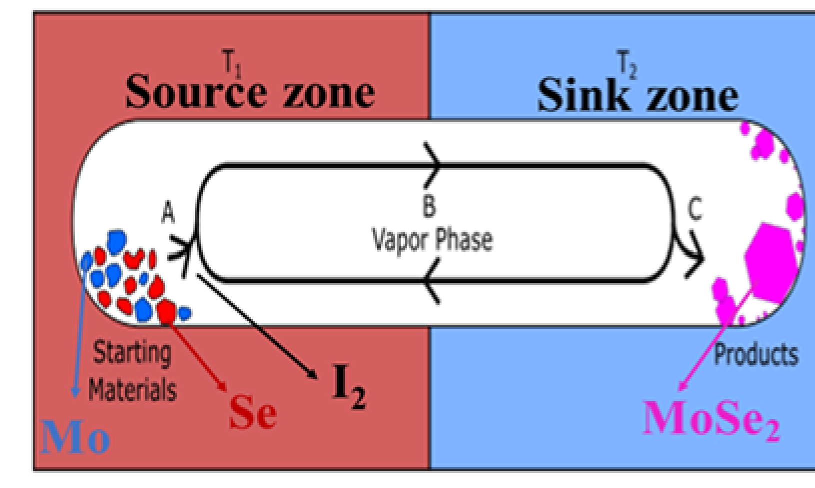

(b)

(c)

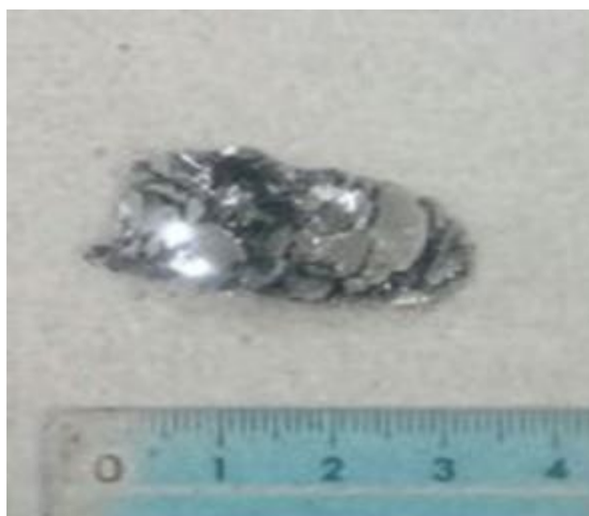

Figure 2. 7. (a) Illustration of a typical CVT. (b) $MoSe_2$ quartz ampoule after crystal growth. (c) $Mose_2$ bulk crystal grown in the quartz ampoule.

As-doped WSe_2 Flake Synthesis: Usually, MX_2 single crystals grown by the CVT method use a small amount of the halogen transport agent, which may be the source of active impurity and affect the physical properties.[2.10,2.11] In order to escape from the contamination, Al-Hilli and Evans[2.12] and Agarwal et. al.[2.13-15] introduced a direct vapor transport method without using a halogen transport agent. From the motivation to synthesize P-type As-doped WSe_2 flakes, we have used the direct vapor transport method without incorporating any halogen agents. In this experiment, As-doped WSe_2 flakes were grown without I_2 but with slightly (5-8%) excess Se to confirm the P-type

behavior, as previously reported in the literature.[2.16] To synthesize As-doped WSe_2, temperatures of source, middle and sink zones of the ampoule were chosen as 1070 °C, 1060 °C and 1060 °C, respectively. In our experiment, large flakes with the best crystallinity could be obtained around the middle part of the ampoule. Finally, p-type WSe_2 thin layers with 1% As acceptor were successfully exfoliated from the crystal.

As the second step of MIS-FET fabrication, the $MoSe_2$/As-doped WSe_2 flakes were transferred onto the AlO_x-deposited p^+-Si substrate using the mechanical exfoliation technique. As $MoSe_2/WSe_2$ is a thin-layered material with an X-M-X structure, where M referred to metal and X is devoted to the chalcogenide; the M-X bond represents an in-plain covalent bonding, and the X-X bond indicates a Van der Waals interaction. Resulting in $MoSe_2$ has great potential as used as an active layer by mechanically exfoliation technique for MIS-FET application. A microscopic image after $MoSe_2$ flakes exfoliation on AlO_x/p^{++}-Si is shown in **Figure 2.8.**

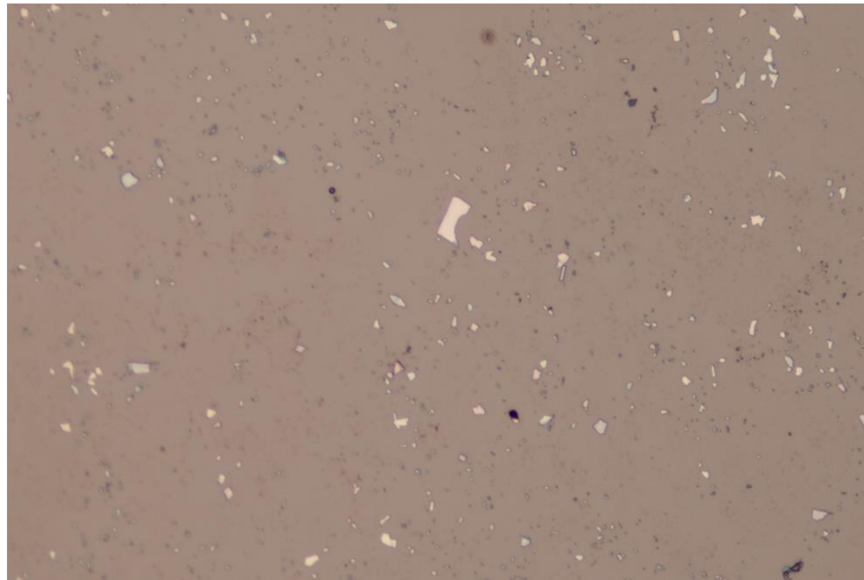

Figure 2. 8. Microscopic image of mechanically exfoliated $MoSe_2$ flakes onto AlO_x/p^{++}-Si substrate.

2.2.3 Electrodes pattering and forming on $MoSe_2$-based MIS-FET

The source/drain electrodes of gold were formed through the lift-off process using the photolithography method with a photoresist (AZ5214E) pattern. After $MoSe_2$ exfoliation, the photoresist (AZ5214E) pattern was formed on the film by using the conventional photolithography method. After masking, the photoresist was removed from the surface of the films by using tetra methyl ammonium hydroxide (NMD-3) is shown in **Figure 2.9.**

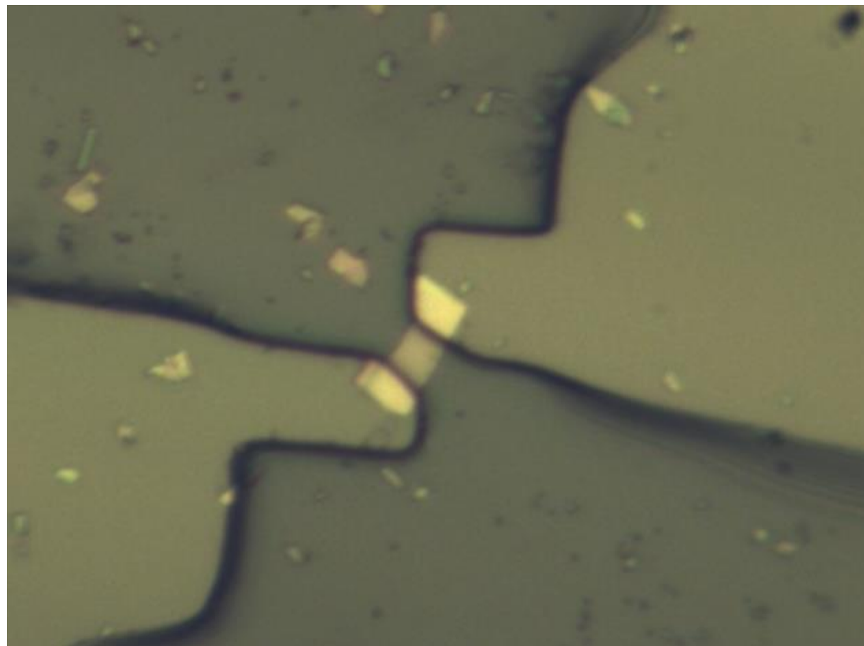

Figure 2. 9. Microscopic image of $MoSe_2$ flake after patterning.

At this stage, the gold electrodes were formed on the patterned film by using the magnetic sputtered deposition method. Finally, the gold electrodes were formed through an ultrasonic lift-off process. The optical image and schematic of the device structure of corresponding FETs are shown in **Figures 2.10(b) and (c)**.

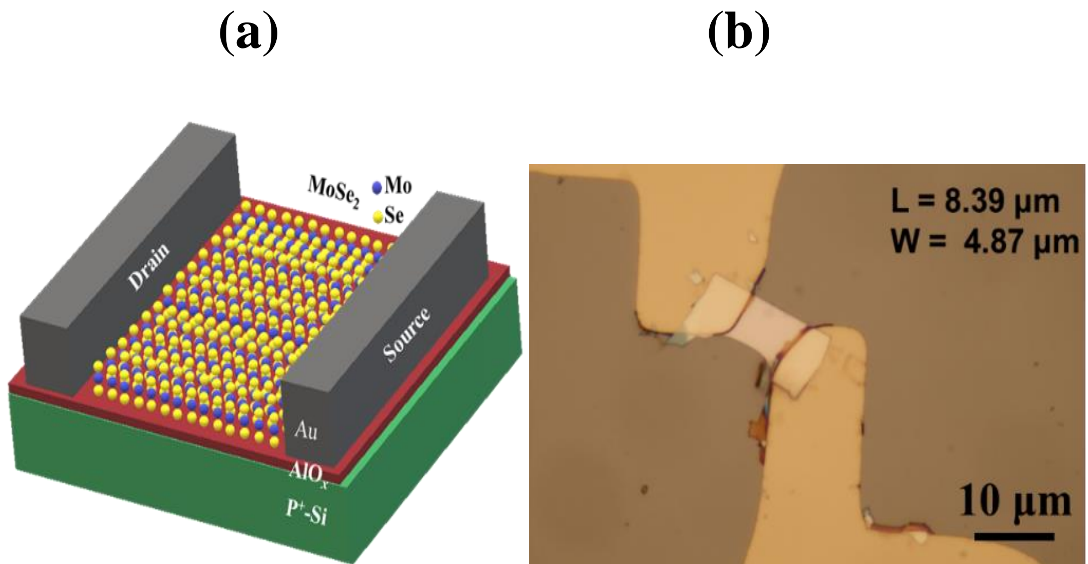

Figure 2. 10. 3D view and the microscopic image of $MoSe_2$ based MIS-FET where AlO_x is used as a dielectric layer.

2.3 Analytic methodology

2.3.1 Chemical Structure by Fourier Transform Infrared (FT-IR) Spectroscopy

Chemical structure of AlO_x, TiO_x, and $Al_{1-x}Ti_xO_y$ were measured by Fourier Transform Infrared Spectroscopy ((Shimadzu, IRT racer- 100) FT-IR Spectrometer) of wave number range 300 cm^{-1} to 4000 cm^{-1} and abscissa precision 0.01. It has high refractive materials that remove the common sources of ordinate error in FT-IR and achieve a higher order of photometric accuracy.

Infrared spectroscopy is based on the principle that molecules will absorb specific frequencies of light that match the vibrational electronic transitions of the molecule. When a molecule vibrates, the atoms move towards and away from each other at the specific frequency of light. The energy of the system is related to how much the spring is stretched or compressed. The vibrational frequency is proportional to the square root of the ratio of spring force constant to mass on the spring. Vibrational frequencies in the molecules are related to the strength of the chemical bonds and masses of the atoms. Once the sample is placed in the instrument, a beam of light is passed through the sample. The intensity of light transmitted through the sample is compared to that of the incident light at each frequency. Then absorbance may be found in this procedure.

$$A = I - T \qquad (2.5)$$

where, A is absorbance, I is the amount of incident light and T is the amount of transmittance light. In this procedure, consider no light is reflected.

In FT-IR, all frequencies of the incident radiation pass through the sample at the same time. Fourier transform is the technique used to process the raw data to present it in a way that is more easily interpreted.

Since different organic functional groups absorb light at characteristic frequencies, IR spectra give qualitative information about the composition of the sample.

Figure 2.11 shows a schematic diagram of an FT-IR set up with a beam splitter, two mirrors (one is fixed and the other is moving with a constant velocity), and the detector. Without utilizing too many details, a beam source contains various IR wavelengths light is transferred through a beam splitter. After that, half of the light beam reaches a fixed mirror and left for the mirror that moves with a constant velocity. These two split beams are then reconciled in two manners (reflect and recombine) to construct the interference pattern named constructive and reflective, respectively. After, the interference pattern (interferogram) is sent to the sample, and the detector is placed backside of the sample that catches the transmitted portion of the interferogram. A spectrum is passed through to the Fourier transform system after comparison with a reference sample beam spectrum in the detector. Finally, a Fourier transform is performed to get the full spectrum as a function of wavenumber.

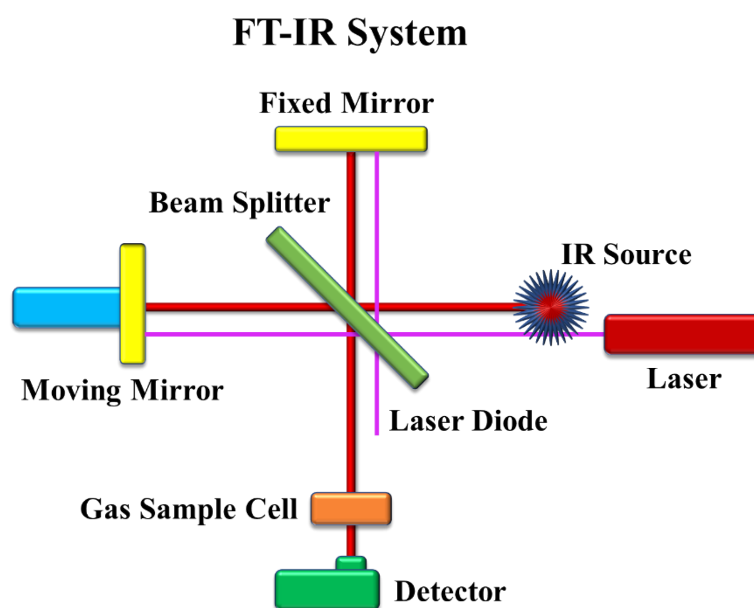

Figure 2. 11. Schematic diagram of an FT-IR.

2.3.2 Optical parameters by Spectroscopic Ellipsometry

Optical parameters were measured by laser ellipsometry (SE: Jobin Yvon, UVISEL) in the photon energy range from 1.5 eV to 5 eV, the spot size of about 1 nm, angle of incidence 70 °, sampling time 20ms as well as measured 10 times at the same location. Note that, the accuracy of the measurement ± 0.005 for refractive index and ± 0.3 nm for thickness. Spectroscopic data are obtained in the spectral range between 1.5eV (830 nm) and 5.0 eV (250 nm) with constant wavelength steps of 0.1 eV.

Electromagnetic radiation is emitted by a light source linearly polarized by a polarizer. Then, it passes through a compensator and falls on a sample. After reflection, the radiation passes through a compensator and a second polarizer, which is called an analyzer, and at last, falls into the detector. The detector measures the light which is polarized parallel to the incident plane (P-polarized) as well as polarized perpendicular to the plane (S-polarized). Ellipsometry measures the complex reflectance ratio, ρ, of a system, which may be parameterized by the thickness and refraction coefficient. The polarized state of the light incident upon the sample may be decomposed into an S and P components (mentioned above). The normalization values of the amplitude of S and P are denoted by $r_s$and r_p, respectively. Ellipsometry measures the complex reflectance ratio, ρ (a complex quantity), which is the ratio of $r_p$over r_s.

$$\rho = \frac{r_p}{r_s} \qquad (2.6)$$

This ρ can be calculated from Fresnel equations,

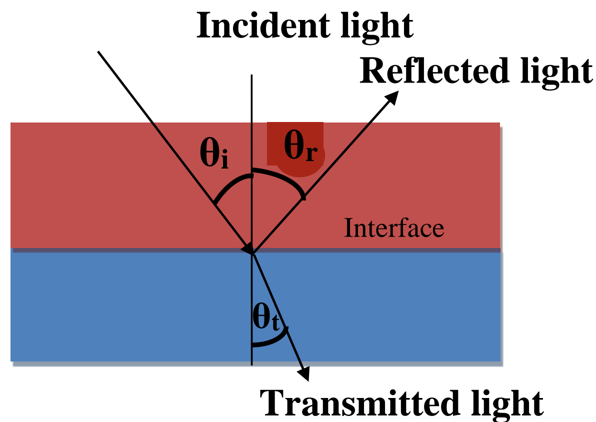

Figure 2. 12. Beam geometry for light with its electric field.

Figure 2.12. shows the beam geometry for light with its electric field. For the case of perpendicular polarized light,

Here, all fields in z direction, which is in the plane of interface.

$$\text{So, } E_i\,(y=0) + E_r\,(y=0) = E_t\,(y=0) \qquad (2.7)$$

Where E_i is the incident beam of the electric field, E_r is the reflected beam of the electric field; E_t is the transmission beam of the electric field.

The total B -the field in the plane of the interface is continuous. Here, all B - fields are in the xy - plane, so we take the x - components:

$$-B_i\,(y=0)\cos\theta_i + B_r\,(y=0)\cos\theta r = -B_t\,(y=0)\cos\theta_t \qquad (2.8)$$

Where B_i is the incident beam of the magnetic field, B_r is the reflected beam of the magnetic field, and B_t is the transmission beam of the magnetic field. θ_i is the incident angle to the normal of the plane, θ_t is the angle of transmission to the normal of the plane, and θ_r is the angle of reflection to the normal of the plane.

Ignoring the rapidly varying parts of the light wave and keeping only the complex amplitudes:

$$E_{0i} + E_{0r} = E_{0t} \qquad (2.9)$$

$$-B_{0i}\cos(\theta_i) + B_{0r}\cos(\theta_r) = -B_{0t}\cos(\theta_t) \qquad (2.10)$$

But, $B = nE / C_0$ and $\theta_i = \theta_r$

Substituting this value into equation (2.10):

$$n_i\,(E_{0r} - E_{0i})\cos(\theta_i) = -n_t\,E_{0t}\cos(\theta_t) \qquad (2.11)$$

where n_i is the refraction coefficient of incident medium and n_t is the refraction coefficient of transmission medium.

Substituting the value of E_{0t} in equation (2.11):

$$n_i\,(E_{0r} - E_{0i})\cos(\theta_i) = -n_t\,(E_{0i} + E_{0r})\cos(\theta_t) \qquad (2.12)$$

$$\text{Rearranging, } E_{0r}\,[n_i\cos(\theta_i) + n_t\cos(\theta_t)] = E_{0i}\,[n_i\cos(\theta_i) - n_t\cos(\theta_t)] \qquad (2.13)$$

Now, Reflection coefficient for perpendicular case,

$$r_p = E_{0r} / E_{0i} = [n_i \cos(\theta_i) - n_t \cos(\theta_t)] / [n_i \cos(\theta_i) + n_t \cos(\theta_t)] \quad (2.14)$$

For parallel polarized light,

$$B_{0i} + B_{0r} = B_{0t} \quad (2.15)$$

$$-E_{0i} \cos(\theta_i) + E_{0r} \cos(\theta_r) = -E_{0t} \cos(\theta_t) \quad (2.16)$$

Solving the above equations in the same manner and we get,

$$r_s = E_{0r} / E_{0i} = [n_i \cos(\theta_t) - n_t \cos(\theta_i)] / [n_i \cos(\theta_t) + n_t \cos(\theta_i)] \quad (2.17)$$

Now, solve the above two equations, and we will get the ρ.

The ellipsometry parameter ρ is only a function of the Fresnel reflection coefficients of the sample are calculated in below, and represents the total information we can obtain from a single ellipsometry measurement ρ is commonly expressed in terms of the two-real valued ellipsometry angles Ψ and Δ as follows,

$$\rho = \frac{r_p}{r_s} = \tan(\Psi)\, e^{i\Delta} \quad (2.18)$$

such that tan Ψ equals the magnitude of the ratio of the p- to s- direction complex reflection coefficients for the sample, and Δ is the phase difference between the p- and s- reflection coefficients.

The equations are used to get Ψ and Δ from the measured detector signal,

$$\tan \Psi = \sqrt{\frac{1+\alpha}{1-\alpha}\tan P}, \quad (2.19)$$

$$\cos \Delta = \frac{\beta}{\sqrt{1-\alpha^2}} * \frac{\tan P}{|\tan P|}, \quad (2.20)$$

where α and β are the Fourier coefficients and P is the azimuthal angle.

This constitutes the model of the ellipsometry measurement. Now, fit the experimental output of the true ellipsometer and compare these two outputs and find the best fit. Now, we can easily calculate the unknown compounds, like thickness and optical constants, and so on. The overall procedure is discussed below.

In an ellipsometry system, Optical experiments never directly measure the sample parameters of interest (thickness, optical constants, refractive index, extinction coefficient etc); rather they measure some quantity that is a function of the parameter of the interest. This procedure may be divided into the following steps, as illustrated in **Fig.2.10 (a)** below.

Measurement: First, the sample is measured. Thus, the ellipsometry measures the reflectance ratio *p* of the system, which may be parametrized by the amplitude component Ψ and the phase difference Δ. A SE measurement parameter are schematized in **Figure 2.13 (a)**.

Model: Having obtained optical measurements, we must now construct a model from which we can accurately predict what we should measure from a sample of known properties. This model should contain some known parameters, such as the wavelength of the incident light, the incident beam polarization state, and the angle of incidence. The model should also contain some free parameters used to fit the data. The single classical oscillator model was used in this study. The single classical model is based on the single Lorentz and Drude oscillators, expressed as;

$$\tilde{\varepsilon}(\omega) = \varepsilon_\infty + \frac{(\varepsilon_s - \varepsilon_\infty)\cdot \omega_t^2}{\omega_t^2 - \omega^2 + i\cdot\Gamma_0\cdot\omega} + \frac{\omega_p^2}{-\omega^2 + i\cdot\Gamma_d\cdot\omega} + \sum_{j=1}^{2}\frac{f_j\cdot\omega_{0j}^2}{\omega_{0j}^2 - \omega^2 + i\cdot\gamma_j\cdot\omega}$$

Where The constant ε_α is the high-frequency dielectric constant. Generally, $\varepsilon_\alpha = 1$ but can be greater than 1 if oscillators in higher energies exist and are not taken into account. The constant ε_s ($\varepsilon_s > \varepsilon_\alpha$) gives the value of the static dielectric function at a zero frequency. The difference $\varepsilon_s - \varepsilon_\alpha$ represents the strength of the single oscillator. ω_t (in eV) is the resonant frequency of the oscillator, when ω_t increases then the peak is shifted to higher photon energies. Γ_0 (in eV) is the broadening of each oscillator also known as the damping factor. The damping effect is due to the absorption process involving transitions between two states.

Fit Model to Measured Data: Using an iterative procedure (least-squares minimization) unknown optical constants and/or thickness parameters are varied, and Ψ and **Δ** values are calculated using the Fresnel equations. The calculated Ψ and **Δ**

values which match the experimental data best provide the optical constants and thickness parameters of the sample.

Evaluate the Best-fit model: To evaluate the best fitting different arrangements were conducted. Different arrangements of the layer for AlO_x are shown in **Figure 2.13 (b).** By tuning the thickness, void area, and different layer schemes, the best fitting model was chosen to obtain the optical constant of the sample.

(a)

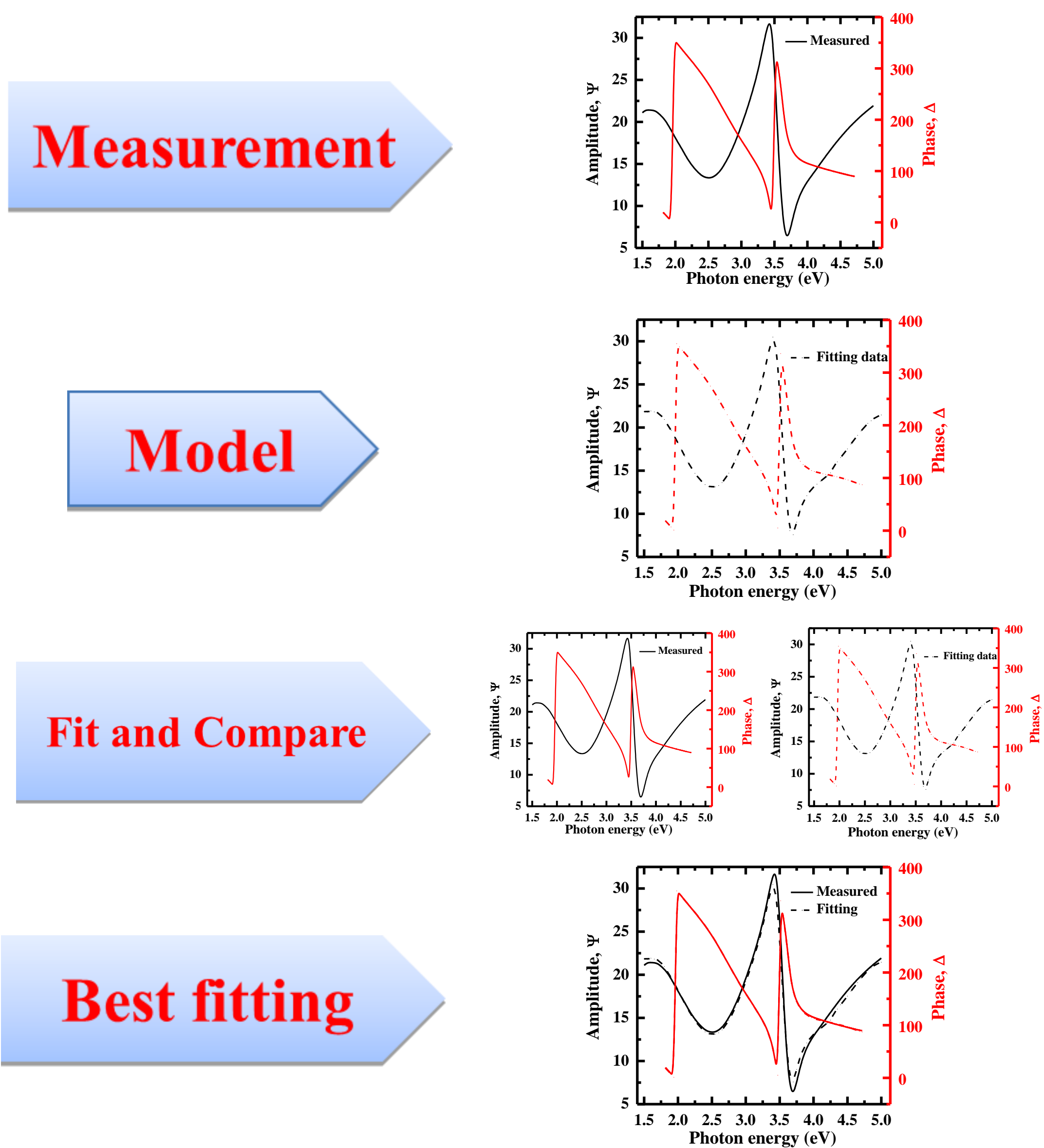

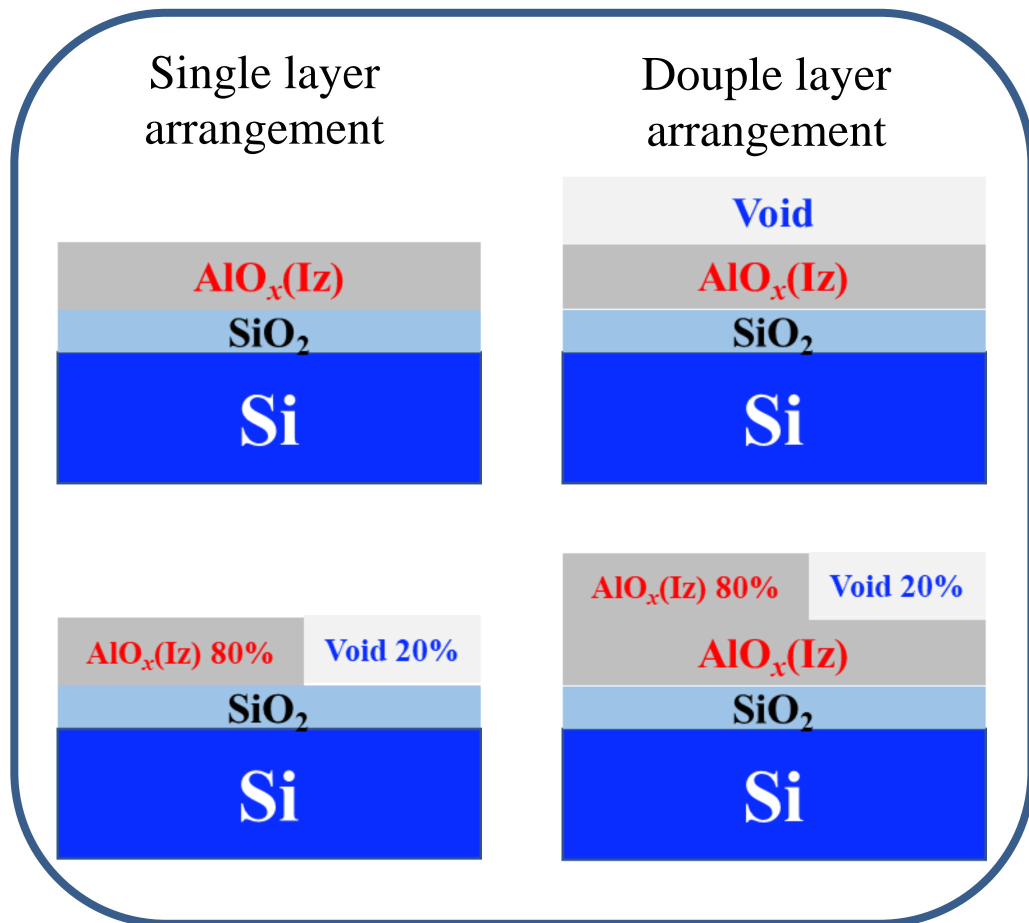

Figure 2. 13. (a) Basic procedure used in ellipsometry measurements to determine optical constant and layer thickness from experimental spectra. (b) Two-layer model used for the spectra analysis.

2.3.3 Morphological study by Atomic Force Microscope (AFM)

The surface smoothness was tested by Atomic Force Microscope (AFM) (AFM5000II, Hitachi-Tech Science). A schematic representation of AFM is shown in **Figure 2.14.** Atomic force microscopy (AFM) is a technology used for characterizing materials, for example, surface topography and surface roughness by sensing the force between a sample and a probing tip. AFM typically uses a silicon or silicon nitride cantilever which has a downward-facing sharp tip at the end with a few nanometer radiuses.

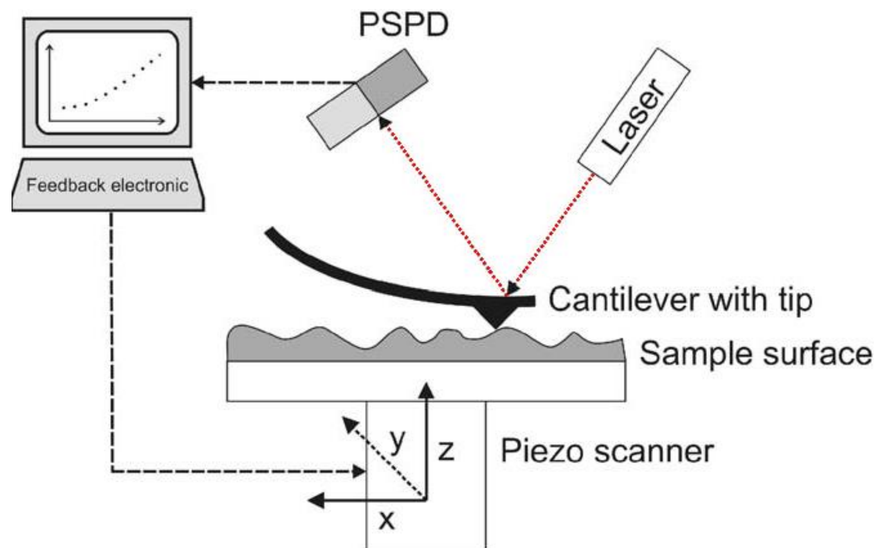

Figure 2. 14. Schematic diagram of AFM.

The basic measuring principle of the AFM is to press the cantilever on the sample. As the tip is close to the surface, the van der Waals force between the tip and the sample surface is increased. The force curve depends on the distance between the tip and the sample, as shown in **Figure 2.15**. There are two kinds of contact modes (contact and non-contact). In the contact mode, the repulsive force is used because the cantilever is closed less than a few angstroms to the sample surface (bold black line on the left side of **Figure 2.15**). The noncontact mode is used the attractive force which is generated by long-range van der Waals interactions. In this mode, the cantilever maintains the space of ten to hundred Å from the sample surface.

The cantilever moves back and forward on the surface to scan. The force on the cantilever varies depending on the surface height profile. A small integrated circuit with a piezo-electric crystal maintains a constant height difference (hence, a constant force). A laser is induced to the back of the cantilever and the sensitive photodetector checks the position changing of the reflected laser. Piezoelectric ceramics are used to move either the sample or the tip with high precision in 3D. The scanning is done in a feedback loop when moving during the scan the bending of the cantilever remains constant in order to maintain constant force. Then the up-and-down motion is recorded as the sample topography.

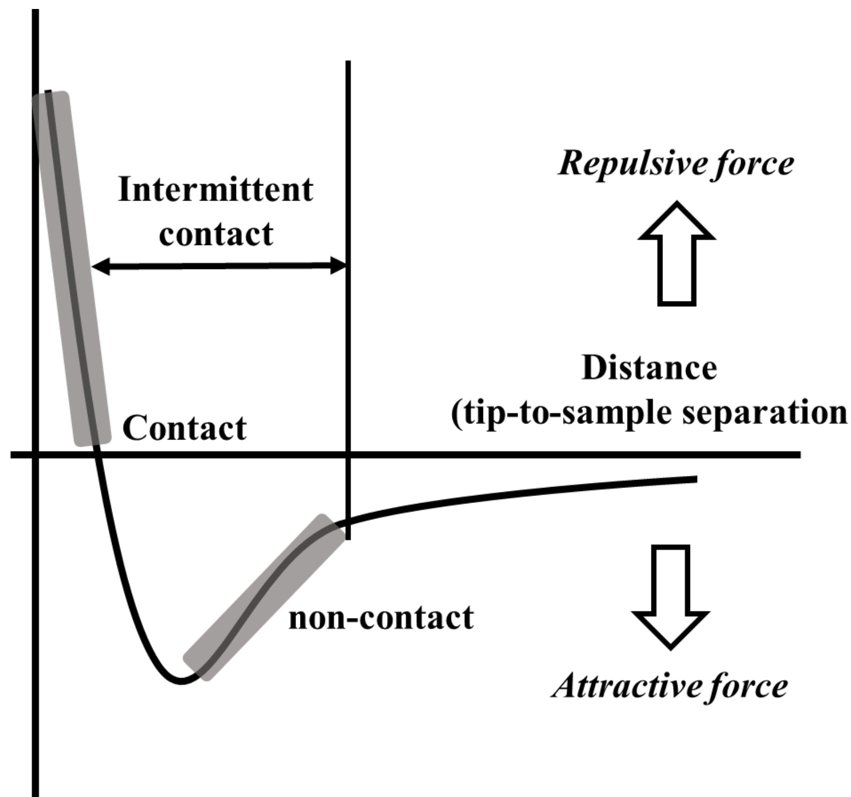

Figure 2. 15. Force curve of AFM.

2.3.4 Minority carrier lifetime utilize by Micro-photoconductive decay (μ-PCD)

The minority carrier lifetime and corresponding to recombination velocity were determined by using Micro-photoconductive decay (μ-PCD) system. In this system, the carrier lifetime was extracted from the measurement of photoconductance decay with microwave reflectance in a linear range. As illustrated in **Figure 2.16**, two light beams are used where a steady-state light beam with pre-calibrated steady-state illumination intensities up to 2 suns is used for scanning rate, G. This beam determines the steady-state injection level that is defined as the concentration of photogenerated excess minority carriers, Δn.

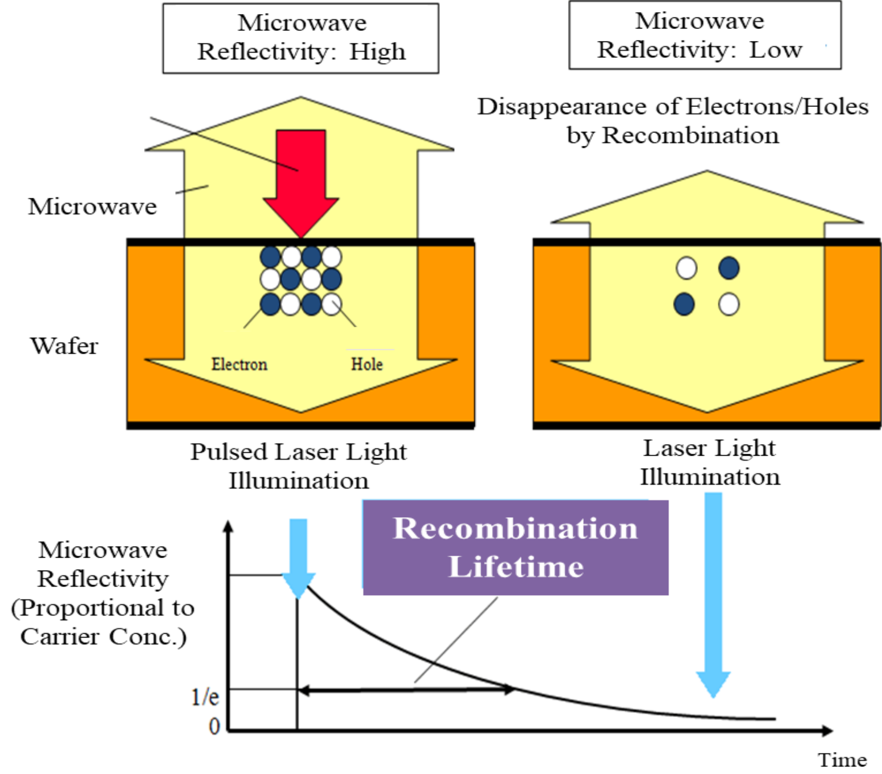

Figure 2. 16. Principle of micro-photoconductive decay (μ-PCD) system.

The second beam is a short duration (0.2μs) the laser pulse with a 905nm wavelength. This pulse generates excess carriers, $\delta\eta_{laser}(t)$. The sequence of steps in the μ-PCD scanning measurement is illustrated in Fig. 2.16. For each step, the decay time constant, τ_{eff}, is determined directly from exponential fitting to the measured decay curve. Pre-calibrated steady-state beam intensity, I, in suns is converted to the corresponding effective generation rate G, using the wafer thickness and standard quasi-steady-state procedure.[2.17] There is user input for the optical constant in the μ-PCD measurement recipe that takes into account reflectivity differences between samples in the determination of G. The quasi-steady-state photoconductance QSSPC procedure. measuring lifetime as $\Delta n = G\tau_{eff}$.

The recombination velocity was calculated from eq. 2.21

$$\frac{1}{\tau_{eff}} = \frac{1}{\tau_{bulk}} + \left[\frac{W}{2Seff} + \frac{1}{D_n}\left(\frac{W}{\pi}\right)^2\right]^{-1} \quad (2.21)$$

where W is the oxide thickness, D_n is the diffusion coefficient, S_{eff} is the recombination velocity, τ_{eff} is the minority carrier lifetime of thin-film, and τ_{bulk} is the minority carrier lifetime for the substrate.

2.3.5 Surface observation by Optical microscope

The attachment of mechanically exfoliated $MoSe_2$ flakes was confirmed by an optical microscope. The confirmation of the photolithography process following electrode connection by sputtering was also utilized by an optical microscope. The device structure of $MoSe_2$ based MIS-FET was also confirmed by using an optical microscope.

The function to create a magnified image of a specimen consists of three basic functions of "obtaining a clear, sharp image", "changing a magnification", and "bringing into focus". An optical system for implementing these functions is referred to as an observation optical system.

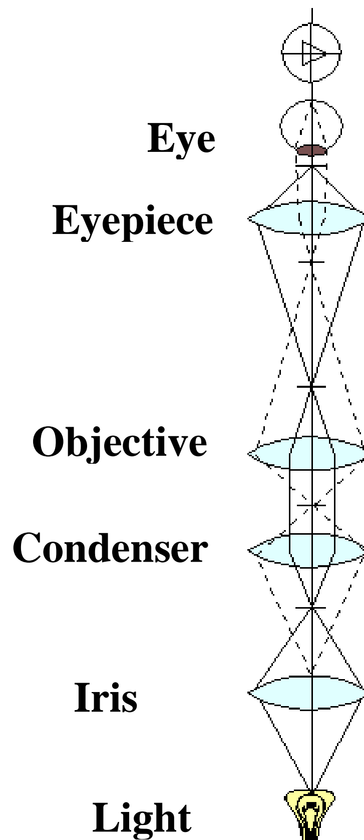

Figure 2. 17. Schematic of a compound microscope.

Meanwhile, the function to illuminate a specimen consists of three basic functions of "supplying light", "collecting light", and "changing light intensity". An optical system for implementing these functions is referred to as an illumination optical system. The structure of a compound microscope is illustrated in **Figure 2.17**. The major parts of a compound microscope include the eyepiece, objective, and stage for both reflective and transmitted light microscopes. The transmitted light microscope also needs to consider illumination which aids in seeing the object clear. Eyepieces are used for magnification. Microscopes either are monocular, meaning that it has only one eyepiece, binocular (two eyepieces) or trinocular (two for eyes, and one for camera). Sometimes a binocular reflected light microscope is referred to it as stereoscopic which only means that you are using two oculars to see depth. The eyepieces are usually marked with a number. Objectives provide the resolution power of the microscope, which increases the detail. A reflecting light microscope (dissecting microscope) has a lower resolving power than a transmitted light microscope. However, a reflecting microscope has a better depth of field and ideal for dissecting or looking at larger objects that cannot be made into a slide. In transmitting light microscopes, the illumination system is very important. The system includes the light source, condenser, and iris. A condenser is usually a combination of lenses that gathers and concentrates light in a specified direction, under the stage. The iris controls the intensity of the light that goes into the condenser. The light source is a variety of bulbs that create just the right kind of light with little heat.

2.3.6 Elemental Composition and chemical bonding analysis by X-ray photoelectron spectroscopy (XPS)

Photoelectron spectroscopy is the technique detecting a photo-ionization and analysis of the kinetic energy of the emitted photoelectrons to investigate the composition and electronic state near the surface region. As shown in Figure 2.18, the photon radiated by monochromatic source normally used X-Ray is absorbed in material then, ionization and the emission of a core (inner shell) electron are occurred with following equation (eq.2.22):

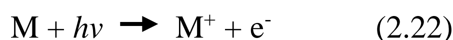

$$M + h\nu \rightarrow M^{+} + e^{-} \qquad (2.22)$$

Where h is the Planck constant, ν is the frequency, M (atom), and e is the electron.

From the conservation of energy rule, the equation is changed following (eq. 2.23);

$$E(M) + h\nu = E(M^{+}) + E(e^{-}) \qquad (2.23)$$

The eq.2.23 can be changed to eq.2.24 because the electron's energy can be present by kinetic energy (K.E).

$$KE = h\nu - [E(M^{+}) - E(M)] = h\nu - BE \qquad (2.24)$$

The indicated brackets in eq.2.6 represent the energy difference between the ionized and neutral atoms so-called the binding energy (BE) of the electron. For every element, there is specific binding energy due to each core atomic orbital. This means that any detected electrons provide a specific fingerprint of the atomic species.[2.18]

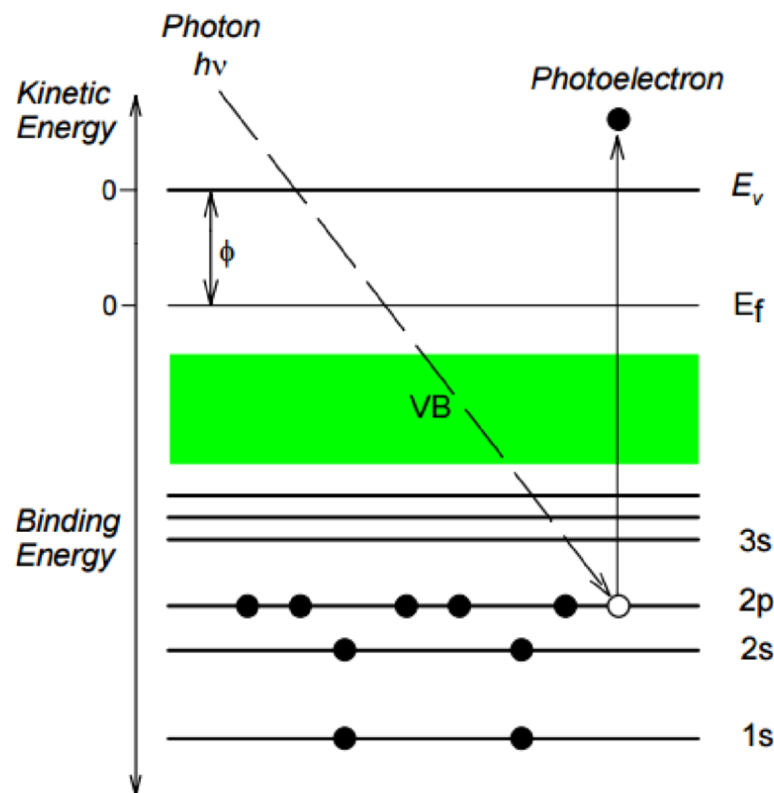

Figure 2. 18. Schematic for the generation of energy difference by photoemission.

2.3.7 Crystallographic structure by X-ray diffraction

Many materials are crystalline which has a repeated structure. These crystals are composed of unit cells in which the smallest number of atoms is contained. The dimension size of its unit cells is a lattice parameter. The most famous method to

determine the lattice constant of a crystalline is X-ray diffraction (XRD) using Bragg's law (eq.2.25). When two parallel waves were reflected by atoms on two parallel lattice planes, the wave which goes to the second lattice plane will travel an extra distance (l) in **Figure 2.19.** This diffracted wave has more travel distance ($2l$) than diffracted from the first lattice plane. The distance $2l$ and diffracted angle (θ) depend on the distance of the two planes (d) in **Figure 2.19** and its relationship is indicated by the function of l=d sin(θ). If the $2l$ is equal to a wavelength (λ) or integer multiples of λ (i.e., nλ), the reflected waves will have the same phase. Hence, the intensity of amplitude is to be maxima when the phase shift is exactly equal to nλ. This process is comprised of equation 2.25 which is the so-called Bragg's law equation.

$$d = n\lambda / 2\sin(\theta) \qquad (2.25)$$

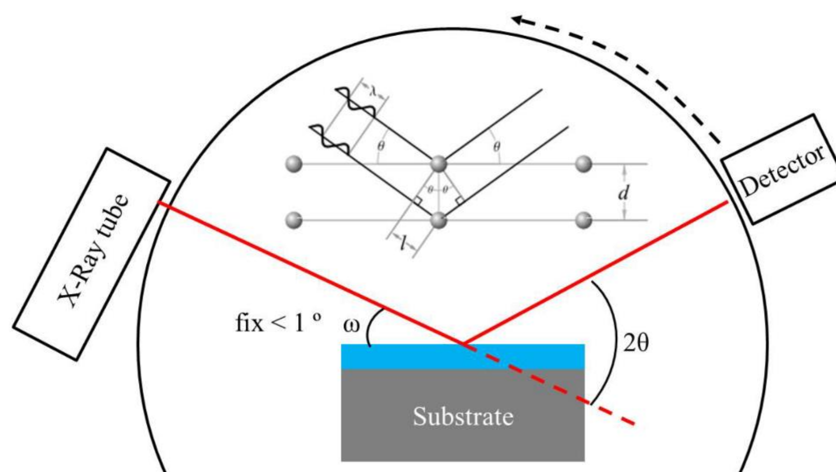

Figure 2. 19. Schematic of XRD.

2.3.8 Size distribution of mist precursors by the particle counter

The size distribution of mist droplets was monitored by fast scanning mobility particle sizer (FMPS). This measurement system was carried out to understand the film properties through size distribution. The basic four components of particle counter are shown in **Figure 2.20 (a)** where Impactor is used for mist droplets conditioner, to neutralize the charge mist particles a neutralizer is employed, differential mobility analyzer is commonly used for size selector, and condensation particle counter (CPC)

is carried out to count the mist droplets. A Fast-Scanning Mobility Particle Analyzer of model-3091 is shown in **Figure 2.20 (b).**

(a)

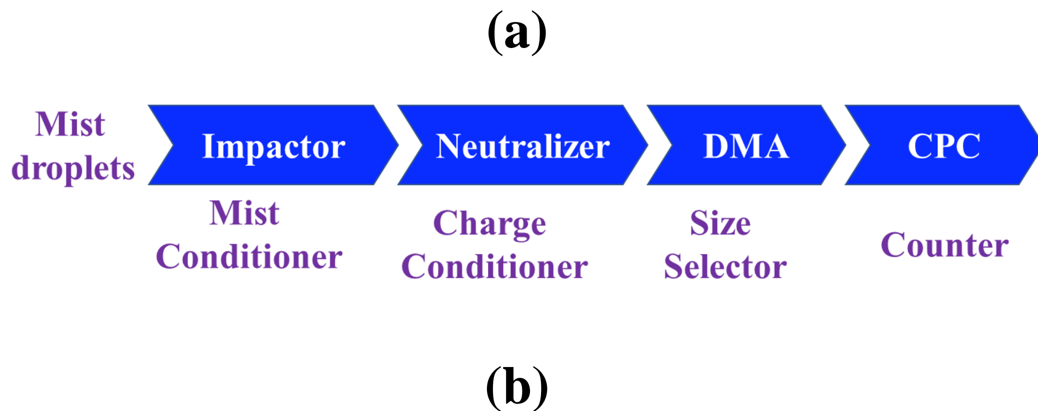

(b)

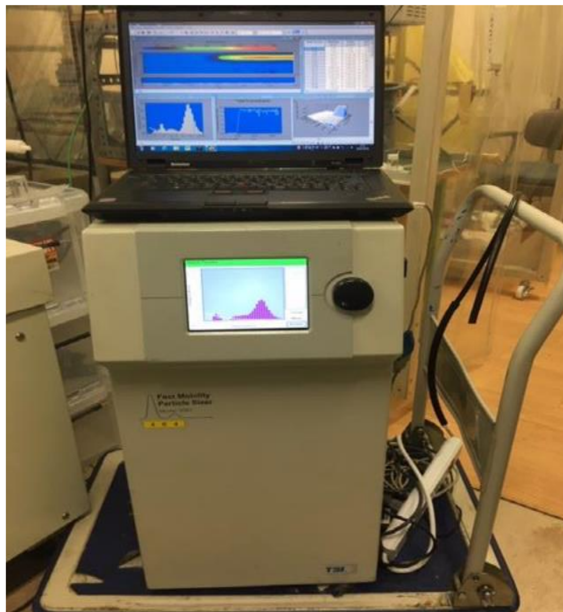

Figure 2. 20. The function of a particle counter. (b) Picture of Fast Scanning Mobility Particle Analyzer, Model-3091.

Impactors are devices that separate particles based on inertia and in general operate to remove particles of a given size range from the sample flow, either collecting them for later analysis or removing them to avoid problems of instrument contamination, etc. The basic principle of an impactor is illustrated in **Figure 2.21**. Essentially air containing particles are accelerated through an orifice or nozzle towards a plate some distance below the orifice, which causes the airstream to change direction abruptly. Particles that are small enough to follow the streamlines remain suspended, while those that cannot hit or impact on the plate. The cut-off point of an impactor is the size at

which particles are collected with 50% efficiency. Collection efficiency increases for particles larger than the cut-off and decreases for smaller particles. The cut-off diameter for a round jet impactor is dependent on the orifice diameter and flow rate according to the following equation (Baron and Willeke):[2.19]

$$d_{50} = \sqrt{\frac{9\eta\pi W^3}{4p_P C_c Q}}\sqrt{Stk_{50}} \qquad (2.28)$$

Where Stk_{50} is the stokes number is expressed as $Stk_{50} \approx 0.24$,[2.14] η is the air viscosity, W is the nozzle diameter, Cc the Cunningham slip factor, p_P the particle density, and U is the average flow velocity in the nozzle.

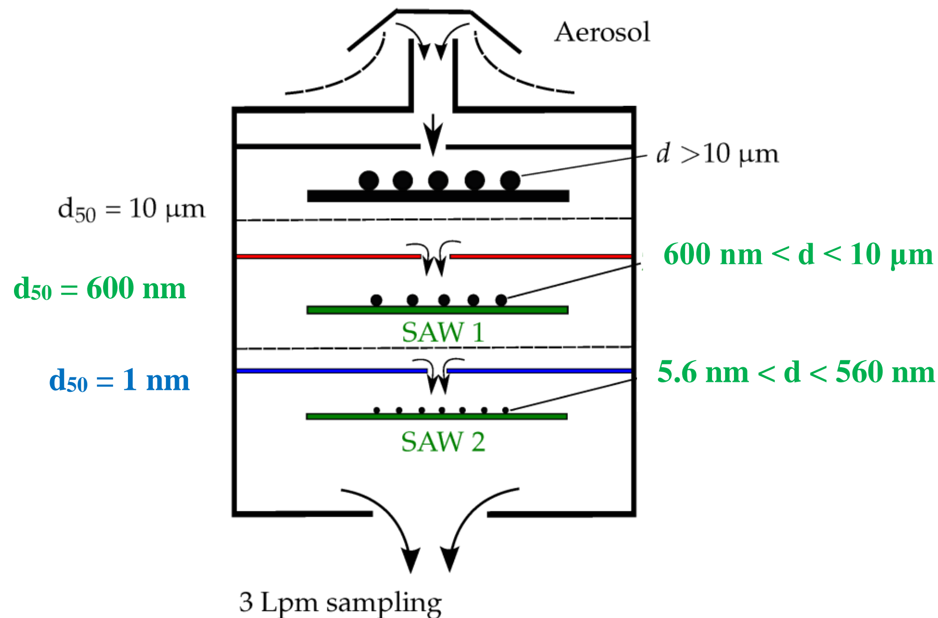

Figure 2. 21. Schematic of a cascade impactor.[2.19]

The aerosol might have charged particles. The second part of the particle counter is the neutralizer. The neutralizer is carried out to neutralize the charged particle so that they can’t radiate energy in the next sections.

The schematic of the differential mobility analyzer is shown in Figure **2.22**. By setting different voltages in the DMA, particles of different electrical mobility are selected and their particle number concentration can be measured. The DMA consists of two electrodes with the inner electrode at a negative voltage, while the outer

electrode is electrically grounded. This creates an electric field between the two electrodes. Before entering the DMA, the sample particles are charged by passing through the charger, where positive and negative ions are produced. The charged aerosols are introduced through an annular slit closed to the outer electrode into the top of the DMA and then, merged with the particle-free airflow. The flow of both streams is maintained in the laminar regime to prevent the mixing of those streams. In the DMA, charged particles are separated according to their electrical mobility. The electrical particle mobility is a function of the particle charge, particle diameter, dimensions of the DMA, and flow rate. The sample flow carrying particles with the same small range of electrical mobility is drawn through the small slit located at the bottom of the collector rod. The remaining air is exhausted out as excess airflow. The particle number concentration in the sample flow is measured in a particle counter.

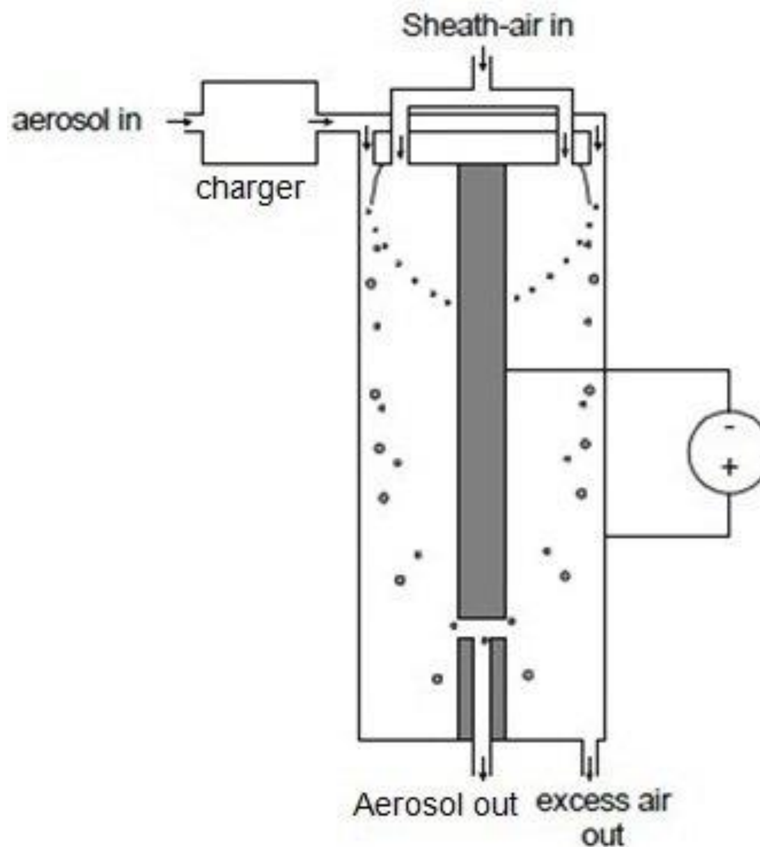

Figure 2. 22. Schematic illustration of differential mobility analyzer.[2.20]

The first known CPC was reported by Aitken in 1888. All commercial CPCs up to 1975 used the adiabatic expansion of constant volume samples to produce condensation, resulting in a discontinuous, pulsating aerosol flow. The first commercial

continuous flow CPC was reported in 1980 and still represents the most common type in the automotive field.[2.21] In this type of CPC, particle growth is achieved by passing the aerosol through a saturated vapor of the working fluid, typically n-butanol, followed by cooling in a condenser, as illustrated in Fig. 2.23.[2.22] The temperatures of the saturator condenser and properties of the working fluid determine the lower detectable size, which is typically in the range of 3–10 nm. The CPCs in the European legislation must be full-flow (the total inlet flow must pass the counting optics) and have a 50% counting efficiency at 23 nm.[2.23-24] Recently, water-based CPCs have been introduced,[2.20] but are not used in the automotive field due to the hydrophobic nature of soon after passing through the Volatile Particle Remover.

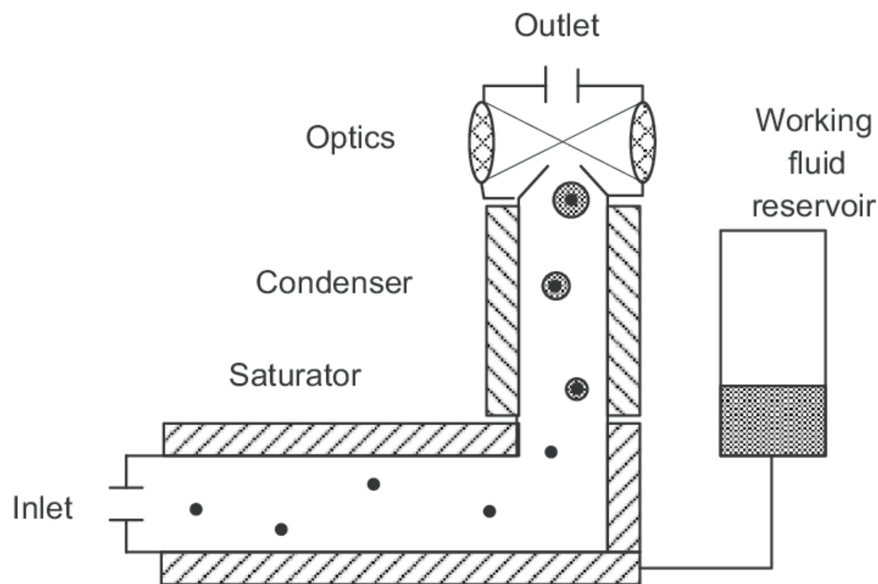

Figure 2. 23. Schematics of continuous flow condensation particle counter (CPC).[2.25]

2.3.9 Van der Pauw method for Hall measurement

The Van-der-Pauw method is a technique to determine the electrical transport properties of materials either bilk or thin films, like the electrical conductivity, the resistivity, the hall constant, the charge carrier concentration, carrier mobility, and the semiconductor type. In 1958 van der Pauw solved the general problem of potential distribution in a thin, conductive layer of any shape and thus made it possible to carry out Hall and resistance measurements on them. Therefore, in theory, it is possible to handle a sample of any shape. However, in actual measurement, if the measured voltages are too imbalanced, error are surely to occur. A well-proportioned shape is

desirable where the thickness t of the sample must be homogeneous and small in relation to the distance between contacts. **Figure 2.24.** shows the plate-shaped test with small electrodes attached to the four corners of a uniform and flat film.

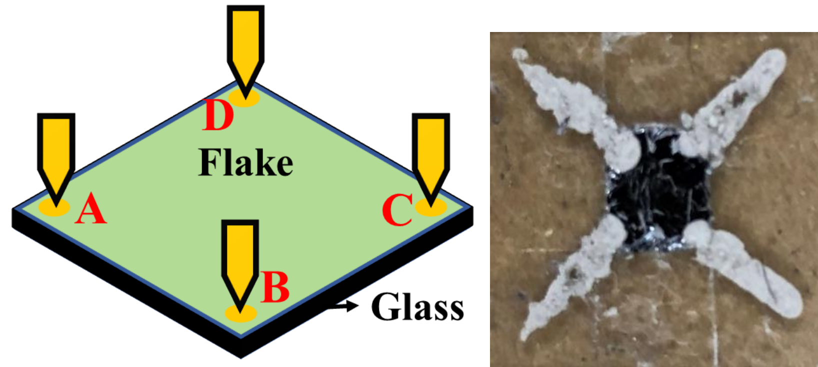

Figure 2. 24. Experimental setup for Van-der-Pauw measurement.

Place each electrode counterclockwise from the upper left corner A, let B, C, and D. First, without applying a magnetic field, a current I_{AB} is passed between the electrodes AB, and then measure the voltage V_{CD} between the electrode's CDs. At this time, use the resistors $R_{AB,CD}$ and define as follows

$$R_{(AB,CD)} = \frac{V_C - V_D}{I_{AB}} \quad (2.29)$$

Next, a current IBC is passed between the electrodes BC, and the voltage VDA between the electrodes DA is measured. Then resistance $R_{BC,DA}$ will be:

$$R_{(BC,DA)} = \frac{V_D - V_A}{I_{BC}} \quad (2.30)$$

After that, a current IAC is passed between the electrodes AC, and a magnetic field with a magnetic flux density B is applied perpendicular to the sample surface (**Figure 2.25**). At this time, if the voltage generated between the electrodes BD is V_{BD} and $R_{AC,BD} = V_{BD}/I_{AC}$, the resistivity ρ, the carrier density n, and carrier mobility µ are given as follows.

$$\rho = \frac{\pi d}{\ln 2}\frac{(R_{AB,CD}+R_{BC,DA})}{2} f\left(\frac{R_{AB,CD}}{R_{BC,DA}}\right) \quad (2.31)$$

$$n = \frac{B}{e.2d.\Delta R_{AC,BD}} \quad (2.32)$$

$$\mu = \frac{d}{B}.\frac{\Delta R_{AC,BD}}{\rho} \quad (2.33)$$

Where e is the charge of the electron and d is the thickness of the epitaxial layer. F is a coefficient for correcting non-uniformity caused by the shape of the sample, position of the electrodes, etc.

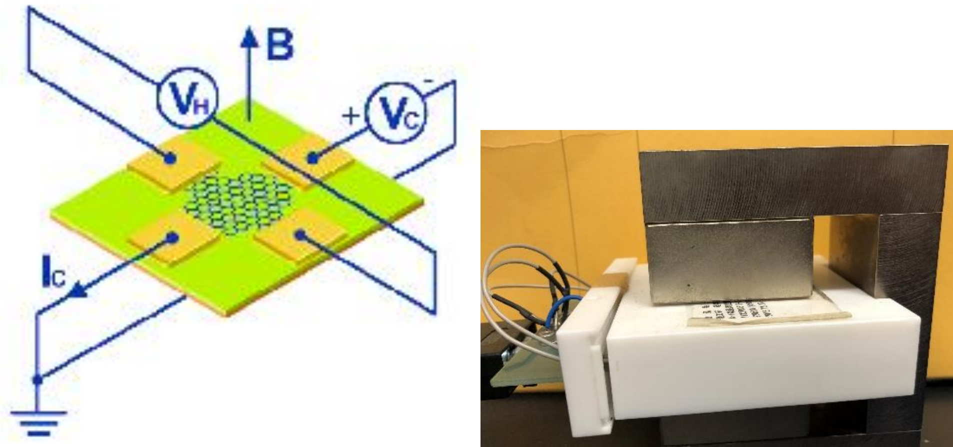

Figure 2. 25. Sample configuration for the Hall coefficient measurement using Van-der-Pauw method, with an applied magnetic field perpendicular to the sample surface.

In this study, the surface of the synthesized single crystal was cleaved with scotch tape to make it as uniform as possible. After that, it was cut out into a square to prepare the sample for measurement. Place this sample on a glass substrate. After sticking, silver paste was used to the four ends of the sample to form electrodes (shown in **Figure 2.24**). The measurement was performed at room temperature, and the magnetic field was -0.5T.

2.3.10 Junction properties analysis by C-V measurement

C-V measurements are carried out to understand the junction properties of oxide and c-Si interface by utilizing the interface defect density, negative fixed charge density, border trap density, flat band voltage, threshold voltage, built-in potential, dielectric constant, etc. of MOS capacitor. **Figure 2.26** illustrates the construction of a MOS capacitor. In a MOS structure, an oxide is placed between a semiconductor and a metal gate where the semiconductor and metal gate are the two plates of the capacitor. The area of the metal gate is defined as the area of the capacitor. The equivalent circuit of the MOS capacitor is illustrated on the right side of **Figure 2.26**.

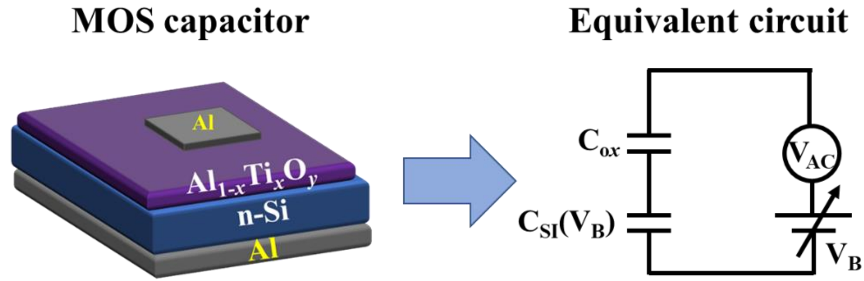

Figure 2. 26. MOS capacitor structure with its equivalent circuit.

The energy band diagrams of the three components when separate, are shown in **Figure 2.27. Figure 2.27(c)** shows the band diagram of n-type silicon with the free electron level at some energy above the conduction band. The free-electron level is defined as the energy level above which the electron is free. For silicon, the free electron level is 4.05 eV above the conduction band edge, as shown in **Figure 2.27(c)**. **Figure 2.25(b)** shows the band diagram of aluminum oxide – an insulator with a large energy gap in the range of 8-9 eV. The free energy level in AlO_x is 0.70 eV above its conduction band. Work function is defined as the energy difference between the free electron level and Fermi level. For the n-type silicon shown in **Figure 2.27(c)**, the work function, $q\phi_s$, can be expressed as:

$$q\phi_s = qX + \frac{E_g}{2} + q\Psi_B \qquad (2.34)$$

Where Ψ_B is the difference between the Fermi potential and the intrinsic potential.

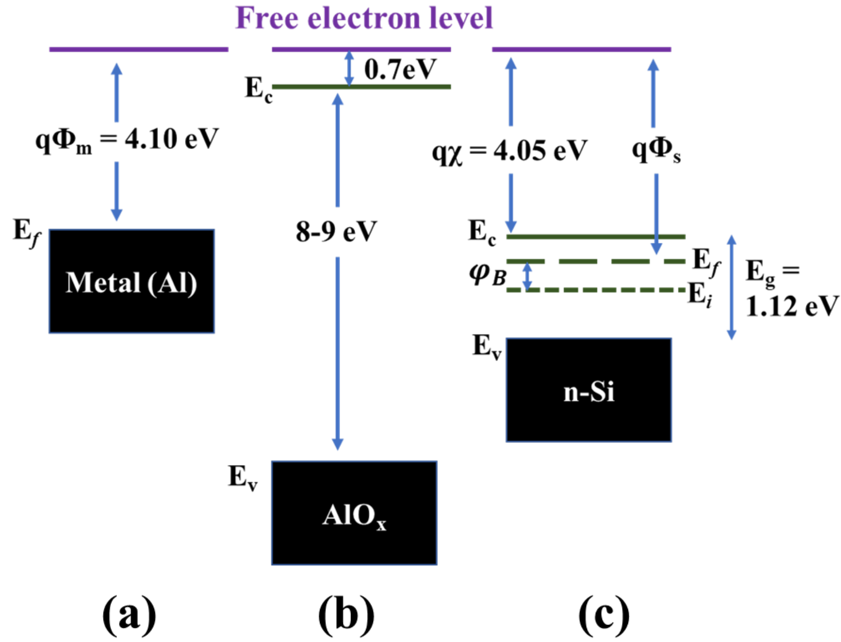

Figure 2. 27. Energy-band diagram of the three components of a MOS capacitor; (a) metal (aluminum), (b) Aluminum oxide, and (c) n-type silicon.

By definition, capacitance is the change of charge corresponding to the change of voltage and expressed as;

$$C = \frac{\Delta Q}{\Delta V} \qquad (2.35)$$

One general way to implement is to apply a small AC voltage signal (millivolt range) to the under test and measure the resulting current. Integrate the current overtime to derive Q and finally calculate C. In C-V measurement is utilized by using two simultaneous voltage sources: an applied AC voltage signal and a DC voltage that is swept in time, as illustrated in **Figure 2.28(a). Figure 2.28(b)** illustrates a high-frequency C-V curve for an n-type semiconductor substrate. As a DC sweep voltage is applied to the gate, it causes the device to pass through accumulation, depletion, and inversion regions.

(a)

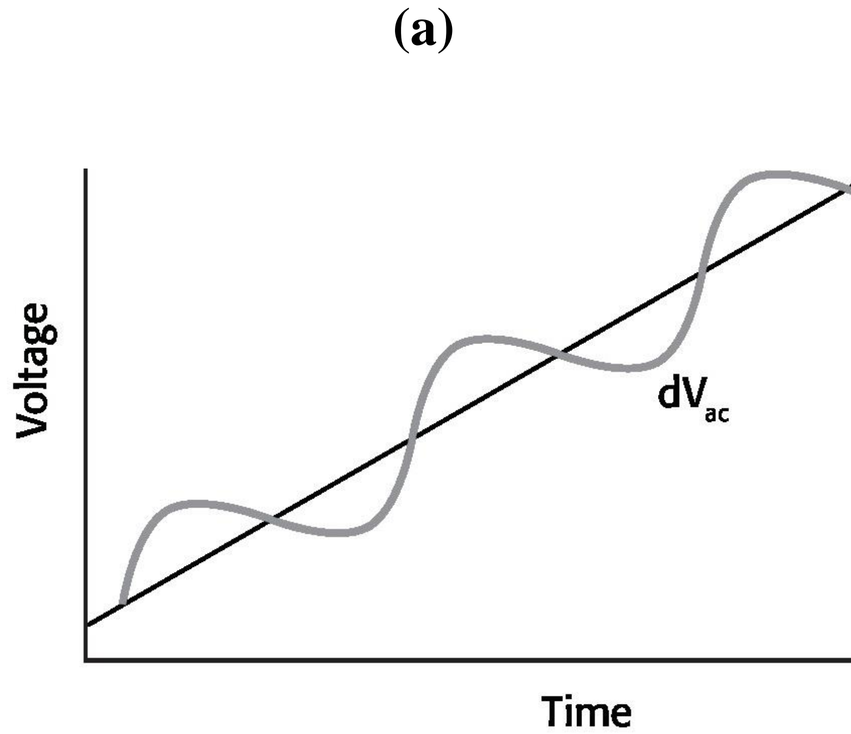

(b)

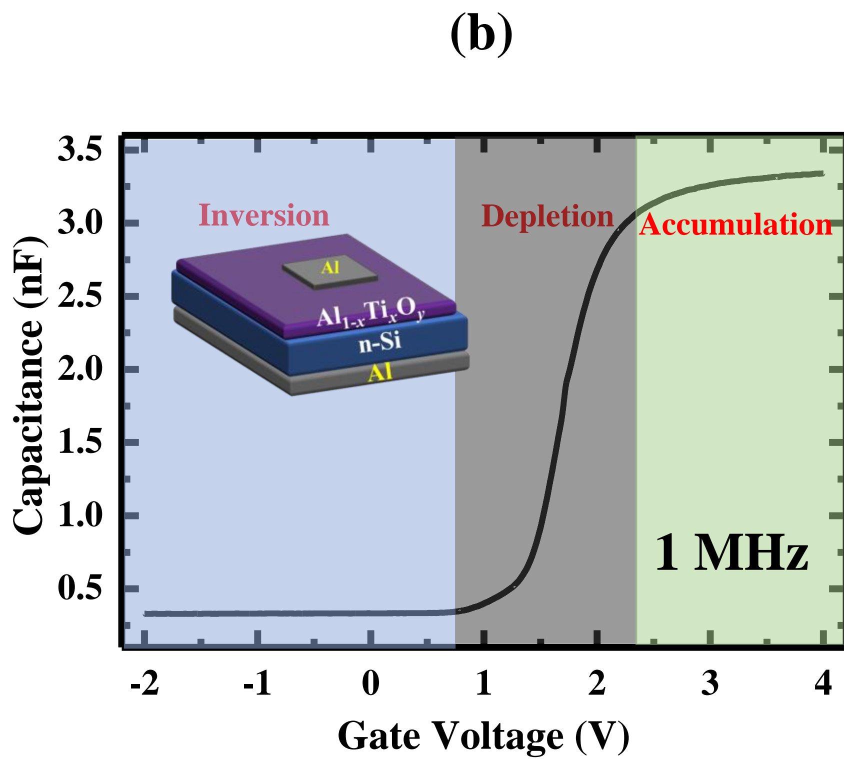

Figure 2. 28. (a) AC and DC voltage of C-V sweep measurement. (b) Capacitance-voltage diagram of an Al/AlO$_x$/n-Si/Al MOS capacitor with the frequency of 1 MHz.

a) At Vg = 0, Flat band condition

For simplicity, the flat band voltage is taken to be zero for all cases. **Figure 2.29** shows the energy band diagram of a MOS system under the flat band condition in which there is no field in all three materials. If the metalwork function is less than the silicon work function (n-Si), a negative gate voltage is required to obtain a flat-band condition. The flat band voltage can be extracted from the eq. 2.36.

$$V_{fb} = (\phi_m - \phi_s) - \frac{Q_{ox}}{C_{ox}} \qquad (2.36)$$

Where Q_{ox} is the equivalent oxide charge per unit area at the oxide-silicon interface, and C_{ox} is the oxide capacitance per unit area.

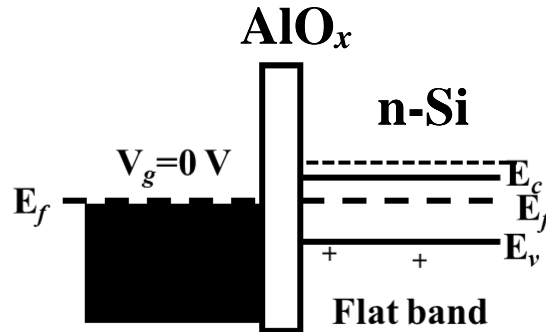

Figure 2. 29. Energy band diagram for flat band condition.

b) Accumulation Region

When a positive voltage is applied to the gate of an n-type MOS capacitor, as shown in **Figure 2.30.** This falls the metal Fermi level corresponding to the silicon Fermi level and creates an electric field in the oxide that would accelerate the positive charge toward the metal electrode. A field is also induced at the silicon surface in the same direction as the oxide field. Because of the low carrier concentration in silicon compared with the metal, the bands bend downward toward the oxide interface. The Fermi level stays flat within the silicon since there is no net flow of conduction current. Due to the band bending, the conduction band at the surface is much closer to the Fermi level than is the conduction band in the bulk silicon. This results in an electron concentration much higher at the surface than the equilibrium electron concentration in the bulk. Since access electrons are accumulated at the surface, this is referred to as the accumulation condition. An equal amount of positive charge appears on the metal side of the MOS capacitor, as required for charge neutrality. For an n-type MOS capacitor, the oxide

capacitance is measured in the strong accumulation region. This is where the voltage is positive enough that the capacitance is essentially constant and the C-V curve is almost flat (**Figure 2.28(b)**).

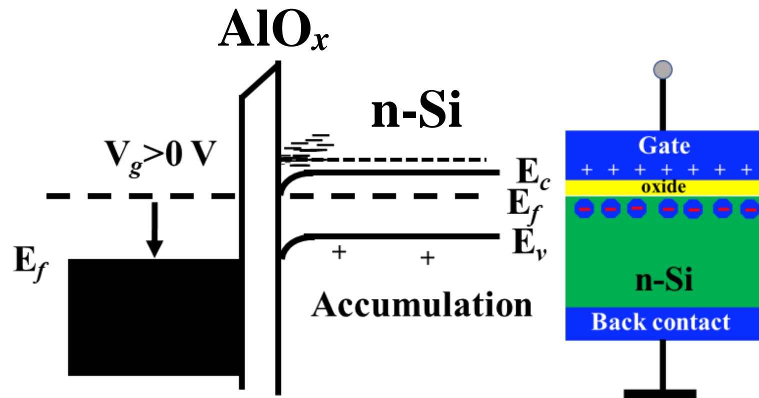

Figure 2. 30. Energy band diagram for accumulation condition with their schematic.

c) Depletion Region

When a negative voltage is applied to the gate of an n-type MOS capacitor, the Fermi level moves upward, which creates an oxide field toward the silicon substrate due to the acceleration of the positive charge in the same direction. A similar field is induced in the silicon, which causes the bands to bend upward toward the surface, as shown in **Figure 2.31**. Since the conduction band at the surface is now further away from the Fermi level than is the conduction band in the bulk, the electron concentration at the surface is lower than the concentration in the bulk. This is referred to as the depletion condition. The depletion of electrons at the surface leaves the region with a net positive charge arising from the unbalanced acceptor ions. An equal amount of positive charge appears on the metal side of the capacitor. This area of the semiconductor acts as a dielectric because it can no longer contain or conduct charge. The total measured capacitance now becomes the oxide capacitance and the depletion layer capacitance in series, and as a result, the measured capacitance decreases. This decrease in capacitance is illustrated in **Figure 2.28** in the depletion region. As a gate voltage increases, the depletion region moves away from the gate, increasing the effective thickness of the dielectric between the gate and the substrate, thereby reducing the capacitance.

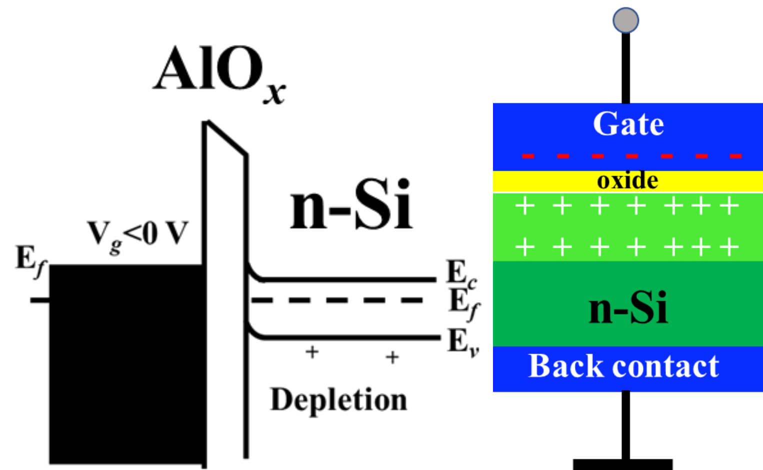

Figure 2. 31. Energy band diagram for depletion condition with their schematic.

d) Inversion Region

As the negative voltage increases, the band bending also increases, resulting in a wider depletion region and a more (positive) depletion charge. This goes on until the band bends upward so much that at the surface, the valence band is closer to the Fermi level than the conduction band is, as shown in **Figure 2.32**. When this happens, not only are the electrons depleted from the surface, but the surface potential is such that it is energetically favorable for holes to populate the valence band. In other words, the surface behaves like p-type material. Note that this p-type surface is formed not by doping, but instead by inverting the original n-type substrate with an applied electric field. This condition is called inversion. The positive charge in the silicon consists of both the ionized donors and the thermally generated holes in the valence band. Again, it is balanced by an equal amount of negative charge on the metal gate. The surface is inverted as soon as the intrinsic level of silicon crosses the Fermi level. This is called weak inversion because the hole concentration remains small until E_i is considerably below E_f. If the gate voltage is increased further, the concentration of holes at the surface will be equal to, and then exceed, the electron concentration in the substrate. This condition is called strong inversion. Once the depletion region reaches a maximum depth, the capacitance that is measured by the high-frequency capacitance meter is the oxide capacitance in series with the maximum depletion capacitance. This capacitance is often referred to as minimum capacitance. The C-V curve slope is almost flat (**Figure 2.28**).

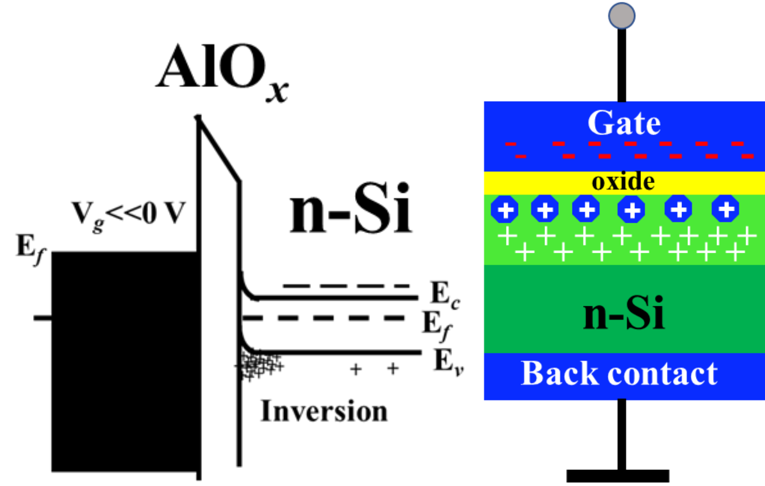

Figure 2. 32. Energy band diagram for inversion condition with their schematic.

2.3.10 Carrier transport parameters of MIS-FET

In the basic MIS-FET operation, three different regions are considered named cut-off region, linear region, saturation region. Usually, the regions below the threshold voltage are called cut-off regions. The magnitude of current flowing through MOS in cut-off conditions is negligibly small as the channel is not present.

Consider an MIS-FET?, as gate voltage exceeds the threshold voltage, the channel is formed between source and drain terminals. If there is a voltage difference between source to drain, the current will flow. The magnitude of the current increases with the increase of drain to source voltage, this region is called the linear region, and the corresponding mobility is assigned as linear mobility.

$$\mu_{lin} = (dI_{DS}/dV_G) \times (L/(W \cdot C_i \cdot V_D)) \qquad (2.37)$$

Further, drain to source voltage increases beyond the linear condition, increasing voltage seems to have no effect on the drain to source current. When the MOS operate in this region, it is said to be in saturation and the mobility corresponding to this regime is called saturation mobility and expressed as,

$$\mu_{sat} = (d\sqrt{I_{DS}}/dV_G)^2 \times (2L/W \cdot C_i) \qquad (2.38)$$

where L is a channel length, W is channel width, and C_i is the capacitance between the $MoSe_2$ channel and back gate, and V_D is the voltage drop through the channel.

The threshold voltage (V_{th}) has been extracted from a plot of the square root of I_D versus Vg. In particular, V_{th} can be estimated from the intersection of the tangent of the linear part of the plot of the square root of I_D with the axis of gate voltages (**Figure 2.33**). Under vacuum conditions, the determined value of threshold voltage for $MoSe_2$ based MIS-FET where AlO_x is used as the dielectric layer was 2.75 V.

Generally, the variation of threshold voltage in MIS-FETs is directly related to the trapped charge density in the insulator/organic semiconductor interface.2.14 The trapped charge density at the interface can be determined by the following relation:2.15

$$N_{trap.charge} = \frac{\Delta V_{th} C_i}{q} \qquad (2.39)$$

Where Ci is the insulator capacitance per unit area, ΔVth the measured shift in the threshold voltage, and q is the electronic charge.

The subthreshold swing, related to the sharpness between the off and on stat, can be determined by the following relation:2.16

$$SS = [\frac{dlog(I_D)}{dV_g}]^{-1} \qquad (2.40)$$

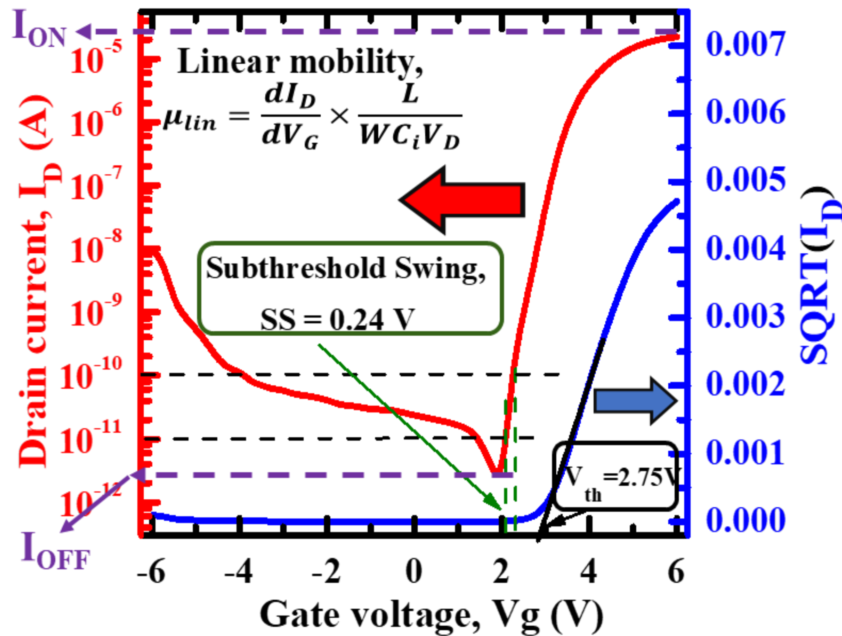

Figure 2. 33. Transfer characteristics of MIS-FET to evaluate the key parameters.

References

2.1. Shanmugasundaram, K. "*A study of the mist deposition and patterning of liquid precursors thin films*", The Pennsylvania State University (2008).

2.2. Hossain, J.; Ohki, T.; Ichikawa, K.; Fujiyama, K.; Ueno, K.; Fujii, Y.; Hanajiri, T.; and Shirai, H. "Investigating the chemical mist deposition technique for poly(3,4-ethylenedioxythiophene):poly(styrene sulfonate) on textured crystalline-silicon for organic/crystalline-silicon heterojunction solar cells", *Jpn. J. Appl. Phys.* **55**, 0310601, (2016).

2.3. Ohki, T.; Ichikawa, K.; Hossain, J.; Fujii, Y.; Hanajiri, T.; Ishikawa, R.; Ueno, K.; and hirai, H. "Effect of substrate bias on mist deposition of conjugated polymer on textured crystalline ‐ Si for efficient c ‐ Si/organic heterojunction solar cells", *Physica Status Solidi A* **213(7)**, 1922-1925, (2016).

2.4. Islam, A.T.M. S.; Karim, M. E.; Rajib, A.; Nasuno, Y.; Ukai, T.; Kurosu, S.; Tokuda, M.; Fujii, Y.; Nakajima, Y.; Hanajiri, T.; Shirai, H. "Chemical mist deposition of organic for efficient front- and back- PEDOT:PSS/crystalline Si heterojunction solar cells", *Applied Physics Letters*, **2019,** 114, 193901.

2.5. Rayleigh, L. "Instability of Jets", *Proc. London math. Soc.* **10**, 4, (1879).

2.6. Wood, W. R., and Loomis, A. L. "The Physical and Biological Effects of High-Frequency Sound-Waves of Great Intensity", *Philosophical Magazine* **4** (22), 417–437, (1927).

2.7. Taylor, G.I. "The instability of liquid surfaces when accelerated in adirection perpendicular to their planes", *Proc. R. Soc. A CCI* **192**, (1950).

2.8. R.J. Lang, "Ultrasonic Atomization of Liquids", *J. Accousticai Sot. Amer.* **34**, 6-8, (1962).

2.9. Topp, M. N.; Eisenklam, P. "Industrial and medical uses of ultrasonic atomizers", *Ultrasonics* **10**, 127–133, (1972).

2.10. A. Aruchamy and M. K. Agarwal, in Photo electrochemistry and Photovoltaics of Layered Semiconductors, ed. A. Aruchamy (Kluwer, Dordrecht, 1992) Physics and Chemistry of Materials with Low Dimensional Structures, Vol. 14, p. 319.

2.11. Pisoni, A.; Jacimovic, J.; Barišić, O.S.; Walter, A.; Náfrádi, B.; Bugnon, P.; Magrez, A.; Berger, H.; Revay, Z.; and Forró, L. "The Role of Transport Agents in MoS_2 Single Crystals", *J. Phys. Chem. C* **19 (8)**, 3918-3922, (2015).

2.12. Al-Hilli, A. A. and Evans, B. L. “The preparation and properties of transition metal dichalcogenide single crystals”, *J. Cryst. Growth* **15**, 93, (1972).

2.13. Agarwal, M. K.; Patel, H. B.; and Nagireddy, K. “Growth of single crystals of WSe2 by sublimation method”, *J. Cryst. Growth* **41**, 84-86, (1977).

2.14. Agarwal, M. K.; Reddy, K. N.; Patel, H. B. “Growth of tungstite single crystals by direct vapor transport method”, *J. Cryst. Growth* **46**, 139-142, (1979).

2.15. Agarwal, M. K.; Wani, P. A.; Patel, P. D. “Vapour growth and characterization of $Mo_{0.5}W_{0.5}Se_2$ single crystals”, *J. Cryst. Growth* **49**, 693-695, (1980).

2.16. Späh, R.; Elrod, U.; Lux - Steiner, M.; and Bucher, E. “pn Junctions in Tungsten Diselenide”, *Appl. Phys. Lett.* **43**, 79, (1983).

2.17. Sinton, R. A.; and Cuevas, A. “Contactless Determination of Current-Voltage Characteristics and Minority-Carrier Lifetimes in Semiconductor from Quasi-Steady-State Photoconductance Data”, *Appl. Phys. Lett.* **69**, 2510-2512, (1996).

2.18. Watts, J. F.; and Wolstenholme, J. “An Introduction to Surface Analysis by XPS and AES”, *Wiley* (2003).

2.19. Marple, V.A.; Willeke, K. “Impactor design”, *Atmos. Environ.* **10**, 891–896, (1976).

2.20. Hering, S.V. “Impactors, cyclones, and other inertial and gravitational collectors”, *Air Sampl. Instrum.* **8**, 279–321, (1995).

2.21. Obaidullah, M.; Bram S.; and Ruyck, J. D. “An Overview of PM Formation Mechanisms from Residential Biomass Combustion and Instruments Using in PM Measurements” *International Journal of Energy and Environment* 12, 41-50, (2018).

2.22. Giechaskiel, B., Wang, X., Horn, H., Spielvogel, J., Gerhart, C., Southgate, J., Jing, L., Kasper, M., Drossinos, Y., & Krasenbrink, A. “Calibration ofcondensation particle counters for legislated vehicle number emission measurements”, *Aerosol Science and Technology,* **43**,1164–1173, (2009).

2.23. Agarwal, J., & Sem, G. “Continuous flow, single particle-counting condensation nucleus counter”, *Journal of Aerosol Science*, **11**, 343–357, (1980).

2.24. Wang, X., Caldow, R., Sem, G., Hama, N., & Sakurai, H. “Evaluation of a condensation particle counter for vehicle emission measurement:experimental procedure and effects of calibration aerosol material”, *Journal of Aerosol Science*, **41**, 306–318, (2010).

2.25. Hering, S., & Stolzenburg, M. “A method for particle size amplification by water condensation in laminar, thermally diffusive flow”, *Aerosol Science and Technology* **39**, 428–436, (2005).

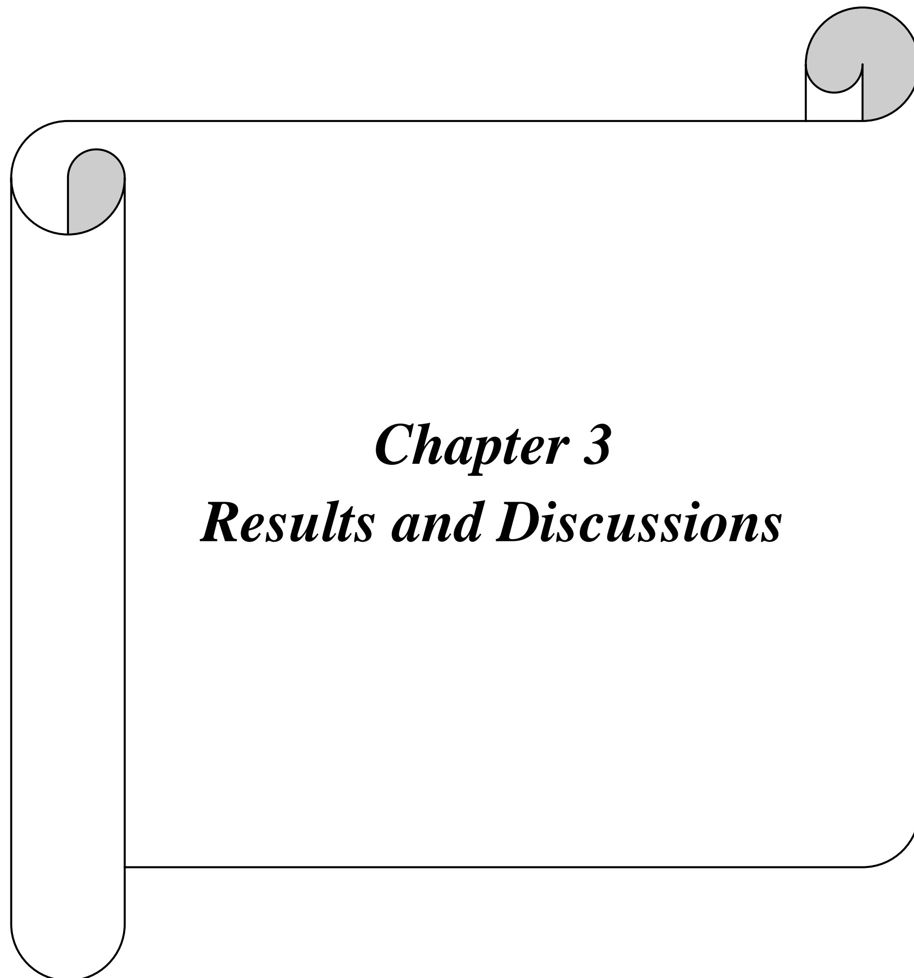
Chapter 3
Results and Discussions

Chapter 3: Results and Discussions

This chapter describes the results obtained in this work. In particular, the first part of this chapter focuses on the effect of H_2O in the synthesis of amorphous AlO_x thin film using mist-CVD from $Al(acac)_3$ and the CH_3OH/H_2O system. The effects of exposing these films to H_2O or CH_3OH mists after synthesis to understand the surface chemistry of the growth surface is also carefully discussed in this part. As a second topic, the effect of deposition parameters, including carrier gas flow, furnace temperature, precursor concentration, and mesh bias supply, on the film properties of AlO_x thin film is discussed. The size distribution of mist particles monitored by particle counter at both inlet and outlet positions A and B for each deposition condition are also discussed in this section. The latter of this chapter focus on the effect of the addition of $Ti(acac)_4$ during the synthesis of $Al_{1-x}Ti_xO_y$ thin films by mist-CVD from $Al(acac)_3$ for different precursor mixing ratios γ [$=Ti(acac)_4/Al(acac)_3$] is examined under the optimized deposition condition of AlO_x thin films provided in the first part of this chapter.

3.1 Role of H_2O in the synthesis of amorphous AlO_x using mist-CVD from $Al(acac)_3$ and CH_3OH/H_2O system for surface passivation and electrical insulator layers

In this section, the effect of H_2O added during the synthesis of AlO_x thin films from Al(acac)3 and CH_3OH by atmospheric-pressure mist-CVD were investigated by examining film deposition characteristics. The effects of exposing these films to H_2O or CH_3OH mists after synthesis was also assessed to understand the surface chemistry of growth surface. Also, the effect of H_2O as an additive during the synthesis of AlO_x thin films on their junction properties at the AlO_x/c-Si interface; like surface passivation capability and electrical insulator layers performances were reported.

3.1.1 Synthesis of AlO_x by mist-CVD with $Al(acac)_3$ and CH_3OH/ H_2O

Figure 3.1.1(a) plots the AlO_x film deposition rates as a function of the CH_3OH: H_2O volume ratio at two different T_f values (350 and 400 °C). The film deposition rates are seen to have decreased from 13.8 to 3.7 nm/min at 400 °C and from 8.92 to 2.4 nm/min at 350 °C as the proportion of H_2O r was increased from 0 to 30 vol%. These results suggest that the decomposition rate of the $Al(acac)_3$ promotes higher T_f values and that the addition of H_2O suppresses film growth.

In **Figure 3.1.2(b)**, the deposition rates for AlO_x thin films at a CH_3OH: H_2O ratio of 9:1 are plotted as a function of the inverse of T_f. Thermal activation energy is calculated from Arrhenius plots as

$$Deposition\ rate = Aexp\left(-\frac{\Delta E_a}{RT}\right), \qquad (3.1)$$

where ΔE_a is the thermal activation energy, R is the gas constant, and T is temperature. The film deposition rate evidently increased with increasing temperature, with thermal activation energy, ΔE_a, of 42-49 kJ/mol up to approximately ~380 °C. However, ΔE_a was reduced to 31-36 kJ/mol above 380 °C, suggesting that the growth chemistry changed from supply control regime to diffusion control regime at the interface temperature.[1] The larger ΔE_a value below 380 °C is ascribed to the stability of OH groups at the growth surface in this temperature regime because of sticking probability might be enhanced from this temperature.[3.1]

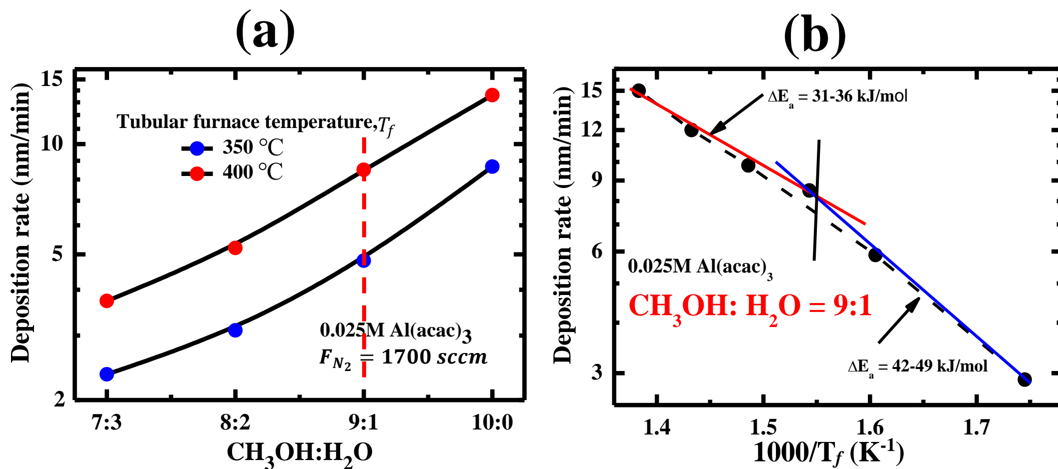

Figure 3.1.1. Deposition rates for AlO_x films during mist-CVD as functions of the CH_3OH: H_2O ratio at a tabular furnace temperature of 350 and 400 °C. (b) Deposition rates for AlO_x films at a CH_3OH: H_2O volume ratio of 9:1 as a function of the inverse of T_f.

Figures 3.1.2. (a) presents the FTIR spectra of 100-nm-thick AlO_x thin films fabricated using various CH_3OH: H_2O ratios, while **Table 3.1.1** summarizes the local vibrational modes for AlO_x related to the absorption peaks obtained from films on c-Si.[2-9] The most valuable peaks related to Al-O and O-Al-O between 500-1200 cm^{-1} represents in the **Figure. 3.1.2 (b)**. Also, the AFM images of the commensurable films are observed in **Figure. 3.1.2(c)**. In the case of AlO_x films synthesized using solely CH_3OH as the solvent, the Al(OH) stretching peak in the range of 2600-3800 cm^{-1} is prominent. However, this peak disappears as H_2O is added to the CH_3OH solvent, while peaks related to Al-O (400-550 cm^{-1}), O-Al-O (550-750 cm^{-1}), and Si-O-Al (~1100 cm^{-1}) emerge. The first two peaks can be assigned to the Al-O stretching and bending modes (expected to appear at approximately 440 and ~603 cm^{-1}, respectively) for octahedral AlO_6 as well as the stretching vibration of tetrahedral (AlO_4) (which should appear in the range of 728-886 cm^{-1}). Several fine peaks were also observed attributing to Si-OH, Si-O-Si, or Al-O-Si band at 300-1100 cm^{-1}, which were almost independent of a CH_3OH to H_2O ratio. These findings suggest that these fine peaks originate from the Si-O-Si or Al-O-Si local bonding at the AlO_x/n-Si interface.

Table 3.1. 1. Local vibration modes of AlO_x related FTIR peaks.

Wavenumber (cm^{-1})	Molecule	Vibrational Mode	Surrounding	Reference
400-530	Al-O	Stretching	Octahedral matrix	3.2-6
550-750	O-Al-O	Bending	Octahedral and tetrahedral matrix	3.2-7
750-850	Al-O	Stretching	tetrahedral matrix	3.2-7
900-1200	Si-O/O-Si-O/Si-OH	Stretching	SiO/SiO_2	3.8-3.9

1300-1750	H-O-H	Bending	tetrahedral and octahedral γ-Aluminum ions	3.6
2300-2350	O-C-O	Stretching	Al_2O_3	3.5
3000-3600	Si-OH	Stretching		3.8
2600-3800	O-H	Stretching	Al-OH	3.6

The AFM images demonstrate that the root means square (RMS) roughness of the films decreased continuously as the H_2O was added, from 3.87 nm for the film made using only CH_3OH to 1.76 nm using 30 vol% H_2O. These results suggest that the surface roughness was primarily determined by residual Al(OH) groups near the growth surface (**Figure 3.1.2(c)**).

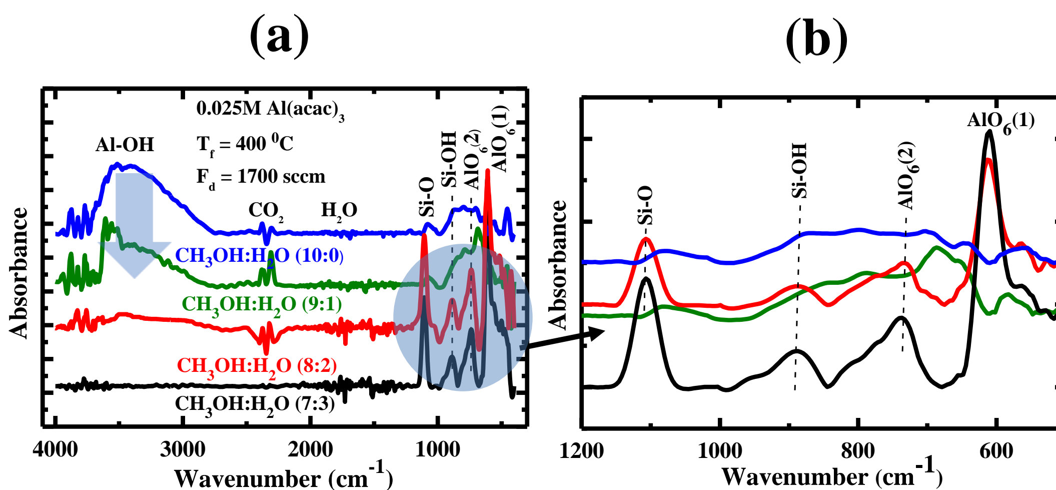

(c)

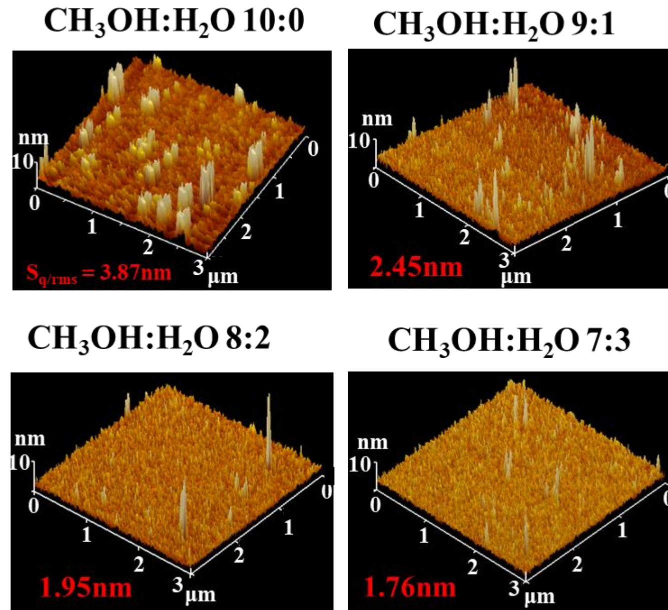

Figure 3.1. 2. (a) FTIR spectra of AlO_x thin films fabricated by mist-CVD using various CH_3OH: H_2O ratios at 400 ºC, (b) FTIR spectra related to Al-O and O-Al-O between 500 and 1200 cm^{-1}, (c) AFM images of the corresponding AlO_x films.

Figure 3.1.3 provides the refractive index (*n*) spectra of the same AlO_x thin films as acquired from spectroscopic ellipsometry (SE) analysis using a single classical oscillator model. The reference *n* value of amorphous ALD-AlO_x has been extracted from Ref. 10. The *n* values increased with the increasing proportion of H_2O in the solvent. The *n* value of AlO_x thin film fabricated by CH_3OH: H_2O =7:3 was almost identical to that for ALD-AlO_x.[3.10,3.11] These findings imply that the rigidity and surface roughness of the AlO_x network can be controlled by adjusting CH_3OH/H_2O ratio.

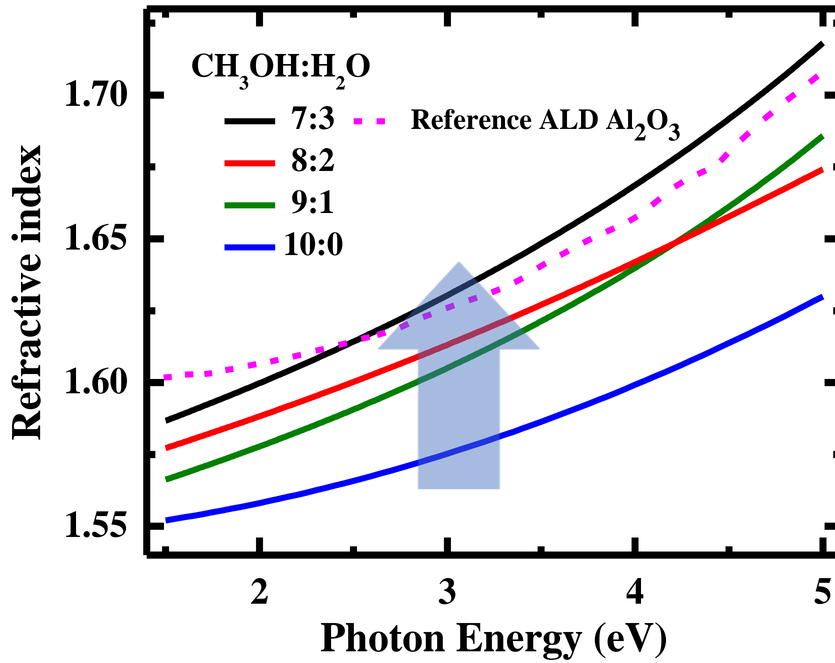

Figure 3.1. 3. The *n* spectra of AlO_x thin films produced using mist-CVD with different CH_3OH: H_2O ratios at 400 °C.

3.1.2 Post-fabrication exposure of Al(OH) and AlO_x network to H_2O and CH_3OH

Figures 3.1.4. (a) and (b) provide the FTIR spectra and AFM images obtained from a 100-nm-thick Al(OH) film fabricated using solely CH_3OH at 400 °C both before and after exposure to a H_2O mist. **Figures 3.1.4.** (c) and (d) present the *n* spectra and the film thicknesses of these same films. The FTIR and AFM data confirm that the as-deposited films generated an intense peak in the range of 2700-3600 cm^{-1} attributed to the Al(OH) stretching absorption and that the film was porous with the significant surface roughness (RMS =3.87 nm). During the first 5-20 min. of H_2O mist exposure, the band at 2700-3500 cm^{-1} became less intense while the peak related to non-symmetric Al(OH) stretching at 3500-3700 cm^{-1} remained relatively constant at first but eventually disappeared. In contrast, the peak attributed to octahedral AlO_6 at 500-700 cm^{-1} became more intense. The AFM images also show decreases in surface roughness with continued exposure to the H_2O mist. The SE results demonstrate that the *n* values were increased with prolonged exposure to the H_2O mist as the film was etched. Conversely, no significant changes in the FTIR spectra, film morphology, or film thickness were observed in the case of the AlO_x generated using a CH_3OH: H_2O =7:3 after H_2O mist exposure for 40 min. These findings suggest that the H_2O mist

removed the Al(OH) groups near the growth surface as the film was etched several mono-layer.

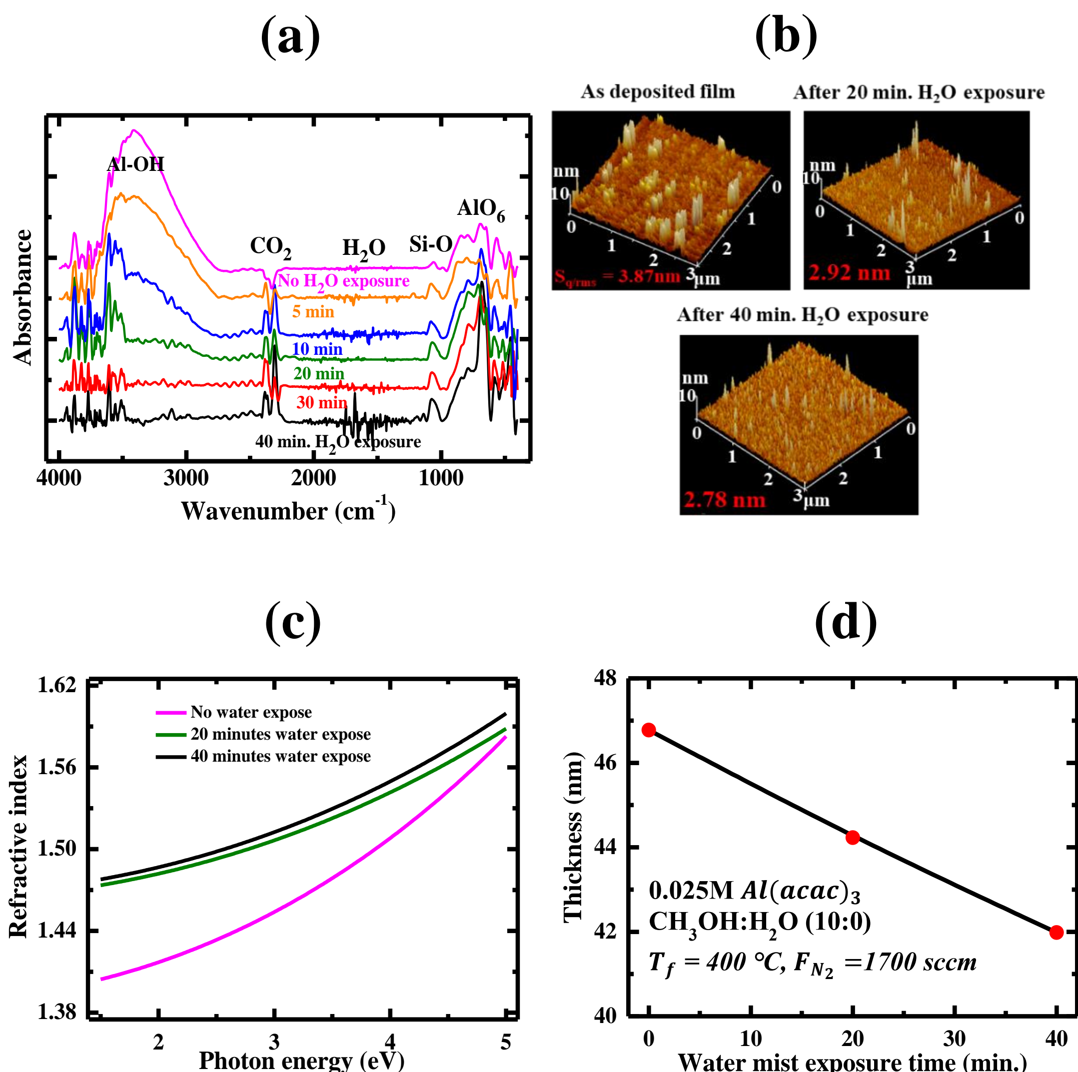

Figure 3.1. 4. (a) FTIR spectra of an Al(OH) thin-film fabricated at 400 ℃. (b) AFM images of the corresponding films. Variation in the (c) *n* spectra and (d) film thickness of Al(OH) films during exposure to a H_2O mist.

Figures 3.1.5 (a) and (b) provide FTIR spectra and n-spectra of a 100 nm thick AlO_x thin film fabricated using a CH_3OH: H_2O ratio of 7:3 at 400 ℃ before and after exposure to a CH_3OH mist. **Figure 3.1.5** (c) represents the AFM image of the corresponding films. In contrast to the effects of H_2O mist exposure, the application of a CH_3OH mist generated the marked increases in the Al(OH) absorption band at 2800-3600 cm-1 together with decreases in the *n* value. The AFM images also indicate

increases in surface roughness after the CH_3OH mist exposure. These results suggest that the H_2O mist acts to scavenge residual OH groups generated by CH_3OH at the growth surface.

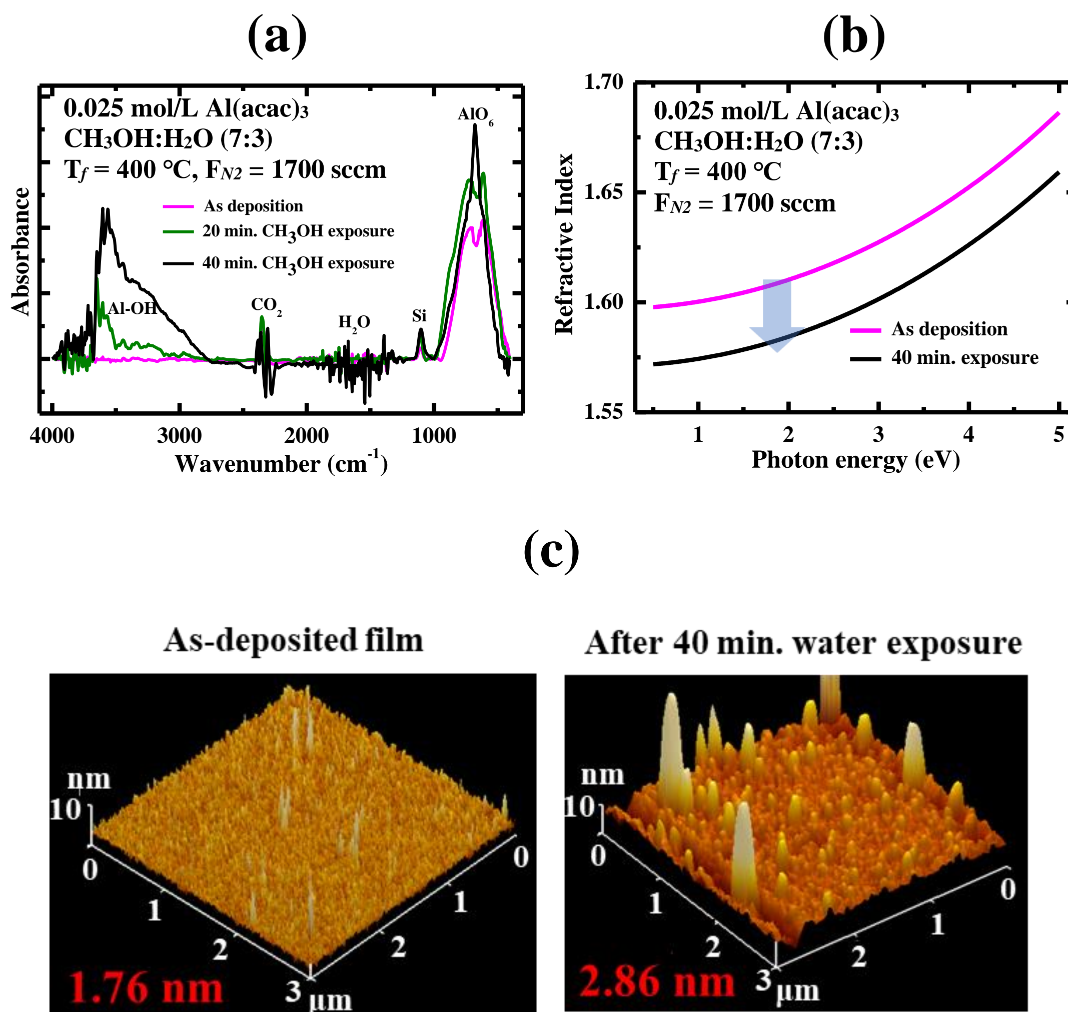

Figure 3.1. 5. (a) FTIR spectra of an AlO_x thin film fabricated at a T_f of 400 ºC exposed to a CH_3OH mist. Changes in the (b) *n* spectra and (c) AFM images of the film before and after CH_3OH mist exposure.

3.1.3 Role of H_2O as an additive during the growth of mist-CVD of AlO_x thin films

Figures 3.1.6. (a) shows the high-speed camera image of CH_3OH/H_2O co-solvent mist at the inlet and outlet positions of the tubular furnace at different CH_3OH to H_2O ratios. The flux and speed of CH_3OH/H_2O mist decreased with the increasing H_2O to the CH_3OH ratio despite the same flow of N_2. These findings originate from the physicochemical property of the CH_3OH/H_2O solution system determines the

generation rate of mist precursor and fine structure of AlO_x films. The addition of H_2O in the CH_3OH solution suppresses the generation of CH_3OH mist because of the formation of a chemically stable complex network of H_2O and CH_3OH molecule due to hydrogen bond in H_2O.[3.12,3.13]

(a)

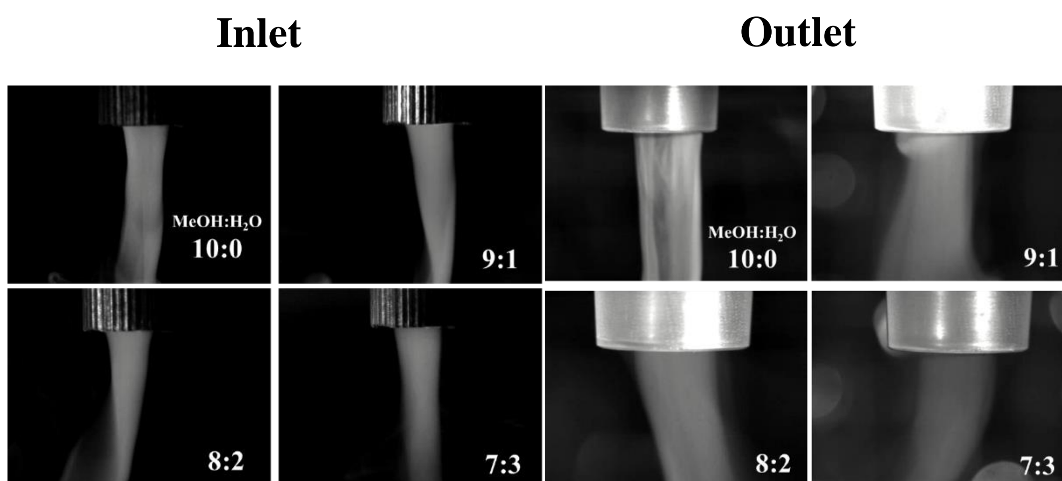

(b)

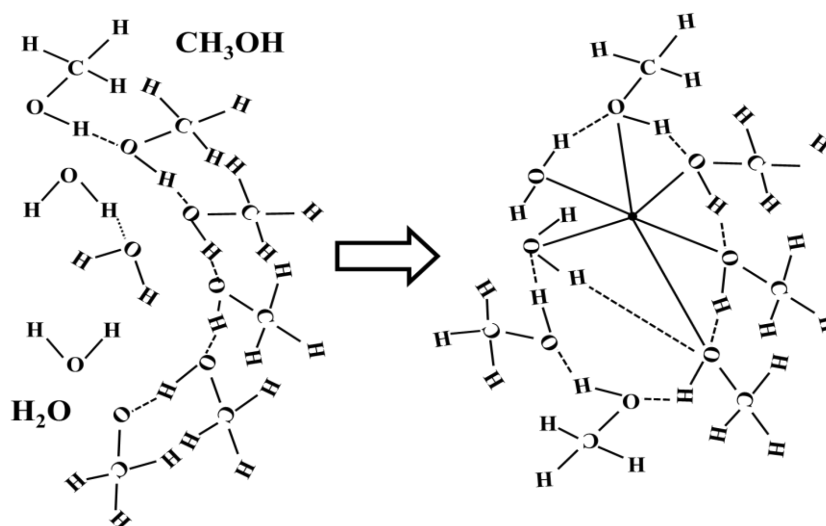

Figure 3.1. 6. (a) High-speed camera images of CH_3OH/H_2O mist at the inlet and outlet positions of the tubular furnace at different CH_3OH to H_2O ratios. (b) Schematic of the fine structure of the CH_3OH/H_2O solution at lower and higher H_2O mixing conditions.

Figures 3.1.7 (a) and (b) show a schematic diagram of the growth surfaces associated with the formation of AlO_x films using CH_3OH: H_2O ratios of 10:0 and 7:3,

respectively. When using solely CH_3OH, a high concentration of Al(OH) groups appeared near the growth surface (see also Fig. 3.1.4.(a)). The post-fabrication H_2O mist exposure experiments demonstrated that this treatment removed -OH groups and promoted the formation of AlO_6 [Figures. 3.1.4. (a) and (b)]. Etching of the film also occurred, together with increases in the n value up to ~1.6. The SE analysis also showed that n increased from 1.4 to 1.5 at 2.85 eV following a 40 min exposure to a H_2O mist, which corresponds to a thickness of 3-4 nm (Figures 3.1.4. (c) and (d). These findings suggest the presence several monolayers that form a flexible Al(OH) network with a significant surface roughness near the so-called "growth zone". In contrast, the growth of AlO_x using a CH_3OH: H_2O ratio of 7:3 proceeded on nearly the atomic scale, while the application of H_2O mist to such films removed -OH groups on the top surface.

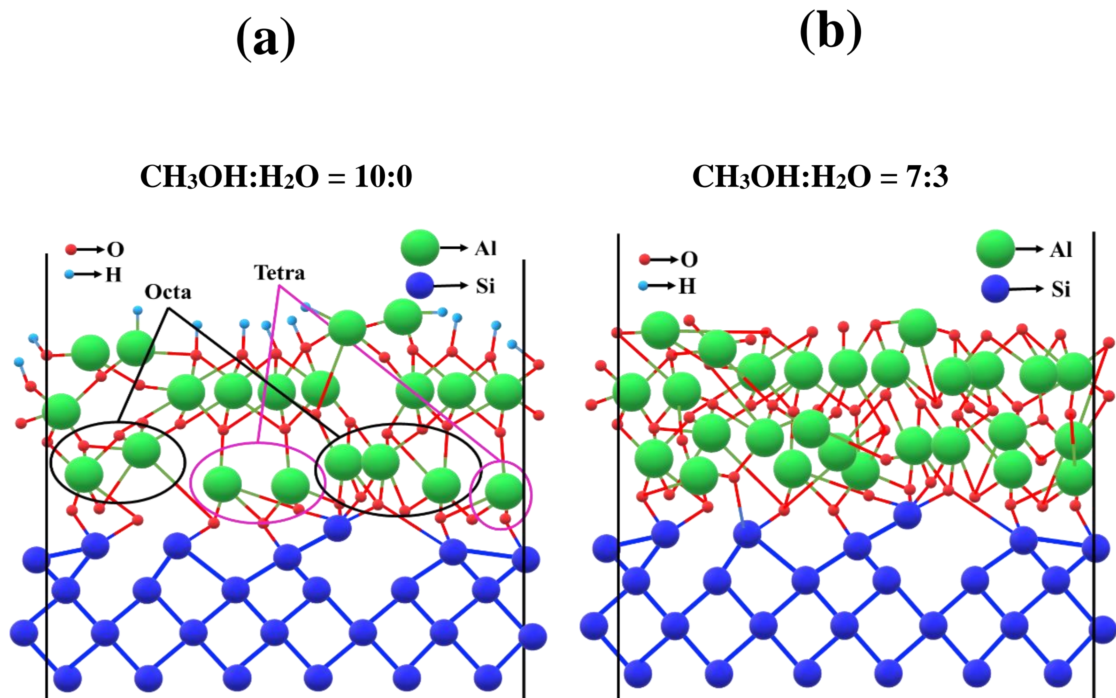

Figure 3.1. 7. Schematic diagram of the growth surface of AlO_x films for CH_3OH: H_2O ratios of (a) 10:0 and (b) 7:3.

3.1.4 Junction properties at the mist-CVD AlO_x/p-Si interface

Figure 3.1.8. summaries the minority carrier life time, τ_{eff} and recombination velocity, S, values for 50-nm-thick AlO_x films produced at various CH_3OH: H_2O ratios

on n-Si substrates, as obtained using μ-PCD. The S values were determined from the effective lifetimes using the following equation.

$$\frac{1}{\tau_{eff}} = \frac{1}{\tau_{bulk}} + \left[\frac{W}{2S} + \frac{1}{D_n}\left(\frac{W}{\pi}\right)^2\right]^{-1} \quad (3.2)$$

where τ_{bulk} is the bulk lifetime of the Si substrate, S is the surface recombination velocity, W is the substrate thickness (250±.060 μm), and D_n is the diffusion length (37 nm for c-Si).[3.14] The τ_{eff} value was increased markedly to 718 μs together with a lowering of S to 16 cm/s upon adjusting the CH_3OH: H_2O ratio to 7:3. These values are quite close to those obtained using ALD and PECVD, which suggests that the AlO_x fabricated by mist-CVD can significantly passivate the c-Si substrate.[3.15, 3.16]

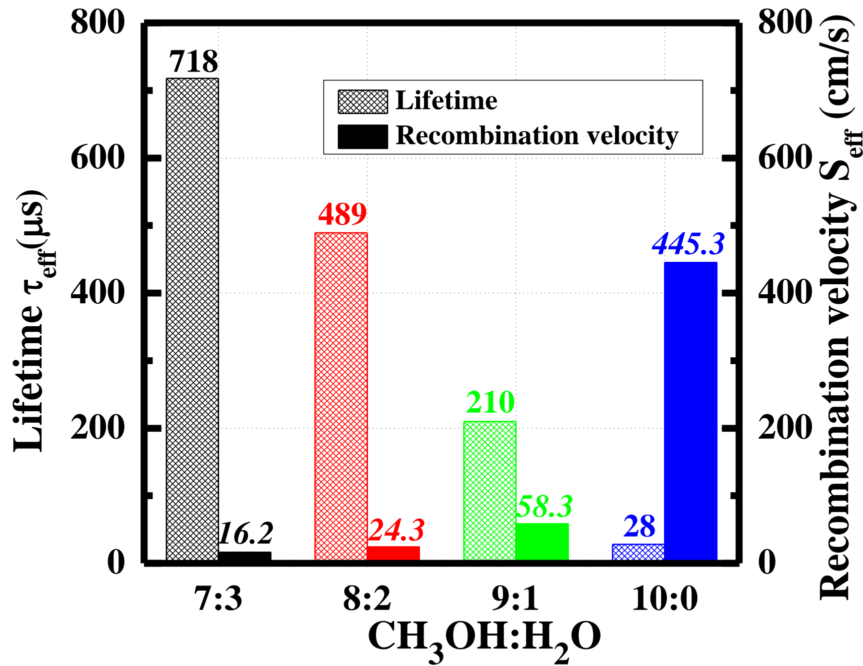

Figure 3.1. 8. Effective minority carrier lifetime, τ_{eff}, and carrier recombination velocity, S, values for AlO_x films generated by mist-CVD with various CH_3OH: H_2O ratios.

Figure 3.1.9. (a) shows the J-E curves obtained from 50-nm-thick AlO_x films fabricated using various CH_3OH: H_2O ratios. The breakdown voltage, EBD, is observed to have continuously shifted, from 2.9 MV/cm for the film made using solely CH_3OH to 6.9 MV/cm for the specimen produced with a CH_3OH:H_2O ratio of 7:3. The leakage

current was also evidently reduced as the H_2O proportion was increased. These results imply that the removal of -OH groups from the AlO_x network is crucial to obtaining high performance from the AlO_x as a gate insulator in field-effect transistors (FETs) and as a passivation layer for c-Si photovoltaics.[3.17,3.18]

Figure 3.1.9 (b) plots both negative fixed-charge density, Q_f, and interface trap density, D_{it}, values as functions of the CH_3OH:H_2O ratio. These data were determined from the C-V characteristic of Al/AlO_x/p^{++}-Si/Al capacitors at high and low frequencies. The intrinsic energy level of p-Si crosses the Fermi level, suggesting that significant inversion occurred at the AlO_x/p-Si interface, similar to the behavior exhibited by SiO_2/p-Si capacitors.[3.17,3.18] Q_f values were calculated using the equation

$$V_{FB} = \varphi_{Ms} - {Q_f}/{C_{ox}} \qquad (3)$$

where φ_{MS} is the Al-Si work function difference (1.1±0.5 eV)[3.19] and C_{ox} is the oxide capacitance. The Q_f values were found to be on the order of 10^{12} cm^{-2}, with a maximum value of 2.4×10^{12} cm^{-2} for the AlO_x films with a CH_3OH: H_2O ratio of 7:3. This value is compatible with those reported for AlO_x produced using ALD (10^{13} cm^{-2}).[3.16,3.20]

Also, values for the density of interface traps, D_{it}, were determined from the C-V characteristics obtained at different measurement frequencies, through the equation;

$$D_{it}(\varphi_s) = \left({C_{ox}}/{q}\right)\left({C_{hf}}/{(C_{ox} - C_{hf})} - {C_{lf}}/{(C_{ox} - C_{hf})}\right) \quad (cm^{-2}eV^{-1}), \qquad (4)$$

where C_{lf} and C_{hf} are the capacitance values measured at low and high frequency, respectively. The resulting D_{it} value of 4.2×10^{10} cm^{-2}eV^{-1} was also close to that of 1.04×10^{10} cm^{-2}eV^{-1} reported for films fabricated using radio frequency magnetron sputtering and PE-CVD.[15,16] These findings indicate that the AlO_x films made using mist-CVD exhibit good passivation and junction characteristics at the AlO_x/c-Si interface and those properties can be tuned by adjusting both T_f and the CH_3OH: H_2O ratio.

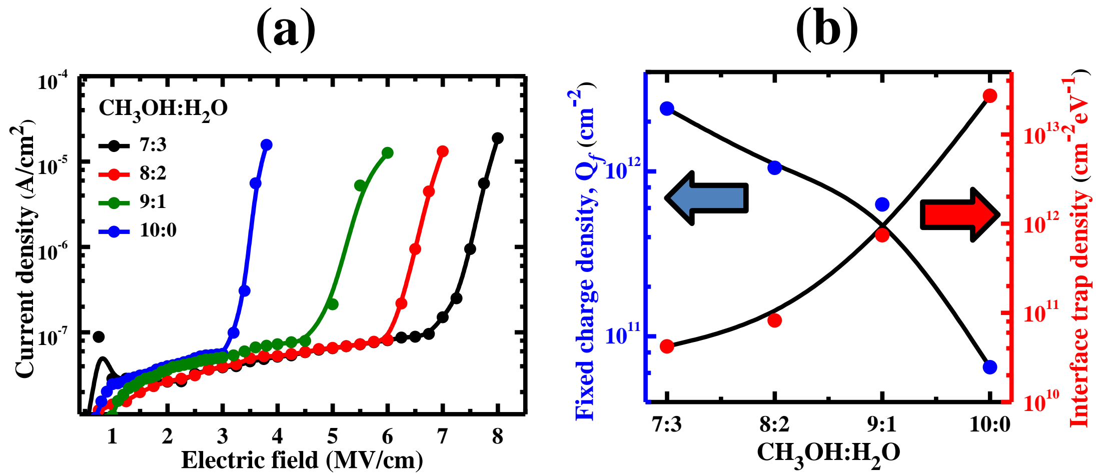

Figure 3.1. 9. (a) J-E curves obtained from Al/AlO_x/p^{++}-Si/Al capacitors with films produced at various CH_3OH: H_2O ratios. (b) Q_f and D_{it} values for Al/AlO_x/p^{++}-Si/Al capacitors as functions of CH_3OH: H_2O ratio.

3.2 Synthesis of AlO_x thin films monitored by a fast-scanning mobility particle analyzer and applied as a gate insulating layer in the field-effect transistors

Here, the effect of deposition parameters on the film properties of mist-CVD a-AlO_x films is demonstrated, which include carrier gas flow, furnace temperature, precursor concentration, and mesh bias V_m as variables. The carrier gas flow determines the residence time of deposition precursor, furnace temperature T_f dominates the surface reaction on the growth surface, and mesh dc bias is supplied between two mesh electrodes with a 2 cm distance for charging mist precursors. The size distribution of mist particles was monitored by using particle counter at both inlet and outlet positions A and B **(Fig. 2.6).**

3.2.1 Film properties of AlO_x thin films at different deposition parameters

Figure 3.2.1(a) shows the film deposition rate of AlO_x thin films grown by mist-CVD as a function of F_d: the analyzed AlO_x thin films were fabricated using a 0.025 mol/L $Al(acac)_3$ solution, CH_3OH/H_2O ratio of 7:3, a T_f of 400 °C, without supplying Vm. The film deposition rate decreased from 7.35 to 1.78 nm/min and tend to saturate when F_d was increased from 600 to 3000 sccm. **Figure 3.2.1(b)** shows the AFM images

of the corresponding AlO_x thin films. The root means square (RMS) roughness of a 20×20 μm^2 area of the films decreased significantly from 83.3 to 6.02 nm when the F_d was increased from 600 to 3000 sccm. These results are attributed to the suppression of the aggregation of the charged mist particles during their transport, because of the short residence time of the deposition precursor. Consequently, the secondary reaction was suppressed, resulting in a low value of surface roughness. Further, **figure 3.2.1(c)** provides the n spectra of the ~30 -nm -thick AlO_x thin films, which were obtained from an SE analysis using a single classical oscillator model. The reference n spectrum of amorphous ALD-AlO_x was referred from literature.[3.10] The n values increased with an increase in F_d, yielding a spectrum similar to that of ALD-AlO_x at an F_d from 2400 sccm. These results suggest that F_d determines the residence time of the $Al(acac)_3$ mist precursor and the surface diffusivity of the deposition precursor at the growth surface.[3.10,3.21]

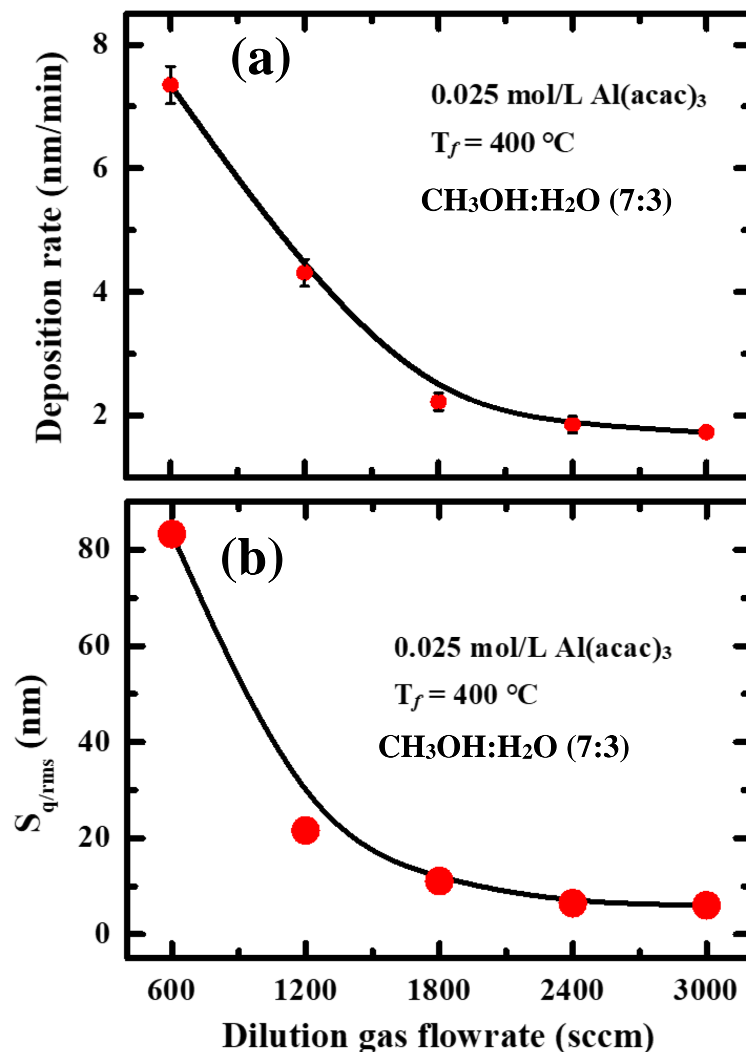

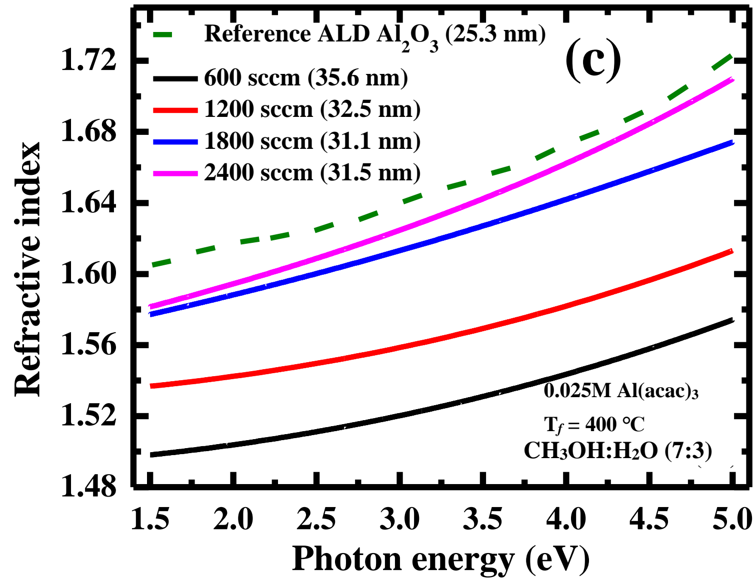

Figure 3.2. 1. (a) Deposition rate for AlO_x thin films through mist-CVD as a function of F_d, in an CH_3OH:H_2O ratio of 7:3 at a T_f of 400 °C. (b) RMS roughness and (c) n spectra of the corresponding AlO_x thin films.

Figure 3.2.2(a) presents the film deposition rate of AlO_x thin films fabricated at different T_f values; the AlO_x thin films employed in the analysis were fabricated using 0.025 mol/L and F_d of 2400 sccm. The film deposition rate increased from 1.85 nm/min to 5.7 nm/min and tend to saturate as T_f was increased from 400 °C to 600 °C. This result suggests that the decomposition rate of the $Al(acac)_3$ precursors was prompted and tend to saturate at higher temperatures, which showed a thermally activation has been reported elsewhere.[3.1,3.22,3.23] The RMS value obtained in 20×20 μm^2 area and the n values of the corresponding 50 -nm -thick AlO_x thin films are shown in **Figure 3.2.2.(b)** and **(c),** respectively. When T_f was increased from 400 °C to 600 °C, the n value increased from 1.62 to 1.66-1.67 at 3.5 eV, whereas RMS values for 20×20 μm^2 area of the films decreased from 6.45 to 1.30 nm. These results suggest that the diffusivity of the deposition precursor is enhanced at the growth surface and promotes the removal of residual Al(OH) bonds.

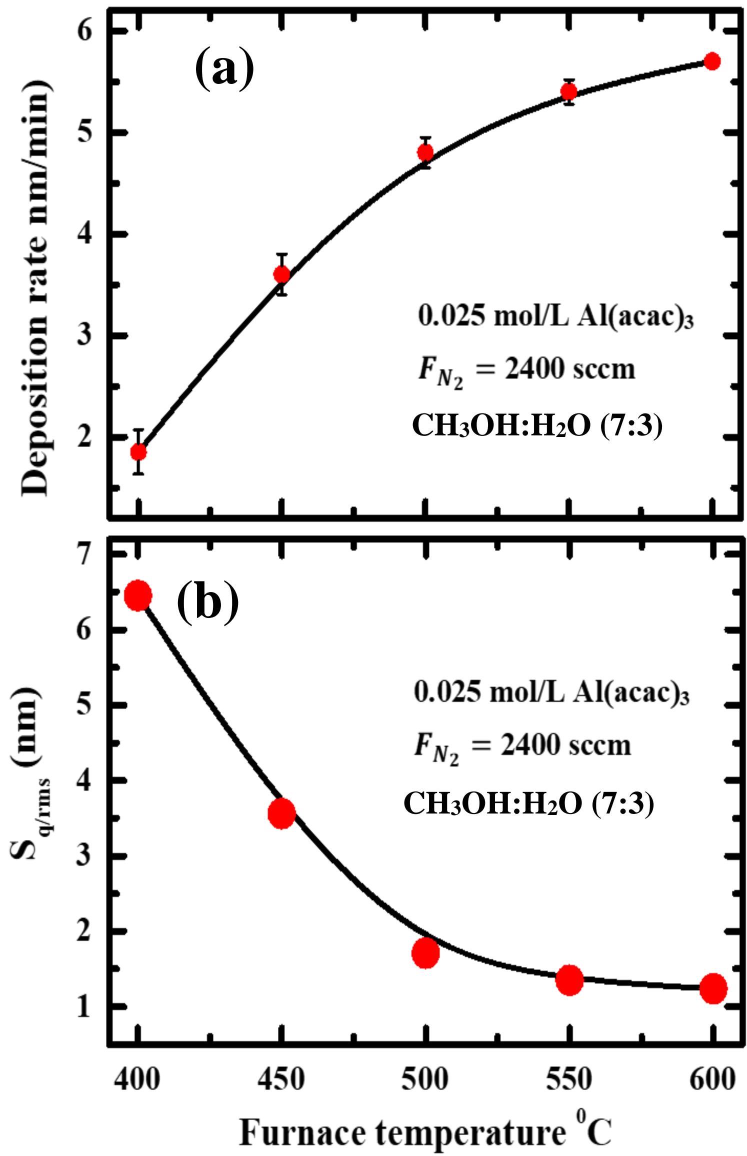

(a)
Deposition rate nm/min
0.025 mol/L Al(acac)3
F_{N_2} = 2400 sccm
CH3OH:H2O (7:3)
(b)
$S_{q/rms}$ (nm)
0.025 mol/L Al(acac)3
F_{N_2} = 2400 sccm
CH3OH:H2O (7:3)
400 450 500 550 600
Furnace temperature ^{0}C

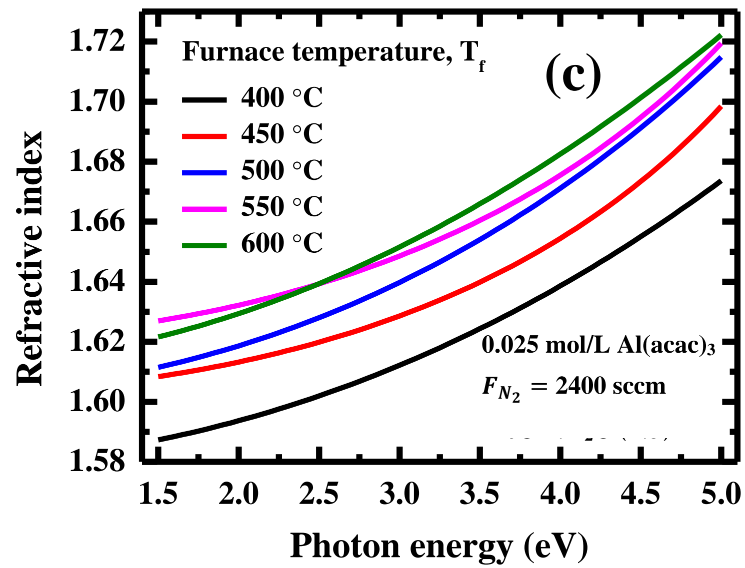

Furnace temperature, T_f
400 °C
450 °C
500 °C
550 °C
600 °C
(c)
Refractive index
0.025 mol/L Al(acac)3
F_{N_2} = 2400 sccm
Photon energy (eV)

Figure 3.2. 2. (a) Deposition rate for AlO_x thin films by mist-CVD fabricated at different values of T_f, with a 0.025M $Al(acac)_3$, a $CH_3OH:H_2O$ ratio of 7:3, and an F_d of 2400 sccm. (b) RMS roughness and (c) *n* spectra of the corresponding AlO_x thin films.

Figure 3.2.3(a) shows the film deposition rate of AlO_x thin films as a function of solution concentration of $Al(acac)_3$ concentration; the analyzed AlO_x thin films were fabricated an F_d of 2400 sccm and T_f of 550 °C. The RMS value and *n*-spectra of the corresponding ~50 -nm -thick AlO_x thin films are shown in **Figures 3.2.3(b)** and **(c)**, respectively. The film deposition rate decreased from 7 nm/min for 0.035 mol/L to 1.4 nm/min for 0.005 mol/L of $Al(acac)_3$. An increase in *n*-value and decrease in surface roughness was observed despite unchanged film thickness. These results suggest that a low $Al(acac)_3$ concentration suppresses the aggregation of mist precursors during the transport of mist and/or promotes the diffusivity of the mist precursors at the growth surface. Accordingly, using a 0.015 mol/L $Al(acac)_3$, dense AlO_x network was obtained; the AlO_x network had an *n*-value of 1.68 at 3.5 eV and small surface roughness (RMS value; 0.96 nm in 20×20 μm^2 area) at a deposition rate of 4 nm/min.

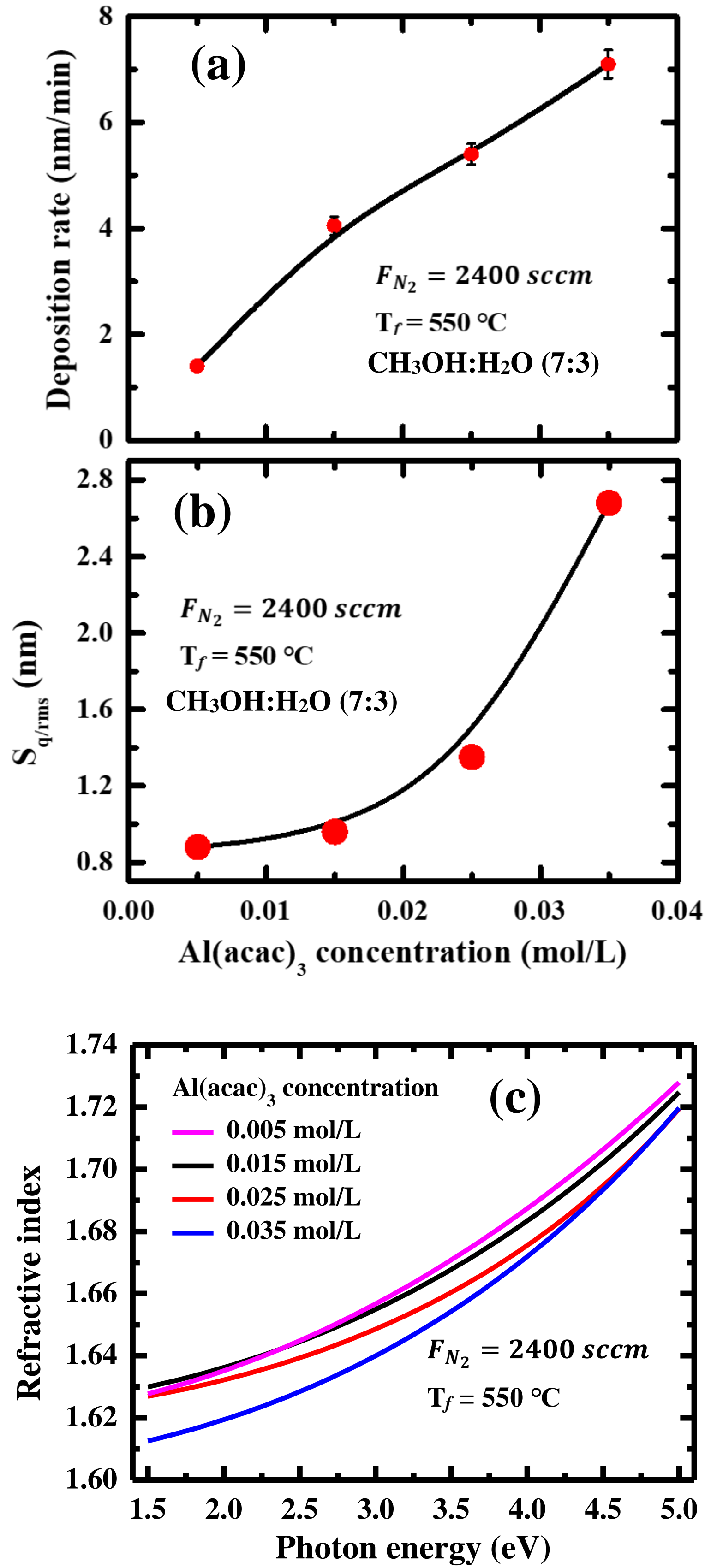

Figure 3.2. 3. (a) Deposition rate and (b) RMS value for AlO_x thin films by mist-CVD fabricated at different solution concentrations of Al(acac)$_3$ with a CH_3OH/H_2O ratio of

7:3 volume ratio, a T_f of 550 °C, and an F_d of 2400 sccm. (c) *n* spectra of the corresponding AlO_x thin films.

3.2.2 Effect of V_m on the film deposition of AlO_x thin films by mist-CVD

Figure 3.2.4(a) shows the film deposition rates of AlO_x thin films fabricated at different V_m values under the optimized conditions, i.e., an F_d of 2400 sccm, T_f of 550 °C, and 0.015 mol/L $Al(acac)_3$. The film deposition rate decreased systematically from 4 to 3.8 nm/min when V_m was gradually increased from 0 to 9 kV. The *n* spectra and AFM images of the corresponding ~50 -nm -thick AlO_x films are shown in **Figure 3.2.4(b)** and **(c)**, respectively. AlO_x thin films with an *n*-value of 1.695 at 3.5 eV and small surface roughness were obtained at a film deposition rate of 3.8 nm/min by adjusting V_m to 9 kV.

(a)

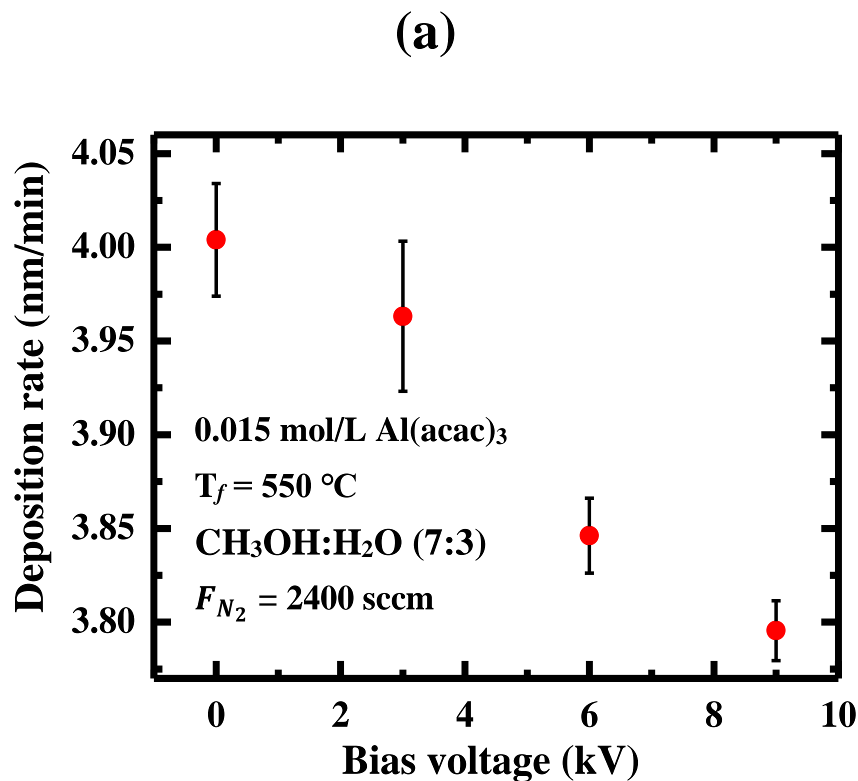

(b)

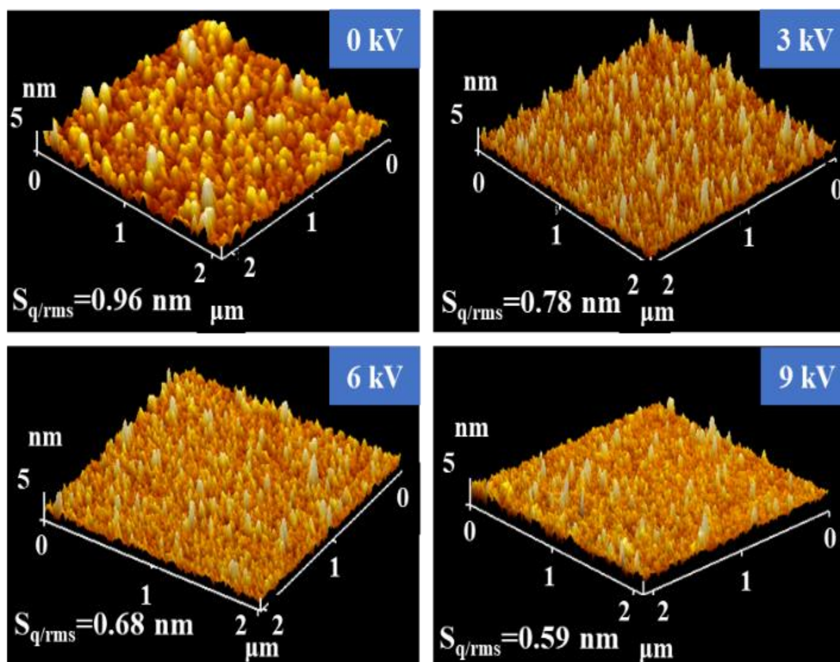

(c)

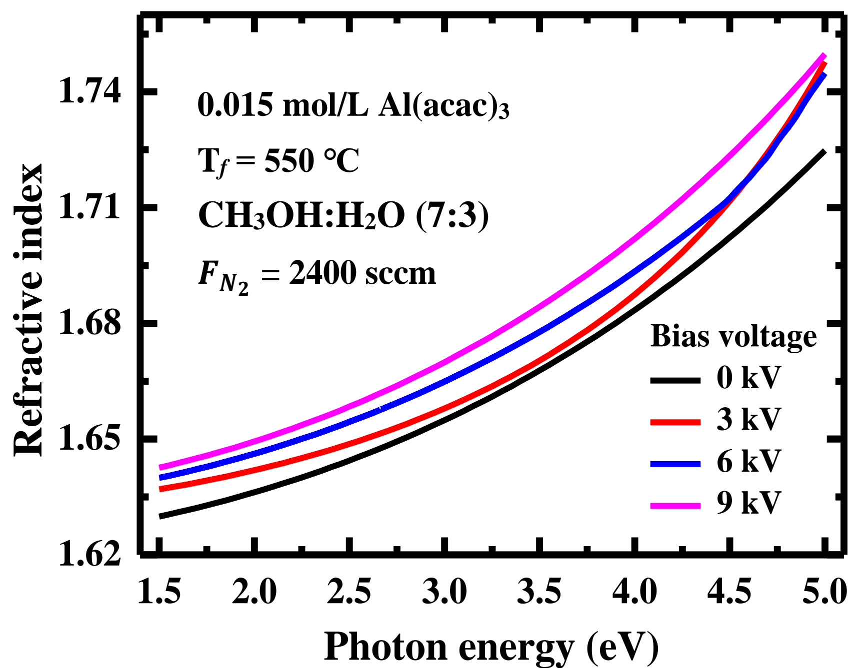

Figure 3.2. 4. (a) Deposition rate for AlO_x thin films through mist-CVD fabricated at different values of V_m, using a 0.015M $Al(acac)_3$ solution and a CH_3OH:H_2O mixture

(7:3 volume ratio), at a T_f of 550 °C, and an F_d of 2400 sccm. (b) AFM image and (c) n spectra of the corresponding ~50 -nm -thick AlO_x thin films.

3.2.3 Size distribution of mist particles monitored by scanning mobility particle analyzer

Figure 3.2.5 shows the size distribution of the mist particles obtained using CH_3OH and H_2O separately and a CH_3OH/H_2O mixture at the inlet position **A** of the tubular furnace (**Figure 1**). The size distribution of mist particles was monitored using a particle analyzer at an F_d of 2400 sccm. The size distribution of CH_3OH mist was maximum for a particle size of ~8 nm and showed a narrow bandwidth at 5 -6 nm. In contrast, the size distribution of de-ionized (DI) H_2O mist was maximum for a particle size of ~70 nm and showed a broad bandwidth at ~100 nm. Further, the size distribution of CH_3OH/H_2O (=7:3) mist was similar to that of DI H_2O mist, with a small contribution of CH_3OH mist for particle sizes of 7 -8 nm. This phenomenon was observed despite the higher quantity of CH_3OH than that of H_2O in the solvent. These results suggest that the effect of H_2O mist on particle size distribution is greater despite the higher composition ratio of CH_3OH in the solvent mixture. This result originates from the higher vapor pressure and lower dielectric constant of CH_3OH than that of H_2O.

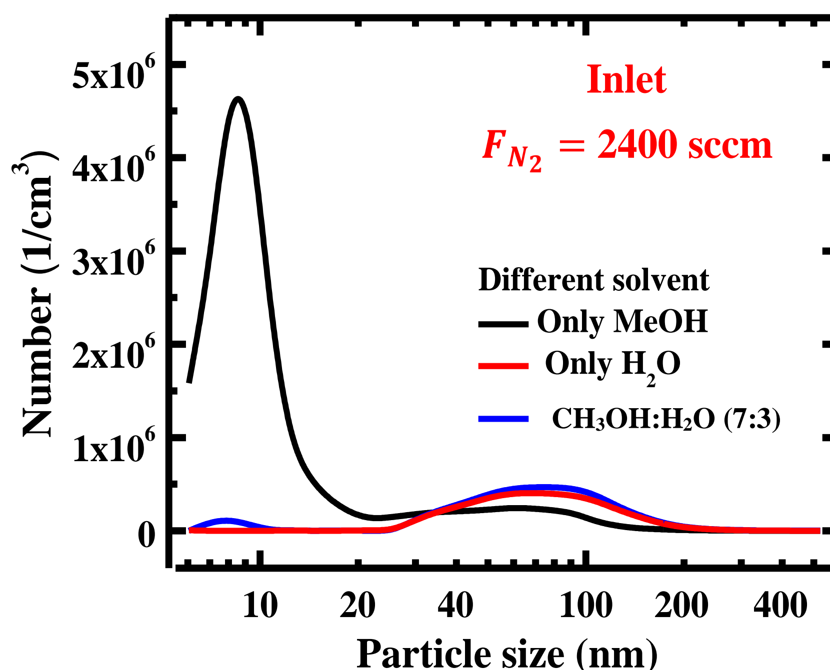

Figure 3.2. 5. Size distribution of CH_3OH and H_2O separately, and CH_3OH/H_2O solvent of (7:3 volume ratio) at an F_d of 2400 sccm at the inlet position **A** of the tubular furnace.

Figure 3.2.6(a) shows the size distribution of $Al(acac)_3/CH_3OH/H_2O$ mist particles at inlet position **A** of the tubular furnace for different values of F_d; the AlO_x thin films were employed in the analysis were fabricated using at 0.025 mol/L $Al(acac)_3$ solution and $CH_3OH.H_2O$ (=7:3) at a T_f of 400 °C. At the inlet position **A**, at the lowest F_d (600 sccm), the size distribution of the mist particles was maximum for particle sizes of 100 -300 nm, and a sub-band peak was observed for the mist particle sizes of 30 -90 nm as a shoulder. At the highest (2400 sccm), the number density of mist particles markedly decreased from 4.6×10^6 to 2×10^6 /cm^3. These results suggest that the residence time of the mist precursor decreases with an increase in F_d. **Figure 3.2.6(b)** shows the size distribution of the mist particle monitored at outlet position **B** of the tubular furnace. At 600 sccm, the number density of the mist particles was negligible, suggesting that the majority of the mist precursors were consumed for the film deposition during their travel in the tubular furnace. At an F_d of 1200 sccm, the number density was maximum for a mist particle size of ~80 nm, with a broad bandwidth of 100 -200 nm. Further increase in F_d to1800 and 2400 sccm decreased the average size of the mist particles to 50 -60, and 30 -40 nm, respectively, additionally, a marked increase in their density was observed. Thus, an increase in F_d promoted the generation of small mist particles of 30 -60 nm; the increase in F_d suppressed the secondary reaction in the furnace because of the short residence time of the mist precursor.

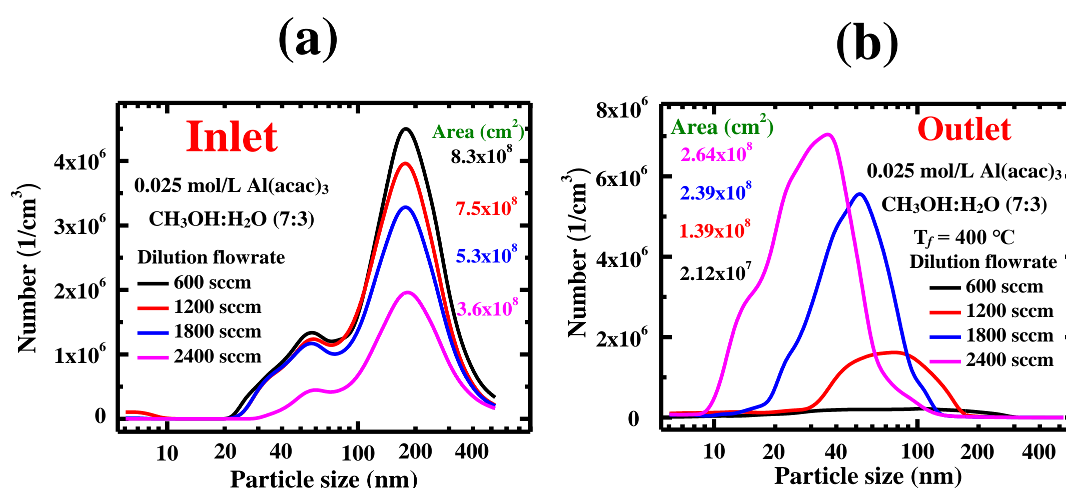

Figure 3.2. 6. Size distribution of $Al(acac)_3/CH_3OH/H_2O$ mist particle at the (a) inlet and (b) outlet of the tubular furnace, **A** and **B**, for different F_d values using a 0.025 mol/L $Al(acac)_3$ solution and a CH_3OH/H_2O mixture (7:3 volume ratio) at a T_f of 400 °C. The inset value is the integrated area of the total number density of mist for each deposition condition.

Figure 3.2.7(a) shows the size distribution of mist particle from $Al(acac)_3/CH_3OH/H_2O$ mist particles at the outlet **B** of the furnace for different values of T_f, the AlO_x thin films employed in the analysis were fabricated using a 0.025 mol/L $Al(acac)_3$ solution and CH_3OH/H_2O mixture (7:3), at an F_d of 2400 sccm. The size distribution of the mist particles was a maximum for mist particle sizes of 30- 40 nm at a T_f of 400 °C; it decreased to 20- 22 nm and had a narrow bandwidth when T_f was increased to 550 °C. Notably, the number density of the mist particles with an average size of 40- 100 nm was markedly suppressed because the overall number density decreased when T_f was increased from 400 to 550 °C. These results suggest that the mist precursor entering the furnace is efficiently consumed for the deposition of AlO_x thin films at higher T_f. Moreover, the film deposition rate increased from 1.9 to 5.4 nm/min and the surface roughness decreased when T_f was increased from 400 to 550 °C (**Figure 3.2.2**). Thus, the results imply that fine mist particles with an average size of ~20 nm and a narrow bandwidth are preferable for the uniform deposition of AlO_x thin films. Further, the results indicate that AlO_x thin films with less surface roughness and high *n*-value can be achieved by adjusting the T_f and F_d.

Figure 3.2.7(b) presents the size distribution of $Al(acac)_3/CH_3OH/H_2O$ mist particles at outlet **B** of the furnace for different values of V_m. The measurement was performed using the optimized parameters, i.e., 0.015 mol/L $Al(acac)_3$ solution, F_d of 2400 sccm, and T_f of 550 °C. When V_m was increased from 0 to 9 kV, the average size of the mist particle decreased from ~25 nm, having a broad bandwidth at ~30 to 18 nm with a narrower bandwidth at ~14 nm. Thus, the mist particles with larger sizes of 40 - 100 nm were suppressed by applying V_m.

The image obtained using a high-speed camera combined with Mie scattering using 633 nm and 338 nm laser diodes revealed that the average size of the mist particles was ~550 nm at inlet **A (Figure 3.2.7(c))**. Additionally, the image revealed a marked increase in the traveling speed of the mist particles at outlet **B** when V_m was applied

(**Figure 3.2.7(c)**). However, the contribution of the mist particles having sizes of several micrometers larger than that of the deposited film is still unclear. We believe that few negatively charged mist particles with an average size larger than ~550 nm was trapped at the front electrode. Untrapped mist particles passing through the electrode collided with each other because of their acceleration by the electric field, resulting in the generation of the fine particles.[3.24] We believe that few negatively charged mist particles larger than ~550 μm were trapped at the front electrode. Untrapped mist particles passing through the electrode collided with each other because of their acceleration by the electric field, resulting in the generation of fine particle (**Figure 3.2.7(c)**).[3.25]

Consequently, the film deposition rate decreased with a decrease in the surface roughness at *a* higher value of V_m. This phenomenon was observed because the fine mist particle generated by the primary reaction mainly contributes to the film deposition (**Figure 3.2.4(c)**). These results imply that the V_m supply during the film growth of AlO_x promotes the formation of fine particles; thus, improved rigidity and uniformity of the AlO_x network can be obtained.

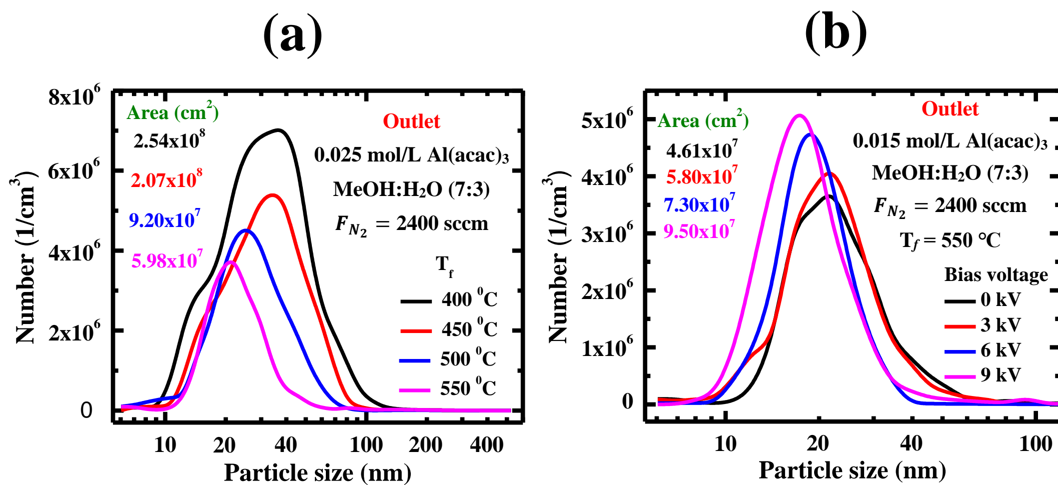

(c)

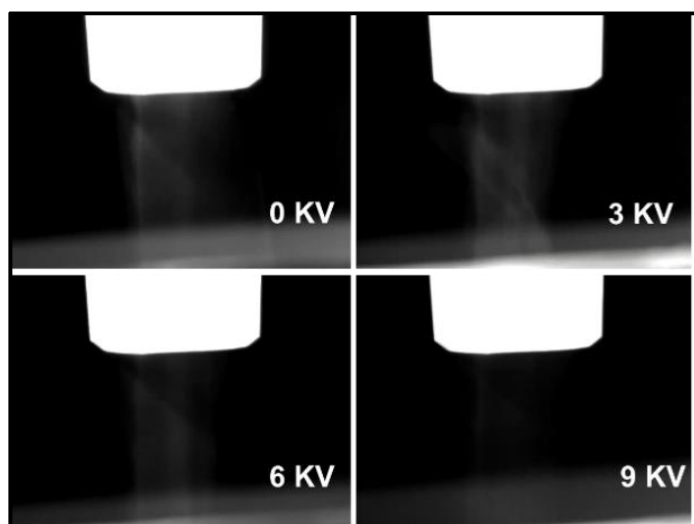

Figure 3.2. 7. Size distribution of $Al(acac)_3/CH_3OH/H_2O$ mist particles (CH_3OH/H_2O= 7:3) measured with different (a) T_f for 0.025 mol/L $Al(acac)_3$ and (b) V_m for 0.015 mol/L $Al(acac)_3$ at the outlet **B** of the tubular furnace for an F_d of 2400 sccm. (c) High-speed camera images at the inlet of the tubular furnace for different values of mesh bias V_m.

Figure 3.2.8(a) summarizes the correlation between the film deposition rate and the integrated area ratio of the size distribution of the mist particles at the outlet and inlet positions (A_{out}/A_{in} as 1-(A_{out}/A_{in})). The correlation is described for different values of F_d, T_f, and V_m, (**Figures 3.2.2–3.2.8**). Notably, a linear relationship between the film deposition rate and ratio 1-(A_{out}/A_{in}) is observed. The correlation between the n-value (at 3.5 eV) and the integrated area ratios of the size distribution of mist particles (at the main peak to the total area, A_M) at the outlet positions is shown in **Figure 3.2.8(b)**; the correlation is presented for different values of F_d, T_f, and V_m. The average particle size of the mist precursor at its highest number density is shown on the horizontal axis of the figure. The n-value of the AlO_x thin film increased with an increase in (A_M/A_{out}) × 100% for small mist particles having high number densities and small surface roughness values (**Figure 3.2.8(c)**). These results imply that the film deposition rate is determined by the ratio 1-(A_{out}/A_{in}). However, the morphology and rigidity of the AlO_x

film network are dominated by the size distribution of mist particles. Nonetheless, further studies on the contribution of the mist particles with larger sizes (of micrometer order) toward the film deposition are required.[3.24]

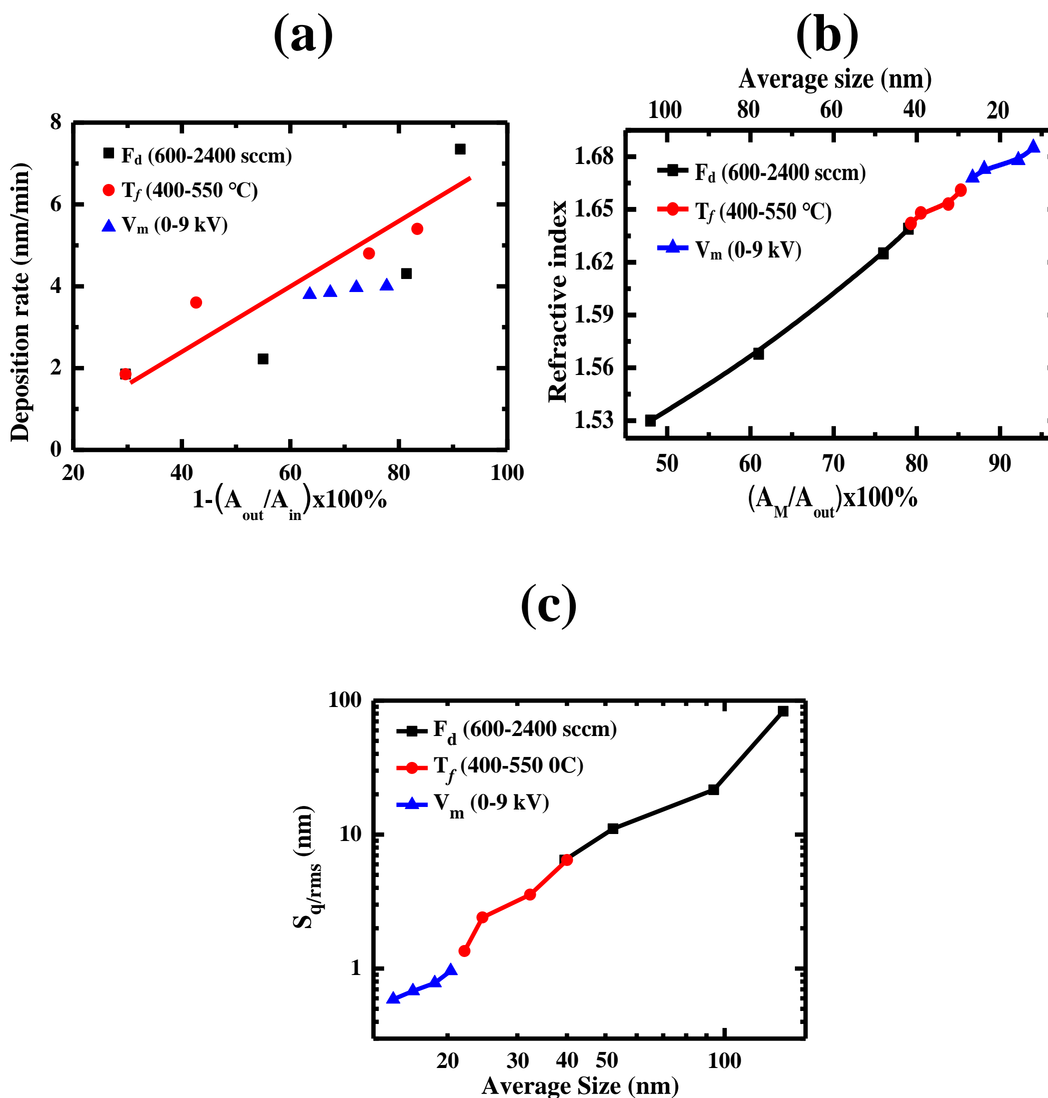

Figure 3.2. 8. (a) Deposition rate for AlO_x thin films by mist-CVD summarized as a function of the area ratio of 1-(A_{in}/A_{out}) for varied F_d, T_f, and V_m conditions (**Figures. 3.2.1-3.2.4**) obtained from the size distributions of mist precursor at the inlet and outlet positions (**Figures 3.2.6 and 3.2.7**). **(b)** Refractive index (n) vs (A_M/A_{out}) × 100% for varied F_d, T_f, and V_m. The average particle size of the mist precursor at its highest number density corresponding A_M is given on the horizontal axis. (c) $S_{q/rms}$ vs average size of mist precursor for varied F_d, T_f, and V_m.

3.2.4 Effect of V_m on the junction properties at the AlO_x/n+-Si interface and FET performance

Figure 3.2.9 shows the J-E curves obtained from AlO_x thin films with a thickness of 50 nm, fabricated using different V_m values. The inset shows a schematic representation of the MOS capacitor. The breakdown field shifted systematically from 6.8 MV/cm for the film grown without V_m to about ~8 MV/cm for the specimen with a V_m of 9 kV. This value is compatible with the breakdown field of over 8.5 MV/cm obtained through a plasma-enhanced ALD Al_2O_3/GaN/sapphire MOS-CAP structure reported previously.[3.26] Additionally, the leakage current was notably suppressed as the magnitude of V_m was increased. These results imply that a smooth and dense AlO_x network is crucial to obtaining high-performing AlO_x films to acts as gate insulators in FETs. In addition, the obtained AlO_x network can improve the passivation ability of c-Si for c-Si photovoltaics **(Figures 3.2.9 (b) and (c))** for the carrier lifetime and surface recombination velocity of the Al/AlO_x (thickness = 50 nm)/n^+-Si structure.[3.15-17]

(a)

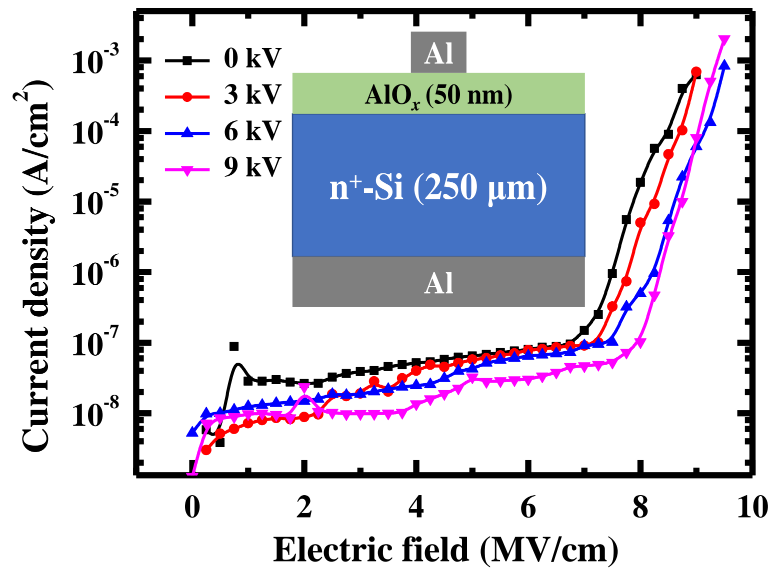

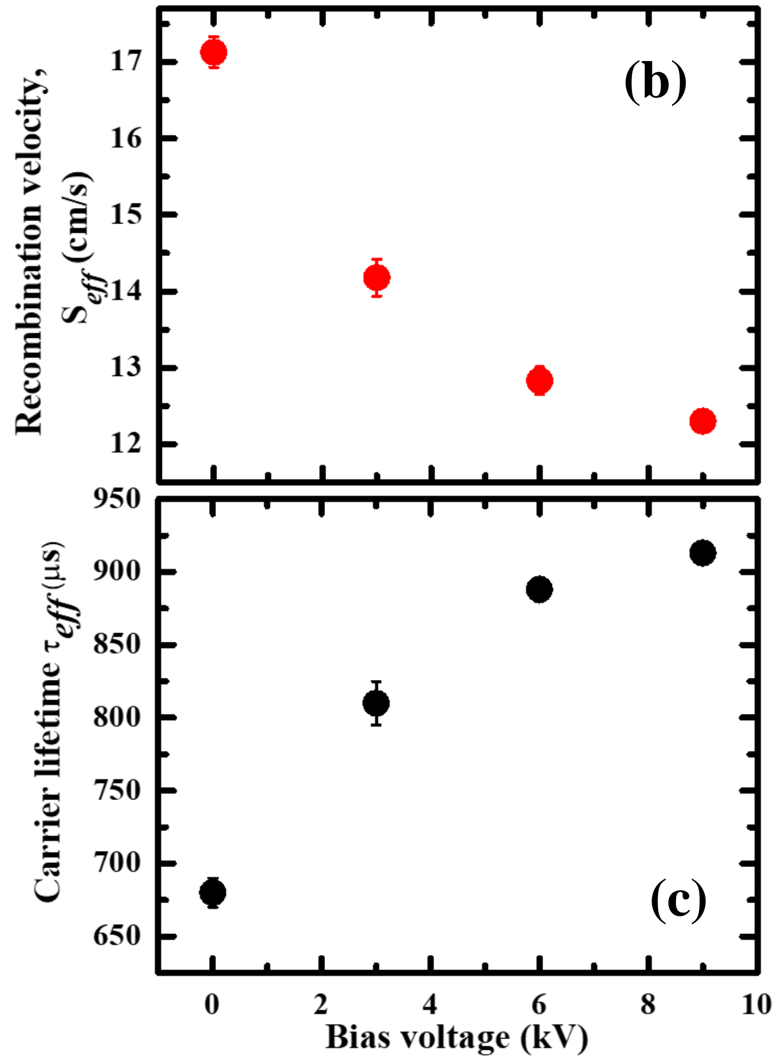

Figure 3.2. 9. (a) J-E curves in the Al/AlO_x/n^+-Si MOS capacitor with AlO_x grown by mist-CVD at different V_m values. (b) Recombination velocity S_{eff}, (c) Minority carrier lifetime τ_{eff} of AlO_x thin films fabricated using mist-CVD with different values of V_m.

Figure 3.2.10 shows the capacitance versus voltage C-V curves for both forward and backward scanning of the Al/AlO_x/n^+-Si MOS capacitors fabricated at different V_m values, whereas sampling voltage and sweep rate were 0.02V and 0.2V/s, respectively. The hysteresis of the C-V curve ΔV_{FB} associated with interface defect (D_{it}) at the dielectric/semiconductor interface was markedly suppressed; [3.27] a decrease from 0.056 V for the film fabricated without V_m to 0.005V for the specimen with a V_m of 9 kV was observed. D_{it} was determined from the *C*-V characteristics at different measurement frequencies, through the following equation (Equation 3.2.1).

$$D_{it}(\varphi_s) = \left(C_{ox}/q\right)\left(C_{hf}/(C_{ox} - C_{hf}) - C_{lf}/(C_{ox} - C_{hf})\right) \quad (cm^{-2}eV^{-1}) \quad (3.2.1)$$

where C_{lf} and C_{hf} are the capacitances measured at low (10 kHz) and high frequency (1MHz), respectively. D_{it} decreased from 4.56×10^{10} to 9.5×10^{9} $cm^{-2}eV^{-1}$ when V_m was increased from 0 to 9 kV (**Table 3.2.1**). The value of D_{it} at 9 kV was ~1×10^{10} $cm^{-2}eV^{-1}$, which was the same as those reported using radio frequency magnetron sputtering and PE-CVD.[3.15,3.16]

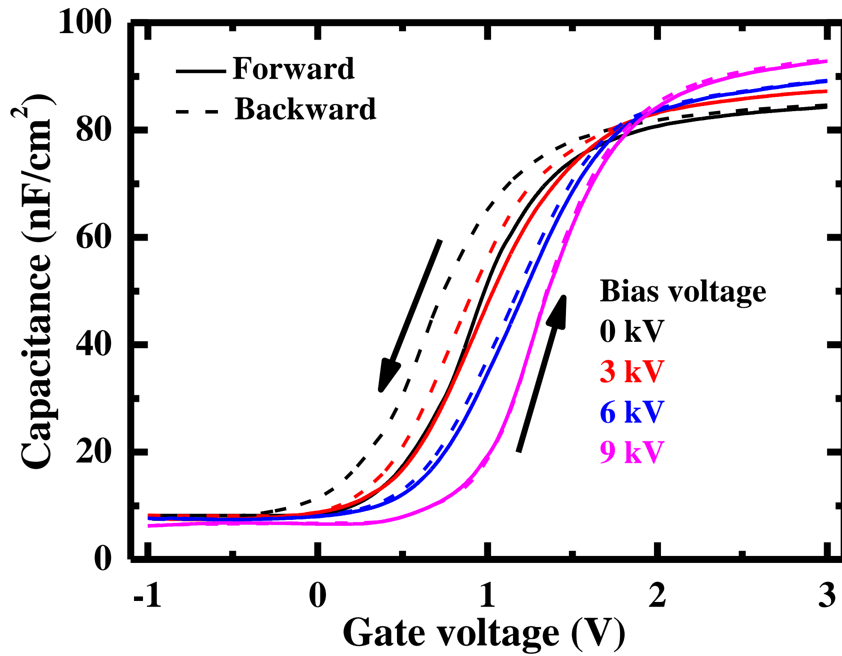

Figure 3.2.10. (a) Capacitance-voltage (C-V) hysteresis behavior of the AlO_x thin films fabricated through mist-CVD at different V_m for a measurement frequency of 1 MHz.

Table 3.2.1 summarizes the C -V hysteresis, flat band voltage (V_{FB}), negative fixed charge density (Q_f), and interface trap density (D_{it}) for the corresponding Al/AlO_x/n^+-Si capacitors, the capacitors analyzed had a thickness of ~50 -nm, and were fabricated using varied V_m. **Table 3.2.1** shows that V_{FB} increased from 0.73 to 1.18 V when V_m was increased from 0 to 9 kV, respectively. The lower V_{FB} value of the AlO_x thin film fabricated without V_m reveals that the native defects/traps in the sample are dominant, owing to oxygen vacancies. In contrast to the sample fabricated without V_m, the sample with V_m shows a positive shift in V_{FB}. Such a shift indicates that negative

fixed charges were accumulated in the oxide and/or at the AlO_x/c-Si interface.[3.28,3.29] Consequently, Q_f increased from -2.03 × 10^{12} cm^{-2} to -5.1 × 10^{12} cm^{-2}. This value is compatible with those reported for AlO_x using ALD.[3.30-32] In addition, high Q_f creates a strong depletion layer in the junction to protect unwanted recombination with the charge in the c-Si[3.30-33], higher relative dielectric constant K for a higher mesh bias voltage of 9 kV also supports to form strong depletion layer in the junction **(Figure 3.2.11)**. Also, μ-photoconductive decay (PCD) measurements revealed that the AlO_x thin films fabricated with a V_m of 9 kV exhibited a minority carrier lifetime of ~750 μs having a low recombination velocity (~12 cm/s) **(Figures 3.2.9 (b) and (c))**. These results imply that the mesh bias supply in the synthesis of AlO_x thin films improves the surface passivation ability of the Al_2O_3/c-Si interface.

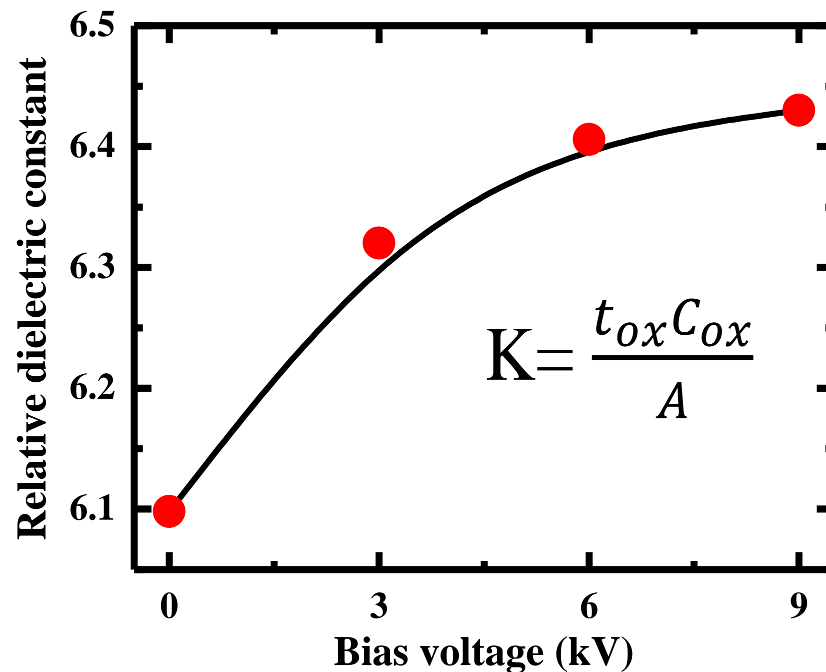

Figure 3.2. 11. Relative dielectric constant κ for AlO_x thin films with a thickness of 50 nm deposited under different values of V_m using mist-CVD on n-Si.

Table 3.2. 1. Extracted parameters for Al/AlO_x (thickness = ~50 nm)/n^+-Si capacitor fabricated at different V_m values.

V_m (kV)	C-V hysteresis (V)	V_{FB} from C-V (V)	Q_f ($\times 10^{12}$ cm^{-2})	D_{it} ($\times 10^{10}$ cm^2eV^{-1})
0	0.056 ± 0.001	0.73	2.03	4.56
3	0.028 ± 0.001	0.89	3.62	2.10
6	0.009 ± 0.001	1.11	4.98	1.02
9	0.005 ± 0.001	1.18	5.10	0.95

Figure 3.2.12(a) shows the schematic and optical microscope images of the MIS-FET device structure used in this study. **Figure 3.2.12 (b)** and **(c)** also show the transfer characteristics and $\sqrt{I_{SD}}$- V_g plots for the $MoSe_2$ layers (thickness of 40–60-nm) on a ~50 -nm -thick AlO_x/p^+-Si fabricated at different V_m values by mist-CVD. For each V_m values, the linear mobility (μ_{lin}), the saturation mobility (μ_{sat}), threshold voltage V_{th}, subthreshold swing factor (SS), and on/off ratio are listed in **Table 3.2.2**. The linear and saturation mobilities of the $MoSe_2$ FET were calculated using the equations $\mu_{lin} = (dI_{DS}/dV_{GS}) \times (L/(W \cdot C_i \cdot V_D))$ and $\mu_{sat} = (d\sqrt{I_{DS}}/dV_{GS})^2 \times (2L/W \cdot C_i)$, respectively,[3.34] where L is the channel length, W is the channel width, and C_i is the capacitance between the $MoSe_2$ channel and back gate, and V_D is the voltage drop through the channel. The off-current was suppressed to be low with increasing the on/off current ratio of ~10^7 with an increase of V_m from 0 to 9 kV. These results originate from a strong depletion layer was formed in the AlO_x/p^+-Si interfaces due to extra negative fixed charges (**Table 3.2.1**). The hysteresis behavior of I_{sd}-V_g for the FET curve was consistent with those of C-V for V_m of 0 and 9 kV (Figure 3.2.12 (d)). These findings suggest that the hysteresis of FETs originates from the junction property at the mist-CVD AlO_x gate insulator/p^+-Si interface dependent on V_m value. Additionally, V_{th} of the $MoSe_2$ shifted negatively by the effect of the V_m on the fabrication of AlO_x thin films that acts as a gate insulator (**Figure 3.2.12(c)**). $MoSe_2$ metal chalcogenide is a well-known two-dimensional atomic layer material, that provides a dangling-bond-free surface. Thus, the majority of the defects at the $MoSe_2$/AlO_x interface are determined by the defect at the AlO_x surface. A FET mobility of 41.4 cm^2/Vs was obtained with a V_{th} of 2.75 V, SS of 0.24 V/dec, and an on/off current ratio of ~10^7 for a ~50 nm thick AlO_x layer; the AlO_x layer

employed in the study was fabricated under similar to that of FET yielded using mechanically exfoliated MoS_2, $MoTe_2$, or $MoSe_2$ on thermally grown SiO_2/p^+-Si.[3.35-38]

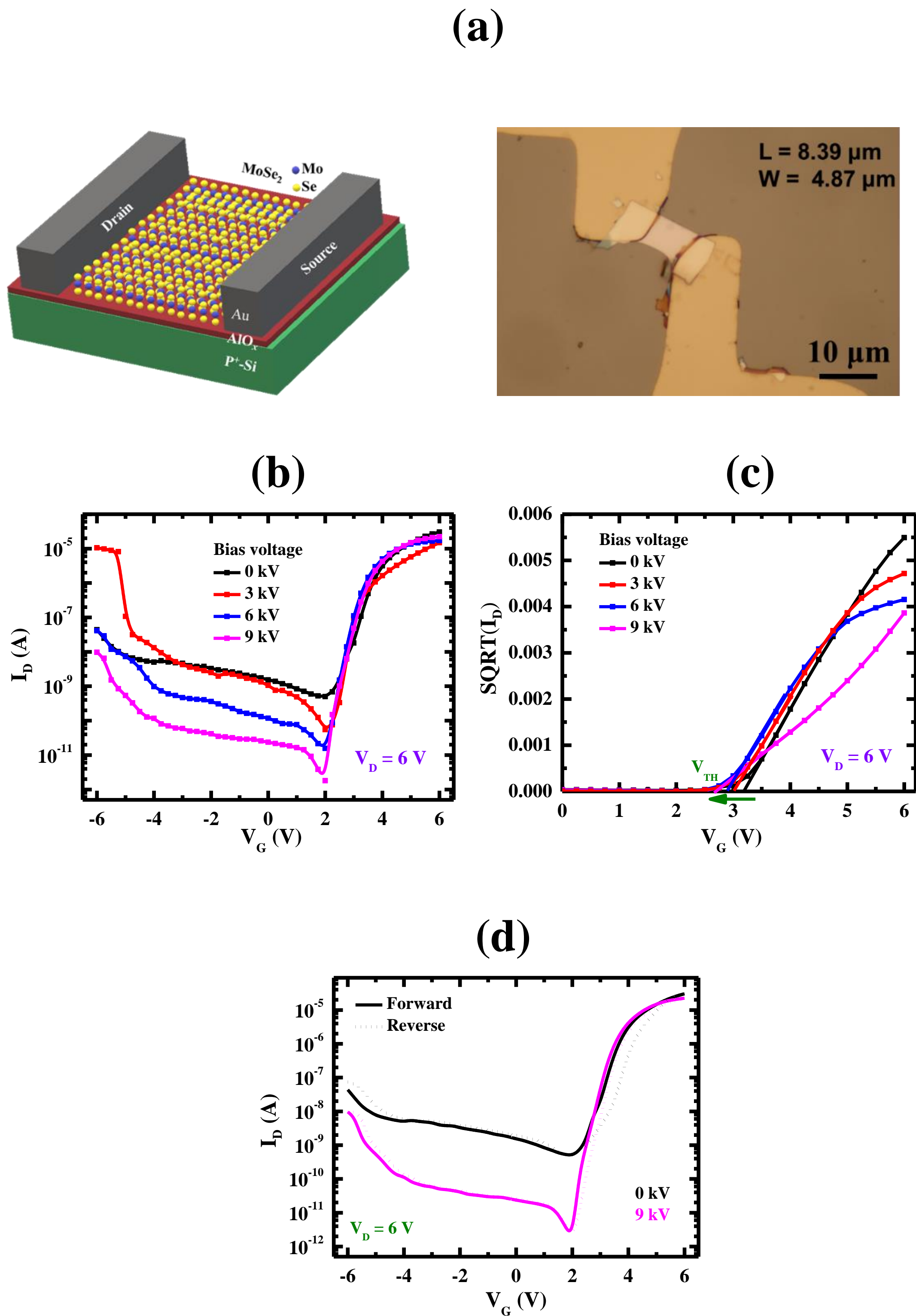

Figure 3.2. 12. (a) Optical image and schematic of the device structure of corresponding FETs. The channel length and width are 8.39 μm and 4.87 μm,

respectively. (b) Transfer characteristics of the $MoSe_2$ based FET, (c) √I_SD- Vg plots where AlO_x is used as a gate insulator fabricated at different Vm values. (d) Transfer characteristics of the $MoSe_2$ based FET hysteresis behavior; AlO_x thin films were fabricated by mist-CVD at different V_m.

3.3 Synthesis of mist chemical vapor deposited $Al_{1-x}Ti_xO_y$ thin films and their application to a high dielectric material

The large bandgap dielectric material is essential to suppress the charge injection from electrodes into dielectrics that cause leakage current. On the other side, the dielectric material with a high dielectric constant is important to scall down the device size. The trade-off between these two properties is clearly noticed. One effective proposal for balancing between κ and E_g is employing aluminum titanium oxide $[(Al_2O_3)_{1-x}TiO_2)_x]$ ($Al_{1-x}Ti_xO_y$) with intermediate properties of Al_2O_3(κ ~9, E_g~ 7 eV) and TiO_2(κ ~50, E_g ~3 eV). As a third topics, we investigated the synthesis of $Al_{1-x}Ti_xO_y$ alloy thin films by mist-CVD from $Al(acac)_3$ and $Ti(acac)_4$ for different precursor mixing ratios γ [=$Ti(acac)_4/Al(acac)_3$] and CH_3OH/H_2O solvent ratios. The junction properties at the corresponding $Al_{1-x}Ti_xO_y$/n-Si interface and examining the potential of $Al_{1-x}Ti_xO_y$ obtained through mist-CVD to act as a high dielectric gate material for metal-oxide field-effect transistors (MIS-FETs) are also investigated by using mechanically exfoliated molybdenum di-selenide ($MoSe_2$) and Arsenic (As)-doped tungsten di-selenide (WSe_2) flakes as an active layer including the assembly of the complementary metal-oxide-semiconductor (C-MOS) inverter.

3.3.1 Synthesis of $Al_{1-x}Ti_xO_y$ thin films by mist-CVD

Figure 3.3.1 shows the Ti composition ratio x in the $Al_{1-x}Ti_xO_y$ films determined by the XPS analysis plotted as a function of $Al(acac)_3$ and $Ti(acac)_4$ precursor mixing ratio γ for different CH_3OH/H_2O solvent ratios at an F_d of 2400 sccm and a T_f of 550 °C. The Ti composition ratio x in the $Al_{1-x}Ti_xO_y$ films depends on γ as well as CH_3OH/H_2O solvent ratio. The linear relation between the x in the $Al_{1-x}Ti_xO_y$ films and the γ value is observed when a CH_3OH/H_2O was 9:1, suggesting that the x ratio in the films can be controlled by tuning the γ as well as CH_3OH/H_2O mixing ratio in the

solution. Thus, the Ti composition ratio x is also sensitive to the CH_3OH/H_2O ratio even at the identical γ ratio.

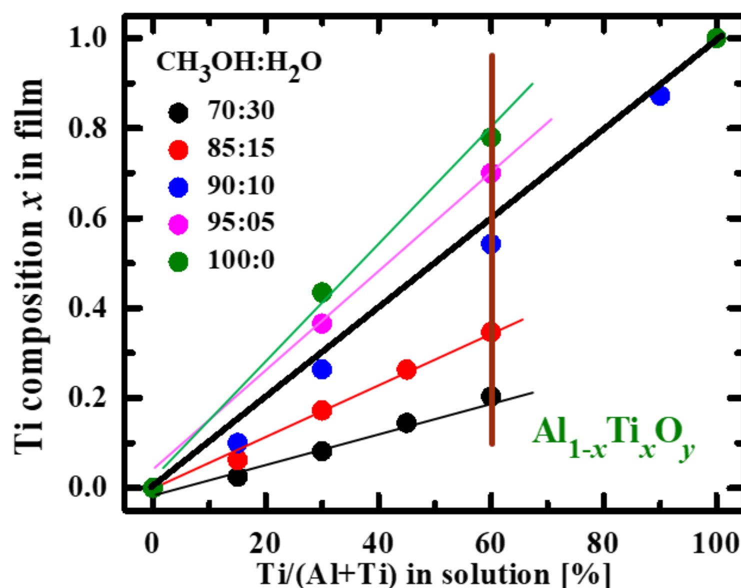

Figure 3.3. 1. Ti composition ratio x in the $Al_{1-x}Ti_xO_y$ films plotted as a function of ratio γ for different CH_3OH/H_2O solvent mixing ratios.

Figure 3.3.2 (a) shows the film deposition rate of the $Al_{1-x}Ti_xO_y$ plotted as a function of CH_3OH/H_2O volume ratios for a γ value of 70/30. The film deposition rate decreased markedly from 10.5 to 0.9 nm/min when the H_2O mixing ratio was increased from 0 to 30 volume percent in CH_3OH solution. In fact, little has been discussed about a discrepancy between the mixing ratio in the solute in a solution and the composition ratio in the mist-CVD alloy thin films. These results imply that the H_2O addition reduces the film growth rate of $Al_{1-x}Ti_xO_y$ because the generation rates for both $Al(acac)_3$ and $Ti(acac)_4$ precursors are suppressed to be lower than those of CH_3OH alone. In fact, the high-speed camera also reveals that the mist flux and their traveling speed decreased by the addition of H_2O (**Figure 3.3.2 (b)**).

(a)

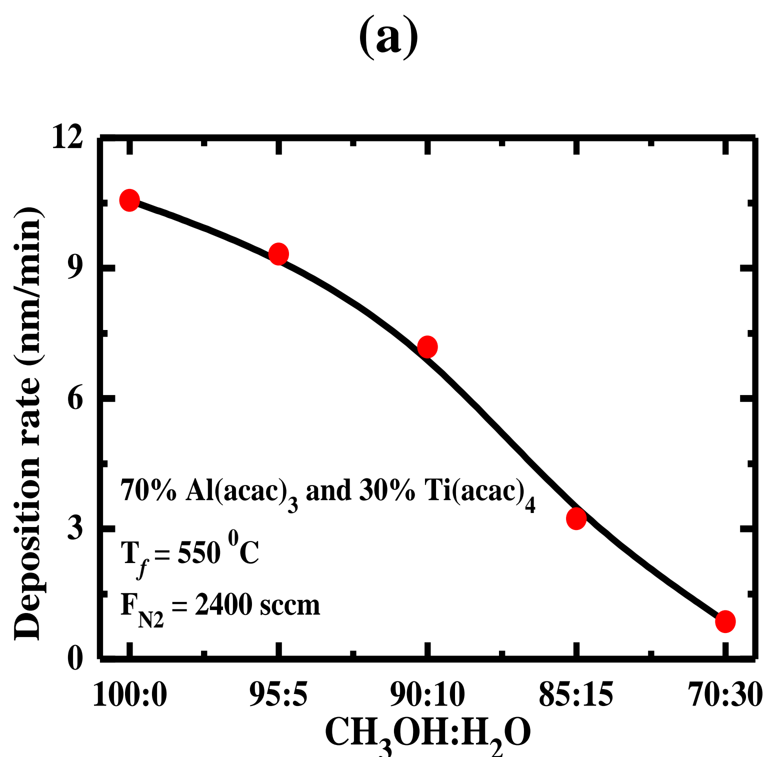

(b)

Ti(acac)4
Al(acac)3
CH3OH:H2O (10:0)

Ti(acac)4
Al(acac)3
CH3OH:H2O (7:3)

Figure 3.3. 2. (a) Deposition rate for $Al_{1-x}Ti_xO_y$ thin films fabricated by mist-CVD plotted against different CH_3OH/H_2O solvent ratios for a γ of 70/30, an F_d of 2400 sccm, and a T_f of 550 °C. (b) High-speed camera image of $Al(acac)_3/Ti(acac)_4$ mist precursors with different CH_3OH/H_2O ratios monitored at the outlet position of the tabular furnace.

In **Figure 3.3.3 (a)**, the size distribution of mist particles monitored at the outlet position of the tubular furnace (**Figure 3.3.3 (b)**) is shown for different CH_3OH/H_2O ratios at a γ of 70/30. The size distribution of the mist particles composed of two broad

bands having a maximum at ~10 and ~25 nm, which are attributed to TiO_x and AlO_x related complex, respectively, considering the origin according to the results of the previous study of size distributions of solely $Al(acac)_3$ and $Ti(acac)_4$ mist particles (**Figure 3.3.3 (c)**). The total number density of mist particles also decreased gradually with increasing the H_2O ratio to 15% and subsequently it decreased markedly when the H_2O ratio was above 15%. These findings originate from the suppression of the mist generation rate due to hydrogenation by a stronger hydrogen bond between H_2O and CH_3OH, which results in the increase in the surface tension and chemical stability of the CH_3OH-H_2O complex in the solution.[3.12,3.13,3.39] On the other hand, it is well known that the H_2O and CH_3OH domain exists in a separate state for CH_3OH/H_2O volume ratio over ~20%.[3.12]

(a)

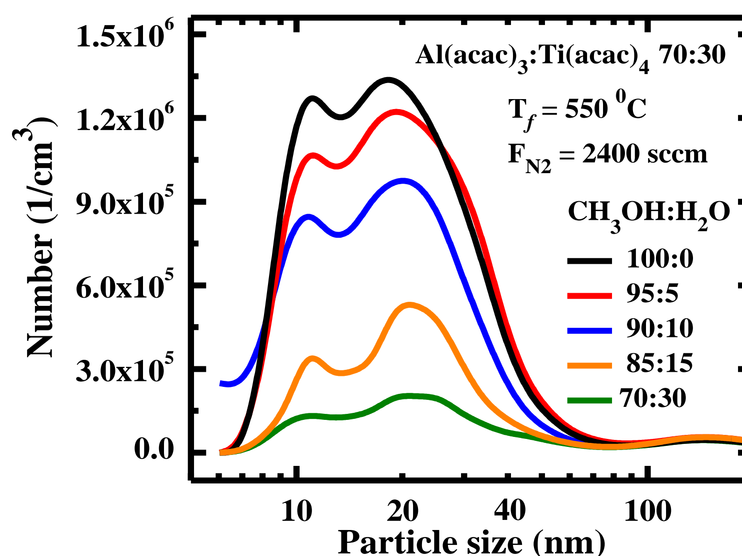

(b)

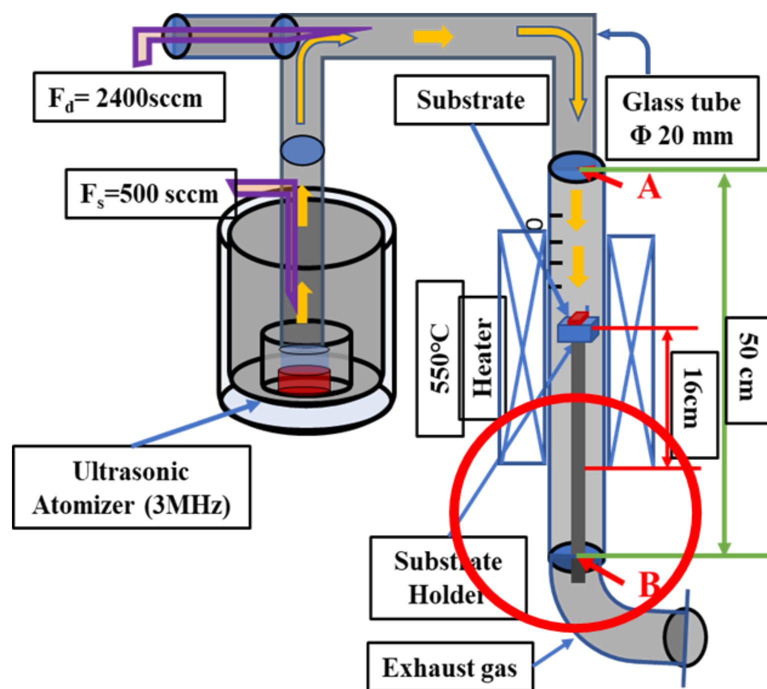

(c)

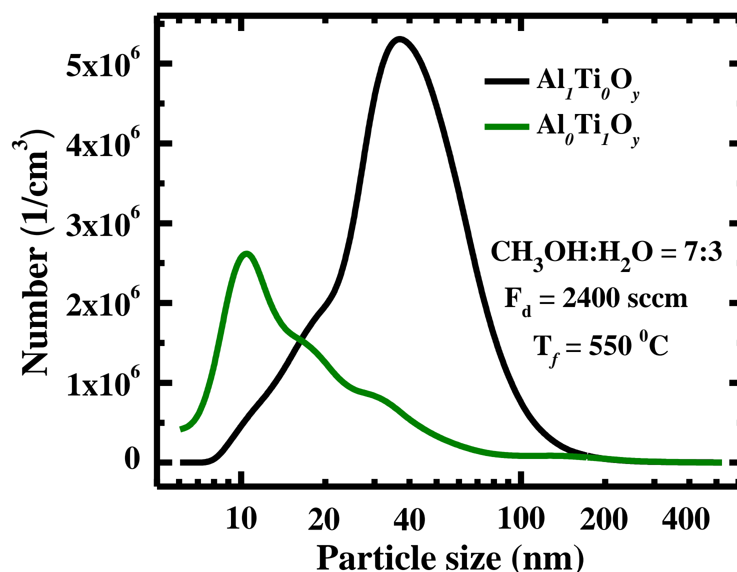

Figure 3.3. 3. (a) Size distribution of Al(acac)$_3$/Ti(acac)$_4$ composite mist particle for an γ ratio of 70/30 mist particles for different CH_3OH/H_2O solvent ratios monitored at the outlet position of the tabular furnace., (b) Arrangement of mist-CVD system for the monitoring of mist droplets size by particle counter at the outlet position B at the tabular furnace. *(c)* Size distribution of solely Al(acac)$_3$/Ti(acac)$_4$ mist particles monitored at the outlet position of the tabular furnace for CH_3OH/H_2O of 70/30, an F_d of 2400 sccm, and a T_f of 550 °C.

Figure 3.3.4 shows the AFM image of 40- nm- thick $Al_{1-x}Ti_xO_y$ films for different γ ratios when a CH_3OH/H_2O ratio was 90/10 and a T_f of 550 °C. RMS value in the 3 × 3 μm^2 areas was decreased from 0.96 to 0.69 nm with an increase in x value from 0 to 0.54 in the $Al_{1-x}Ti_xO_y$ thin films. These results may originate from the increased number density of fine mist particles of TiO_x compared to the AlO_x.

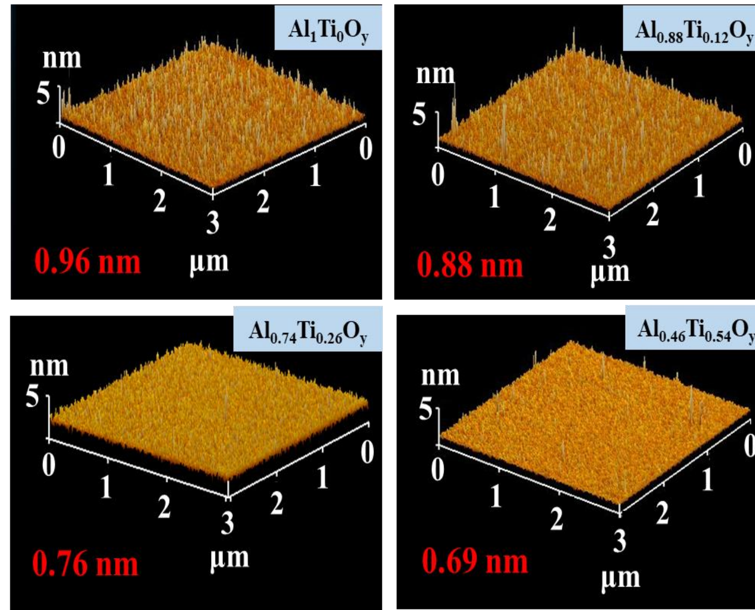

Figure 3.3. 4. AFM image of the corresponding ~40-nm- thick $Al_{1-x}Ti_xO_y$ thin films synthesized for different γ values at a CH_3OH/H_2O ratio of 90/10 where a linear relation between γ and x was observed.

3.3.2 Junction property at the $Al_{1-x}Ti_xO_y$/n-Si interface

Figure 3.3.5 (a) shows the C-V curve for Al/$Al_{1-x}Ti_xO_y$/n-Si MOS diodes for different x values and a CH_3OH/H_2O ratio of 9:1 measured at a sweep rate of 0.2 V/s for a step size of 0.02 V. The inset shows the schematic of the MOS capacitor. The saturated capacitance per unit area in the accumulation region increased from 95 to 207 $\mu F/cm^2$ when x increased from 0 to 0.54. This result originates from the increased capacitance owing to the stronger polarizability of TiO_2. **Figure 3.3.5 (b)** shows the flat band voltage for different x values of $Al_{1-x}Ti_xO_y$ thin films. V_{FB} is extracted from the

intersection of the extrapolation of the linear region of $(\frac{C_{ox}}{C_{MOS}})^2 - 1$ to the V_G-axis using the following equation.

$$(\frac{C_{ox}}{C_{MOS}})^2 - 1 = \frac{2C_{ox}^2}{qN_D\varepsilon_S\varepsilon_0}(V_G - V_{FB}), \qquad (3.3.1)$$

The flat band voltage V_{FB} decreased from 1.76 to 0.61 V with the increase of x values in the $Al_{1-x}Ti_xO_y$ thin film, suggesting the smaller number of traps at the interface **Figure 3.3.5 (b)**.[3.40]

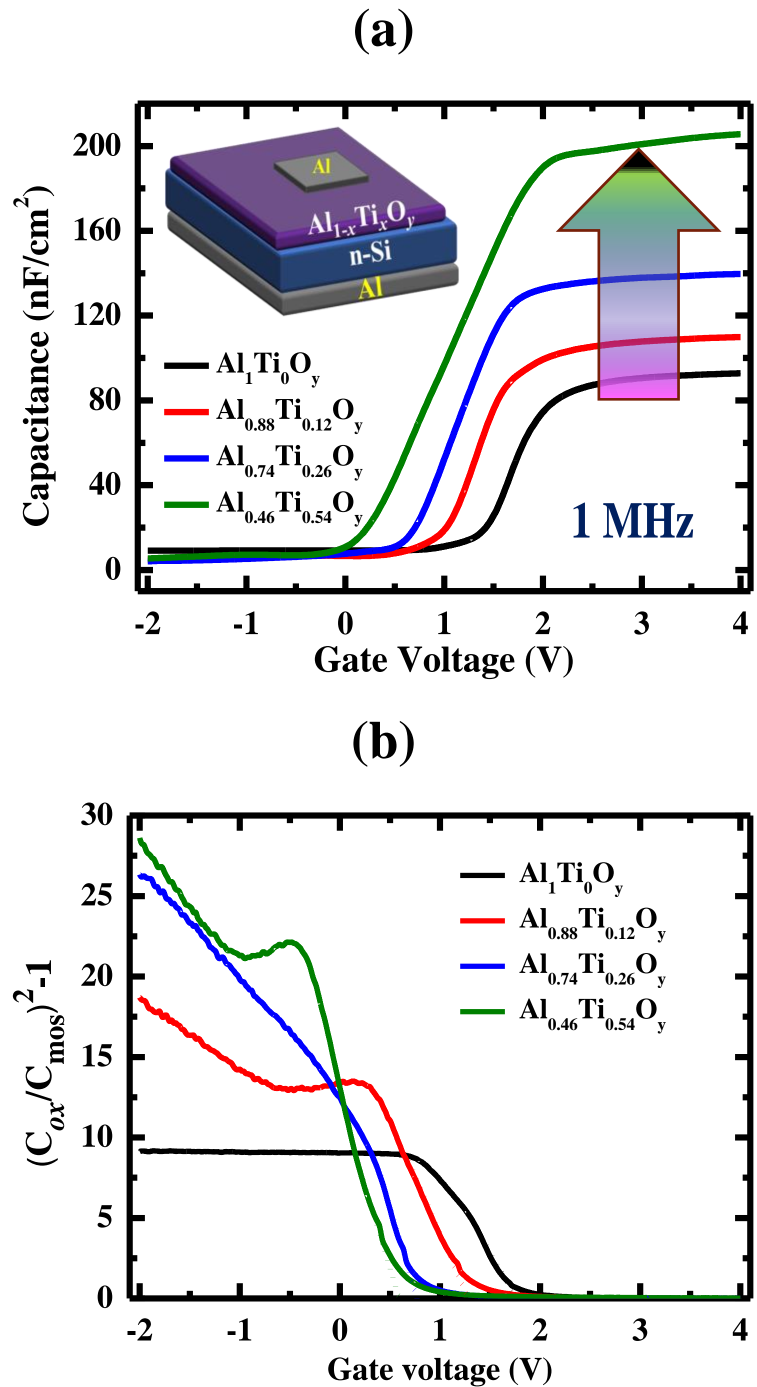

Figure 3.3. 5. (a) Capacitance-voltage curve with a schematic representation in the inset of the $Al/Al_{1-x}Ti_xO_y/n^+$-Si MIS capacitors fabricated at different *x* values for a measurement frequency of 1 MHz. (b) $(C_{ox}/C_{MOS})^2$-1 vs gate voltage curve to determine flat band voltage V_{FB} for $Al_{1-x}Ti_xO_y$ thin films with a thickness of 40 nm deposited under different values of *x*.

Figure 3.3.6 shows the interface state density D_{it} plotted as a function of *x* in the $Al_{1-x}Ti_xO_y$ thin films. D_{it} was determined from the C-V characteristics using the following equation (Eq. 1)

$$D_{it}(\varphi_s) = \left({C_{ox}}/{q}\right)\left({C_{hf}}/{(C_{ox} - C_{hf})} - {C_{lf}}/{(C_{ox} - C_{hf})}\right) \quad (cm^{-2}eV^{-1}) \quad (1)$$

where C_{lf} and C_{hf} are the capacitances measured at low (10 kHz) and high frequency (1 MHz), respectively. It is observed in **Figure 3.3.6** that D_{it} decreased from 4.56×10^{10} to 1.23×10^{10} $cm^{-2}eV^{-1}$ when *x* increased from 0 to 0.54.

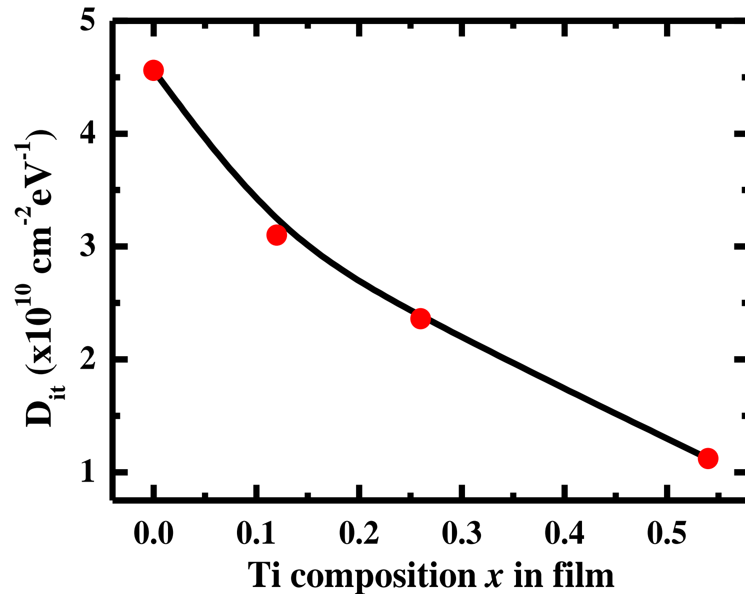

Figure 3.3. 6. Interface state density D_{it} as a function of x in the $Al_{1-x}Ti_xO_y$ thin films.

Figure 3.3.7 (a) displays the XPS spectra of the O(1s) core energy level region for 50-nm- thick $Al_{1-x}Ti_xO_y$ thin films with different *x* values. The broad peaks attributed to the two components at 529.5 ± 0.5 eV (well-bonded oxygen) and 531 ± 0.5 eV (the oxygen atom which is associated with lattice defects such as oxygen and

metal vacancies, and/or interstitials adjacent to the oxygen), their illustrations are shown in **Figure 3.3.7 (b) and (c)**.[3.41-45] The mist-CVD amorphous AlO_x thin films contain the lattice defects and hydrolysis due to their weak bonding to oxygen.[8] However, when the weakly bonded oxygen was replaced by strongly bonded oxygen upon the addition of a Ti cation, an oxide frame with fewer lattice defects and hydroxides was generated. These results imply that the well-bonded oxides increase with x in the $Al_{1-x}Ti_xO_y$ thin films, due to the decrease in lattice defects originated from oxygen vacancies. The XPS results also revealed that the incorporation of titanium ions facilitates the oxide lattice formation in the $Al_{1-x}Ti_xO_y$ thin-film, which leads to a decrease in the donor density at the $Al_{1-x}Ti_xO_y$/n-Si interface. This is because the bonding energy of O-Ti (666.5± 5.6 kJ/mol) is higher than that of O-Al (501.9± 10.6 kJ/mol).[3.46,3.47]

(a)

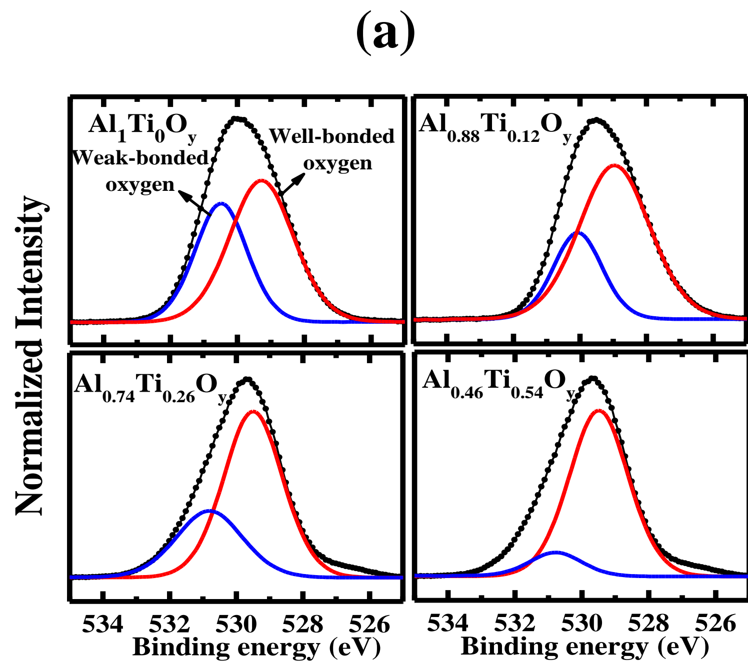

(b) **(c)**

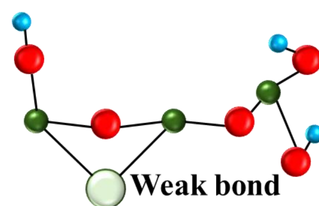

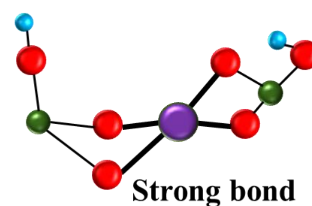

Figure 3.3. 7. (a) XPS spectra of O(1s) core energy level region for $Al_{1-x}Ti_xO_y$ thin films for different x values. Schematic showing the conceptual structural features of (b) AlO_x and (c) $Al_{1-x}Ti_xO_y$.

The conduction band offset, ϕ_{CBO}, at the $Al_{1-x}Ti_xO_y$/n-Si interface is extracted by C-V measurement using the following equation:

$$\phi_{CBO} = qV_{bi} + \frac{KT}{q} - \Delta\phi_B \quad (1)$$

$$\Delta\phi_B = \left(\frac{qE_m}{4\pi\varepsilon_{si}\varepsilon_0}\right)^{1/2} \quad (2)$$

where V_{bi} is the built-in potential at zero bias which is determined from the extrapolation value on the C^{-2}-V plot (Figure S7), K is the Boltzmann constant, T is the tabular furnace temperature of 550 °C, q is the charge, $\Delta\phi_B$ is the image force barrier lowering [Eq. (1)], and E_m is the maximum electric field. The values obtained for each term in Eq. (1) at different x values in the $Al_{1-x}Ti_xO_y$ thin films are presented in Table I. Here, KT_f/q is 0.063 eV at a 550 °C and $\Delta\phi_B$ is 20 meV (Eq. 2). As shown in Table 1, the conduction band offset at zero bias decreased systematically from 1.75 to 0.38 eV when the x value increased from 0 to 0.63 in the $Al_{1-x}Ti_xO_y$ thin films.

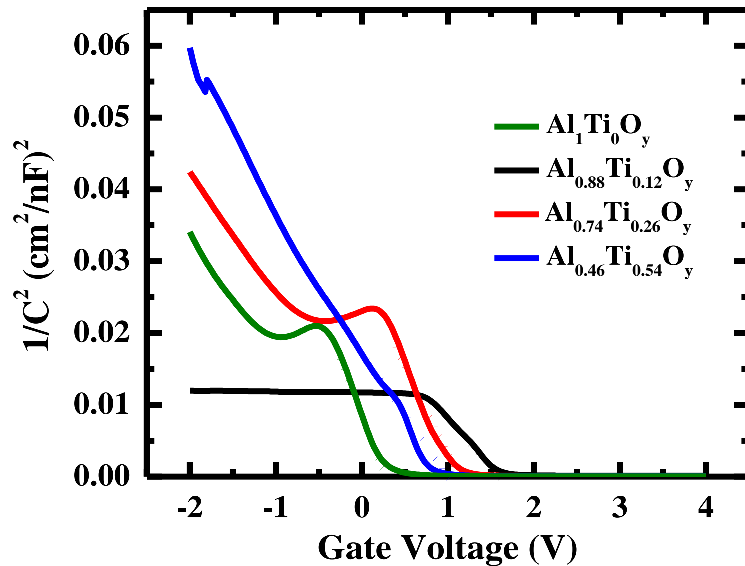

Figure 3.3. 8. C^{-2}-V plot for different x values in $Al_{1-x}Ti_xO_y$ thin films to determine built-in potential.

Table 3.3. 1 Extracted parameters to utilize conduction band offset at the $Al_{1-x}Ti_xO_y$/n-Si interface as determined from C-V characteristics for different x values.

Alloy composition	qV_{bi} (eV)	ϕ_{CBO} (eV)
$Al_1Ti_0O_y$	1.69	1.75
$Al_{0.88}Ti_{0.12}O_y$	1.16	1.22
$Al_{0.74}Ti_{0.26}O_y$	0.98	1.06
$Al_{0.46}Ti_{0.54}O_y$	0.31	0.38

Figure 3.3.9 (a) provides the κ value and the bandgap energy E_g plotted as a function of x in the $Al_{1-x}Ti_xO_y$ thin films. The κ value was calculated using: $\kappa = C_{ox}d/\varepsilon_0A$, where C_{ox} is the accumulation capacitance, d is the thickness of the $Al_{1-x}Ti_xO_y$ layer, ε_0 is the permittivity of free space, and A is the area. The bandgap energy of the $Al_{1-x}Ti_xO_y$ thin films was determined from the XPS O(1s) core energy level through spectral analysis. The energy band diagram at the accumulation region of $Al_{1-x}Ti_xO_y$ thin films for different x values are schematized in **Figure 3.3.9 (b)**. The equivalent oxide thickness (EOT) was determined using: $EOT = \frac{\kappa(SiO_2)}{\kappa(Al_{1-x}Ti_xO_y)} d\left(Al_{1-x}Ti_xO_y\right) + d(SiO_2)$, where $\kappa(SiO_2)$ and $\kappa(Al_{1-x}Ti_xO_y)$ are the dielectric constants and $d(SiO_2)$ and $d(Al_{1-x}Ti_xO_y)$ are the film thickness, and conduction band offset were extracted from C-V analysis. The κ value increased systematically from 6.23 to 25.12. As a result, the EOT decrease from 30.4 nm to 7 nm, when x increased from 0 to 0.54. The dielectric constants for different x values are compatible with those reported elsewhere.[18,19] This result originates from the decrease in the donor density at the $Al_{1-x}Ti_xO_y$/n-Si interface, which may originate from the decrease in the oxygen vacancy-related defects. This is because the bonding energy of O-Ti (666.5±5.6 kJ/mol) is higher than that of O-Al

(501.9±10.6 kJ/mol). On the other hand, the electronic bandgap E_g corresponding to their conduction band offset is systematically decreased from 6.45 eV to 4.25 eV and 1.75 eV to 0.38 eV, respectively with the increase of x value, which is a major cause of leakage current. As a result, $Al_{1-x}Ti_xO_y$ thin films with a higher k value of 13.8 and lower leakage current were obtained by adjusting a Ti composition ratio of 0.26.

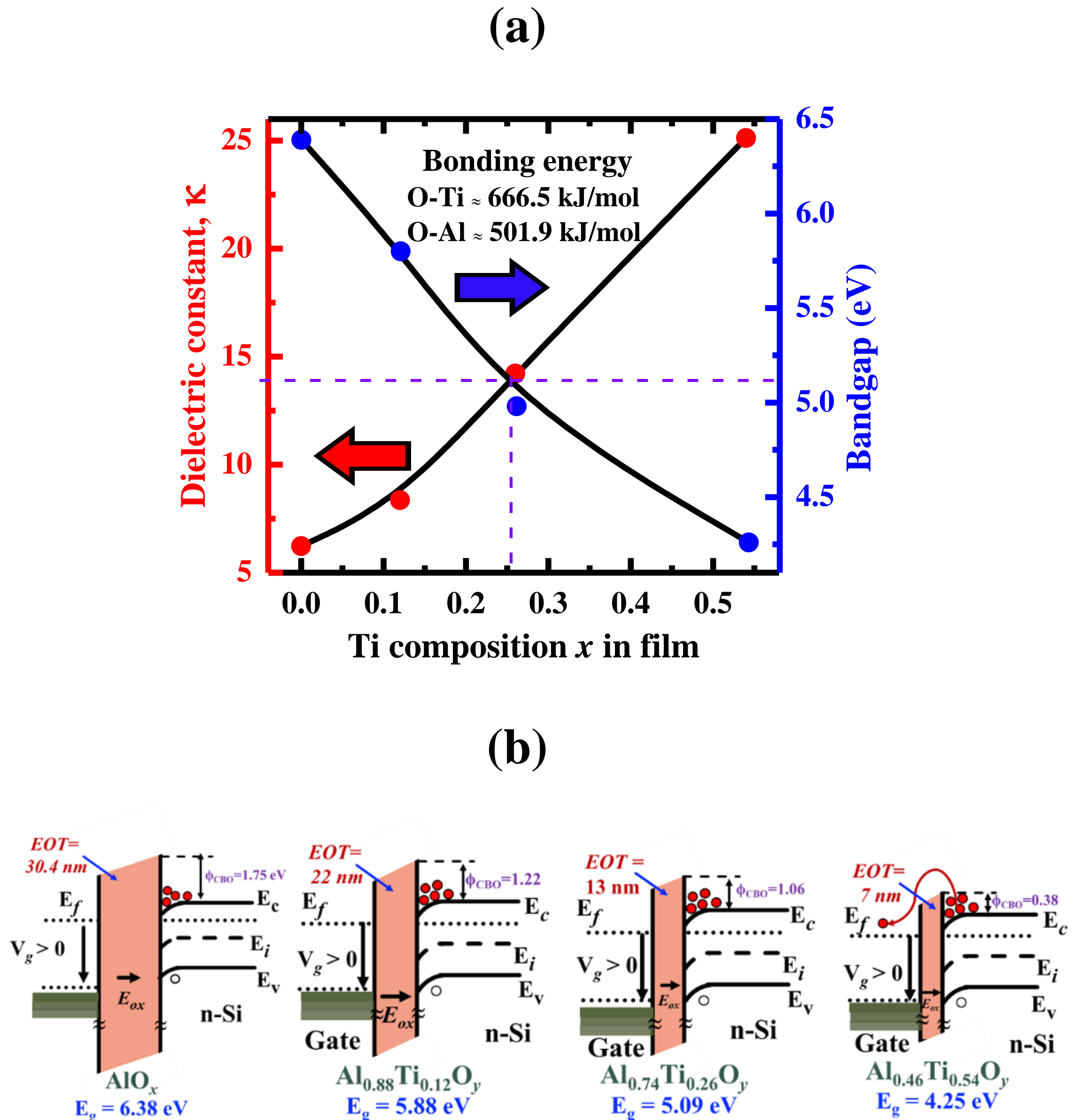

Figure 3.3. 9. (a) Dielectric constant, κ, and electronic bandgap E_g plotted as a function of x. (b) Energy band diagram of $Al_{1-x}Ti_xO_y$ thin films as a function of Ti compositions ratio x.

3.3.3 $Al_{1-x}Ti_xO_y$ as a gate insulator layer for MIS-FETs

Figure 3.3.10 (a) shows the transfer characteristics of MIS-FETs with the mechanically exfoliated $MoSe_2$ flakes of approximately 40 nm thickness on $Al_{1-x}Ti_xO_y$/p^+-Si with different *x* values. TMDC $MoSe_2$ is a two-dimensional (2D) layered material, composed of covalent bonds in the layer and van der Waals forces between the layers. The schematic and optical microscopic images of the MIS-FET device structure are shown **Figure 3.3.10 (b)**. The result for the FET with AlO_x alone as a gate dielectric layer is also included for comparison. The linear mobility (μ_{lin}), saturation mobility (μ_{sat}), threshold voltage V_{th}, subthreshold swing factor, SS, and on/off ratio with their corresponding $Al_{1-x}Ti_xO_y$ thin film thicknesses are listed in **Table 3.3.2**. The linear and saturation mobilities of the $MoSe_2$ FETs were calculated using the equations $\mu_{lin} = (dI_{DS}/dV_{GS}) \times (L/(W{\cdot}C_i{\cdot}V_D))$[3.34] and $\mu_{sat} = (d\sqrt{I_{DS}}/dV_G)^2 \times (2L/W{\cdot}C_i)$[3.34], where L is the channel length, W is the channel width, C_i is the capacitance between the $MoSe_2$ channel and the back gate, and V_D is the voltage drop through the channel. The linear (saturated) FET mobility was increased from 41.4 (137) to 85 (195) $cm^2/(V{\cdot}s)$ with a lower V_{th} shift from 2.75 to 0.92 V, a subthreshold swing SS of 0.24 to 0.12 V/dec, and an on/off current ratio of $\sim10^5$ to $\sim10^6$ for the $Al_{0.74}Ti_{0.26}O_y$ layer despite a relatively lower thickness of 39 nm. These values are almost compatible with the values obtained from the atomic-layer-deposited and sputtered $Al_{1-x}Ti_xO_y$ dielectric layers.[3.35-38]However, the off-current level in the reverse V_g region was increased at a higher TiO_2 composition of $x = 0.54$, which is determined by the balance between the conduction band offset and dielectric constant of the $Al_{1-x}Ti_xO_y$ layer and/or insufficient passivation quality of p^+-Si. The insertion of a chemically inert layer such as SiO_2, boron nitride, and TiO_2 at the $Al_{1-x}Ti_xO_y$ layer in the gate stack will further effectively passivate the conductance as well as offer strong permanent polarization for electronic synapse applications.

(a)

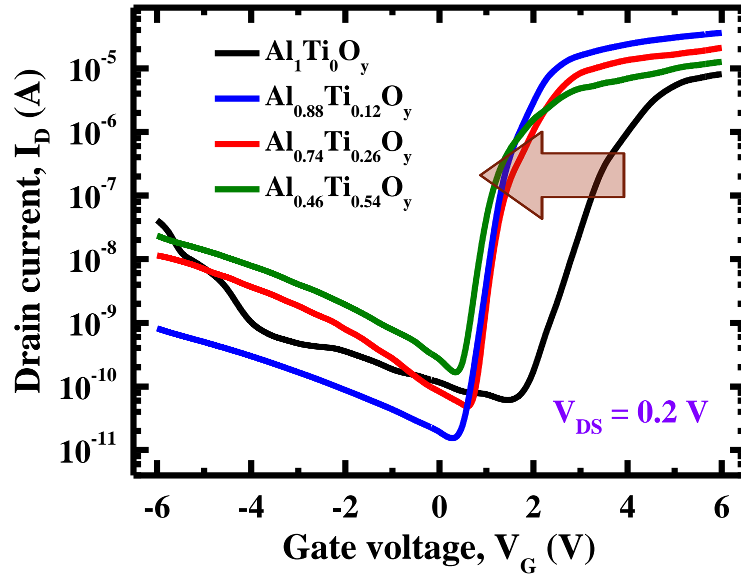

(b)

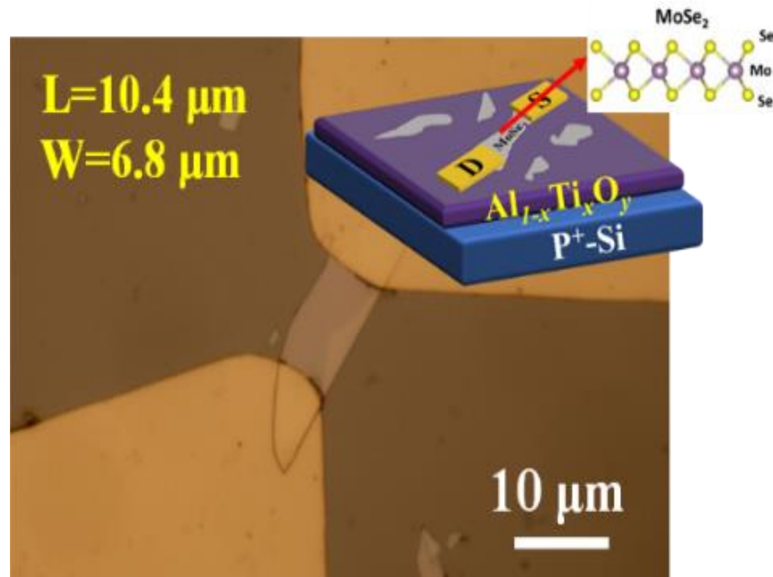

Figure 3.3. 10. (a) Transfer characteristics of the $MoSe_2$-based FETs where $Al_{1-x}Ti_xO_y$ is used as a gate dielectric layer for different x values at a V_{DS} of 0.2 V. (b) Optical image and schematic of the device structure of corresponding FETs. The channel length and width are 10.4 and 6.8 μm, respectively.

Table 3.3. 2 Electrical characteristics of $MoSe_2$-based n-channel MIS-FETs with $Al_{1-x}Ti_xO_y$ for different x values.

Alloy composition	Film thickness (nm)	V_{th} (V)	SS (V/dec)	I_{ON}/I_{OFF}	μ ($cm^2V^{-1}s^{-1}$)
$Al_1Ti_0O_y$	50.52	2.75	0.34	1.20×10^5	μ_{sat} =137.90 μ_{lin} =41.4
$Al_{0.88}Ti_{0.12}O_y$	39.38	1.13	0.16	6.52×10^5	μ_{sat} =181.30 μ_{lin} =72.37
$Al_{0.74}Ti_{0.26}O_y$	38.69	0.92	0.12	2.46×10^6	μ_{sat} =195.32 μ_{lin} =85.25
$Al_{0.46}Ti_{0.54}O_y$	40.96	0.53	0.28	9.79×10^4	μ_{sat} =162.31 μ_{lin} =47.30

Figure 3.3.11 (a) shows the crystal structure of the hexagonal-shaped As-doped WSe_2 layer, where the stacking layers follow the sequence of Se-W-Se. Each layer has a thickness of 0.34 nm. The atomic and covalent radius of W, As, and Se atoms are summarized in **Table 3.3.3**. For either atomic or covalent radius, it is noticed that there is a much smaller size mismatch when As is substitutionally incorporated at a selenium site than at a tungsten site. The wide scan XPS spectrum for as-synthesized bulk As-doped WSe_2 crystals used in this study is displayed in **Figure 3.3.11 (b)**. In addition to W and Se related fine structures, As(3d) core energy levels are observed at 40- 43 eV as a shoulder peak with W(4f) peak (inset of **Figure 3.3.11 (b)**), although the activation efficiency of As atoms were not clear. These results suggest that the growth of As-doped WSe_2 crystal was successful. **Figure 3.3.11 (c)** shows the AFM image of an As-doped WSe_2 flake transferred onto a c-Si/$Al_{0.74}Ti_{0.26}O_y$ substrate, which thickness was estimated to be about 25 nm corresponding to the number of ~20 stacks. Hall measurement also revealed that As-doped WSe_2 showed p-type with a carrier concentration of 8.8×10^{17} cm^{-3} and mobility of 8.61 $cm^2/(V\cdot s)$.

(a)

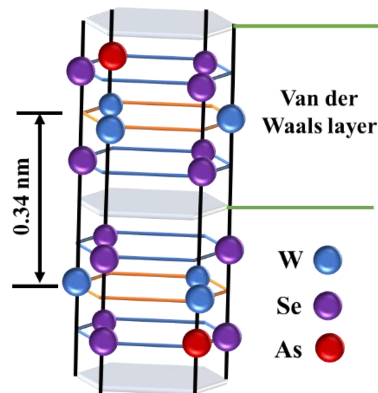

(b)

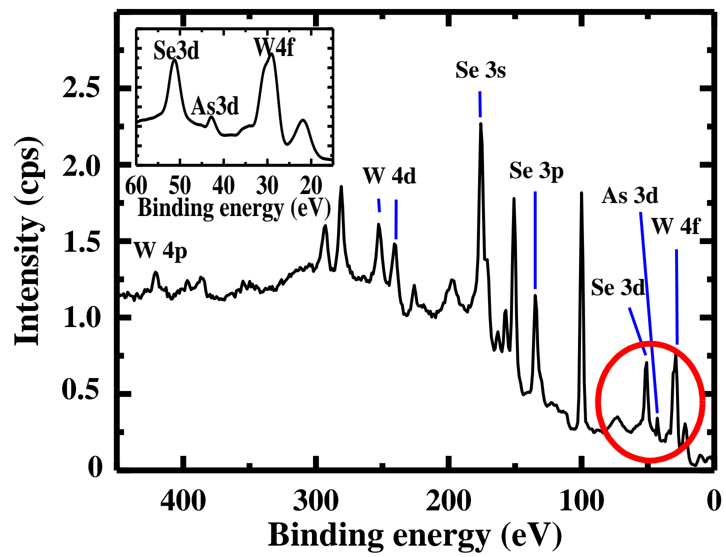

(c)

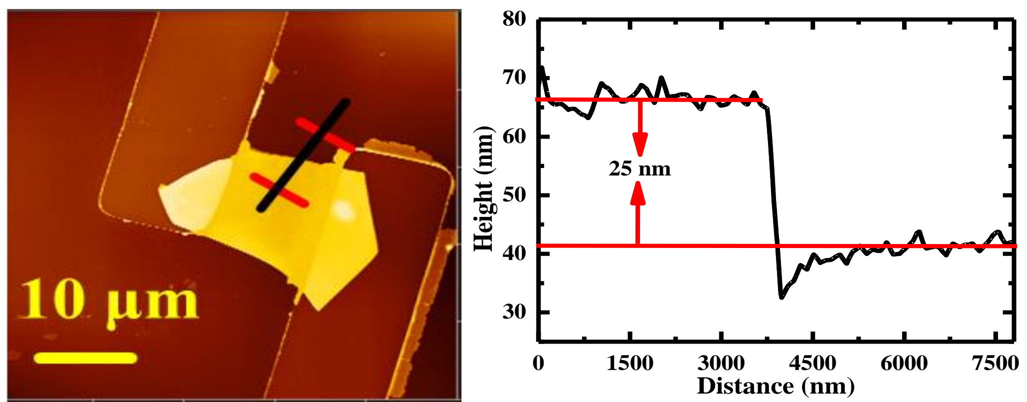

Figure 3.3. 11. (a) Crystal structure of the hexagonal shaped As-doped WSe_2 layer, (b) Wide scan XPS spectrum for as-synthesized bulk As-doped WSe_2 crystals, (c) AFM image of an As-doped WSe_2 flake transferred onto a $Al_{0.74}Ti_{0.26}O_y$/Si substrate, which thickness was estimated to be about 25 nm corresponding to the number of ~20 layers stacked.

Table 3.3. 3 Covalent bond radius and atomic radius of W, Se, and As.[3.48]

	Covalent bond radius (pm)	Atomic radius (pm)
W	162±0.7	139
Se	120±4	120
As	119±0.4	119

Figure 3.312 (a) depicts the transfer characteristics of a 25-nm-thick As-doped WSe_2 FETs on $Al_{0.74}Ti_{0.26}O_y$ as a gate dielectric layer under different V_{DS} values on linear and logarithmic scales. Platinum was used as a source and drain electrodes by radiofrequency sputtering with a channel length/length of 10.55/11.57 μm. The output characteristics of the As-WSe_2 transistor at different V_{bg} values in the positive and negative V_{DS} regimes are also illustrated in **Figures 3.3.12 (b) and (c)**. The microscopic image of the MIS-FET device is illustrated in the inset of **Figure 3.3.12 (b)**. The linear mobility, ON/OFF ratio of current and SS for N and P channel at 0.2 V_{ds} are listed in **Table 3.3.4**. An abrupt increase in I_{DS} is clearly observed in **Figure 3.3.12 (a)** with increasing V_{bg} for both positive (n-channel) and negative (p-channel) polarities, which demonstrates the ambipolar operation in the As-doped WSe_2 flake transistors. In the output characteristics, when sweeping V_{DS} from 0 to +5 V, a saturation of the current for positive gate voltage due to pinch off in the channel and a linear behavior for negative gate voltages are detected. Electrons are dominant in this regime but such a unique increase for negative gate voltage, which is not present in unipolar transistors, can be attributed to the accumulation of holes in the conducting channel and is a typical ambipolar feature. On the other side, when V_{ds} is going to scan from 0 to -5 V, a non-linear increase in current of I_{ds} are confirmed, suggesting that the transistor behavior has also appeared in this channel and holes are dominant in the negative V_{bg} regime, confirming that the type of carrier that formed the majority in the inversion layer was

not as obvious as seen in **Figure 3.3.12 (c)**. Under modulation of V_{bg}, the current on/off ratio at $V_{DS} = 0.2$ V reaches 8×10^3 and 5×10^3 for the n- and p-type regimes, respectively, fulfilling the requirements for use as a switch.[3.49,3.50] The extracted mobilities were 6.3 and 5.7 $cm^2V^{-1}s^{-1}$ for n and p channels, respectively. Those mobilities were compatible with the theoretical prediction in the literature,[3.51] implying the existence of small contact resistance in the layered WSe_2 transistors due to high work function metal Pt was used as the contact.

(a)

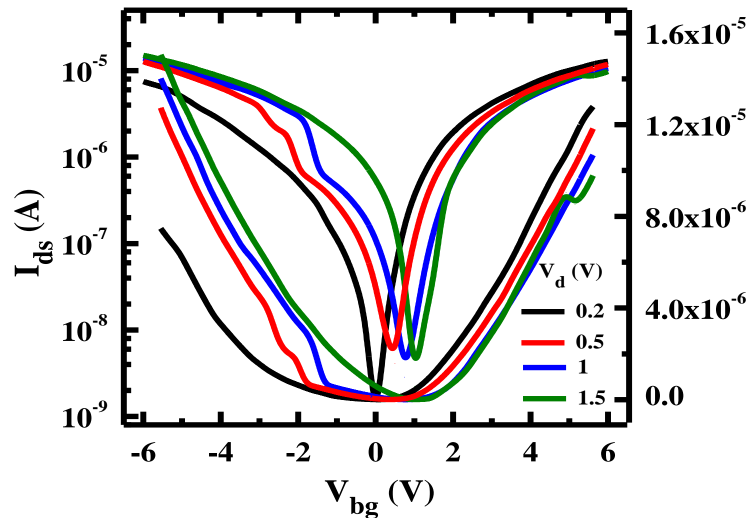

(b)

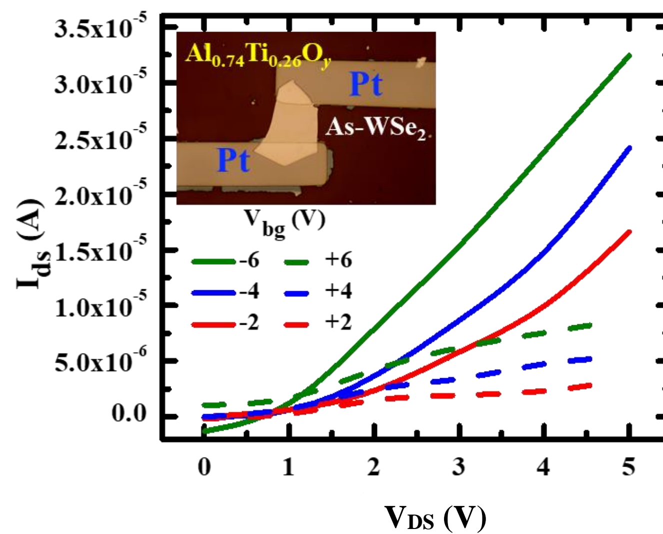

(c)

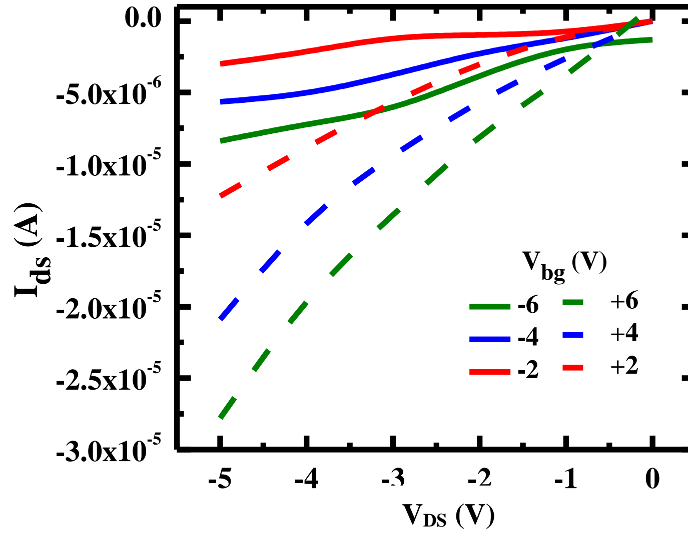

Figure 3.3. 12. (a) Transfer characteristics of a 25-nm-thick As-doped WSe_2 transistor under different V_{DS} values on a linear and a logarithmic scale, Output characteristics of the As-doped WSe_2 transistors under different V_{DS} values in the positive V_{DS} regime (b) and in the negative V_{DS} regime (c).

Table 3.3. 4 Electrical characteristics of As-doped WSe_2 based ambipolar MIS-FET where $Al_{0.74}Ti_{0.26}O_y$ used as dielectric layer.

SS (V/dec)		I_{ON}/I_{OFF}		μ_{lin} ($cm^2V^{-1}s^{-1}$)	
n	P	n	P	n	P
0.35	0.65	$7X10^3$	$4X10^3$	6.3	5.7

Figure 3.3.13 (a) shows the circuit diagram for the inverter by cascading two ambipolar MIS-FET using As-doped WSe_2 as a channel layer with a common gate as the input voltage, V_{IN}. When a positive V_{DD} and V_{IN} are applied, the inverter works in the positive V_{OUT} regime (1st quadrant). Under these circumstances, the ambipolar transistor, FET1 operates as a p-type channel, whereas the FET2 conducts as an n-type channel (**Figure 3.3.13 (b)**). As V_{DD} and V_{IN} are applied negatively without any alternation of the circuit formation, the inverter works in the negative V_{OUT} regime (3rd quadrant), as shown in **Figure 3.3.13 (c)**. The corresponding voltage gains, defined as

$\Delta V_{OUT}/\Delta V_{IN}$, at various V_{DD} are displayed as a function of V_{IN} in **Figure 3.3.13 (d)**. The two peak positions rise at the about same level demonstrating that both electrons and holes are equally contributed in the ambipolar transistor. These findings provide that mist CVD $Al_{0.74}Ti_{0.26}O_y$ has great potential as the gate dielectric layer for MIS-FETs using 2D WSe_2 flake as a channel layer.

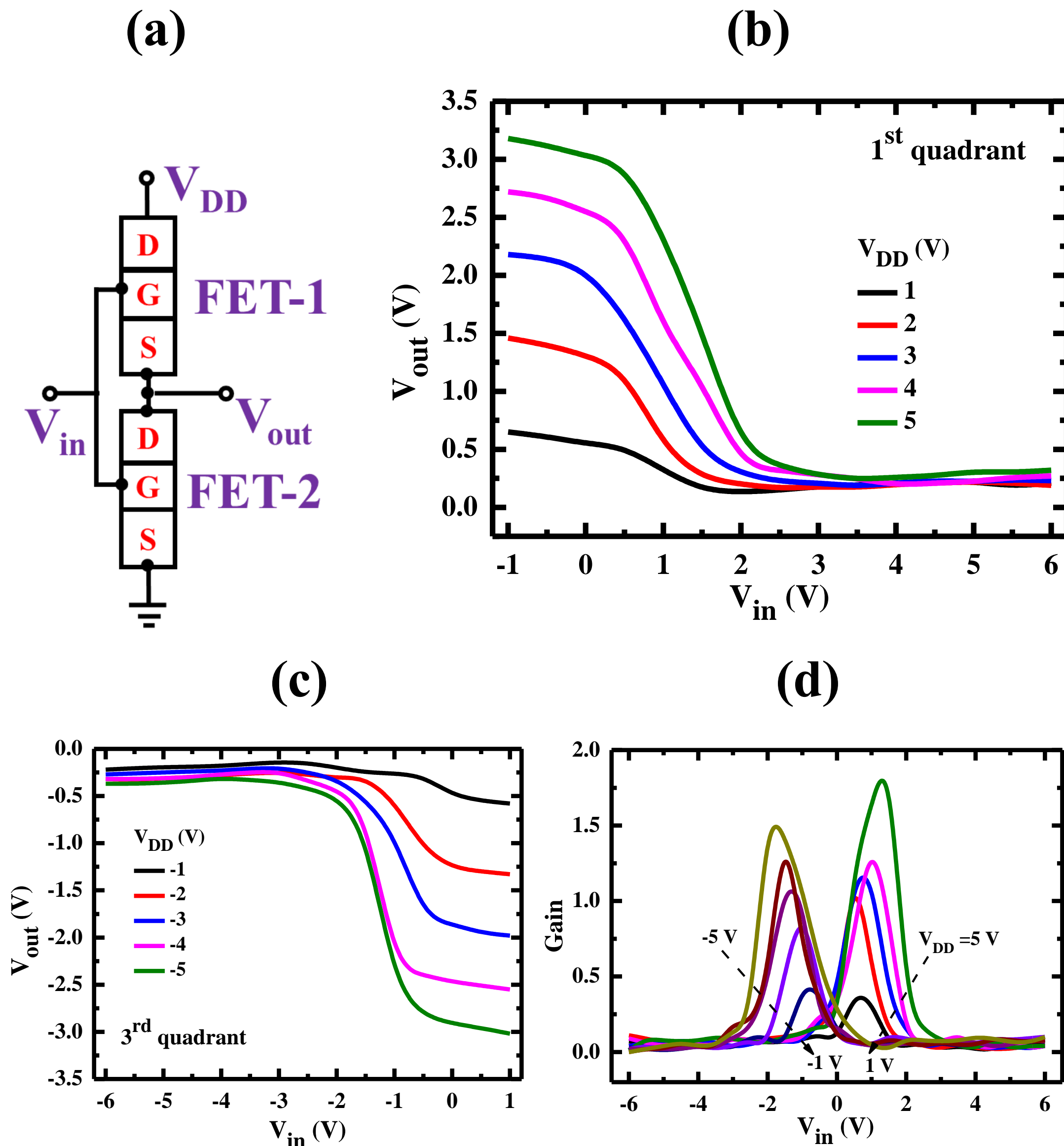

Figure 3.3. 13. (a) Schematic of a complementary inverter circuit comprising two ambipolar transistors, one which operated as an n-type channel transistor whereas the other was conducted as a p-channel transistor. (b) Inverter characteristics where V_{IN} and V_{DD} were both positively biased (1st quadrat), (c) Inverter characteristics where V_{IN} and V_{DD} were both negatively biased (3rd quadrat). (d) The corresponding voltage gain of the complementary inverter ($\Delta V_{OUT}/ \Delta V_{IN}$).

References

3.1 Kawaharamura, T.; Uchida, T.; Sanada, M.; and Furuta, M. "Growth and electrical properties of AlO_x grown by mist chemical vapor deposition", *AIP Adv.*3, 032135, (2013).

3.2 Katamreddy, R.; Inman, R.; Jursich, G.; Soulet, A.; and Takoudis, C. "The Electrochemical Society, find out more ALD and Characterization of Aluminum Oxide Deposited on Si (100) using Tris(diethylamino) Aluminum and Water Vapor", *J. Electrochem. Soc.*153(10), C701, (2006).

3.3 Chowdhuri, A. R.; Takoudis, C. G.; Klie, R. F.; and Browning, N. D. "Metalorganic chemical vapor deposition of aluminum oxide on Si: Evidence of interface SiO_2 formation", *Appl. Phys. Lett.* **80(22)**, 4241, (2002).

3.4 Tarte, P. "Infra-red spectra of inorganic aluminates and characteristic vibrational frequencies of AlO_4 tetrahedra and AlO_6 octahedra", Spectrochim. Acta Part A: **23(7)**, 2127, (1967).

3.5 Morterra C.; and Magnacca, G. "A case study: surface chemistry and surface structure of catalytic aluminas, as studied by vibrational spectroscopy of adsorbed species", *Catal. Today* **27(3)**, 497, (1996).

3.6 Dillon, A. C.; Ott, A. W.; Way, J. D.; and George, S. M. "Surface chemistry of Al_2O_3 deposition using $Al(CH_3)_3$ and H_2O in a binary reaction sequence", *Surf. Sci.* **322(1)**, 230, (1995).

3.7 Li, T.-T. A.; Ruffell, S.; M. Tucci, Mansoulie, Y.; Samundsett, C.; De Iuliis, S.; Serenelli, L.; and Cuevas, A. "Influence of oxygen on the sputtering of aluminum oxide for the surface passivation of crystalline silicon", *Sol. Energy Mater. Sol. Cells* **95(1)** 69-72, (2011).

3.8 Bulkin, P. V.; Swart, P. L.; and Lacquet, B. M.; "Electron cyclotron resonance plasma enhanced chemical vapour deposition and optical properties of SiO_x thin films", *J. Non-Cryst. Solids* **226(1)**, 58, (1998).

3.9 Yi, L. X.; J. Heitmann, Scholz, R.; and Zacharias, M. "Phase separation of thin SiO layers in amorphous SiO/SiO_2 superlattices during annealing", *J. Phys.: Condens. Matter* **15**, S2887, (2003).

3.10 Wang, ZY.; Zhang, RJ.; Lu, HL.; Chen, X.; Sun, Y.; Zhang, Y.; Wei, YF.; JP. Xu, Wang, SY.; Zheng, YX.; and Chen, LY. "The impact of thickness and thermal

annealing on refractive index for aluminum oxide thin films deposited by atomic layer deposition", *Nanoscale Research Letters* **10(1)**, 46, (2015).

3.11 Kumar, P.; Wiedmann, M. K.; Winter, C. H.; and Avrutsky, I. "Optical properties of Al2O3 thin films grown by atomic layer deposition" *Appl. Optics* **48(28)**, 5407-5412, (2015).

3.12 Atkins, P. *"Atkins' Physical Chemistry"*, Oxford University Press, (2006), ISBN: 9780198700722,0198700725.

3.13 Lale, A.; Scheid, E.; Cristiano, F.; Datas, L.; Reig, B.; Launay, J.; and Temple-Boyer, P. "Study of aluminium oxide thin films deposited by plasma-enhanced atomic layer deposition from tri-methyl-aluminium and dioxygen precursors: Investigation of interfacial and structural properties", *Thin Solid Films* **666**, 20-27, (2018).

3.14 Miyajima, S.; Irikawa, J.; Yamada, A.; and Konagai, M. "High Quality Aluminum Oxide Passivation Layer for Crystalline Silicon Solar Cells Deposited by Parallel-Plate Plasma-Enhanced Chemical Vapor Deposition", *Appl. Phys. Express* **3**, 012301, (2010).

3.15 Hoex, B.; Schmidt, J.; Pohl, P.; van de Sanden, M. C.M.; and Kessels, W. M. M. "Silicon surface passivation by atomic layer deposited Al_2O_3", *J. Appl. Phys.* **104**, 044903, (2008).

3.16 Wu, S. Y.; Hong, M.; A. R. Kortan, A.; Kwo, J.; Mannaerts, J. P.; Lee, W. C.; and Huang, Y. L. "High-quality thin single-crystal γ-Al_2O_3 films grown on Si (111)" *Appl. Phys. Lett.* **87**, 091908, (2005).

3.17 Sze S. M.; and Ng, K. K. Physics of Semiconductor Devices. (*Wiley*, 2006).

3.18 Kolodzey, J.; Chowdhury, E. A.; Adam, T. N.; Qui, G.; Rau, I.; Olowolafe, J. O.; Suehle, J. S.; and Chen, Y. "Electrical conduction and dielectric breakdown in aluminum oxide insulators on silicon", *IEEE Transactions on Electron Devices* **47(1)**, 121-128, (2000).

3.19 Ito, T.; Matsumoto, T.; and Nishioka, K. "Improvement of electrical properties of silicon oxide thin film with ultraviolet and organic gas assisted annealings", *Surf. Coatings Technol.* **215**, 447, (2013).

3.20 Uchida, T.; Kawaharamura, T.; Shibayama, K.; Hiramatsu, T.; Orita, H.; and Fujita, S. "Mist chemical vapor deposition of aluminum oxide thin films for rear surface passivation of crystalline silicon solar cells", *Appl. Phys. Express* **7**, 021303, (2014).

3.21 Kumar, P.; Wiedmann, M. K.; Winter, C. H.; Avrutsky, I. "Optical Properties of Al_2O_3 Thin Films Grown by Atomic Layer Deposition", *Appl. Opt.* 48, 5407, (2015).

3.22 Maruyama, T.; Arai, S. "Aluminum Oxide Thin Films Prepared by Chemical Vapor Deposition from Aluminum Acetylacetonate", *Appl. Phys. Lett.* 60(3), 322-323, (1992).

3.23 Devi, A.; Shivashankar' S. A.; Samuelson' A. G. "MOCVD of Aluminium Oxide Films Using Aluminium P-diketonates as Precursors", J. *Phys. IV France* **12**, 139-146, (2002).

3.24 Rutthongjan, P.; Nishi M.; Liu, L.; Sato, S.; Okada, Y.; Dang, G.; Kawaharamura T. "Growth Mechanism of Zinc Oxide thin Film by Mist Chemical Vapor Deposition via the Modulation of [H_2O]/[Zn] Ratios", *Appl. Phys. Express* **12**, 065505, (2019).

3.25 Ohki, T.; Ichikawa, K.; Hossain, J.; Fujii, Y.; Hanajiri, T.; Ishikawa, R.; Ueno, K.; Shirai, H. "Effect of Substrate Bias on Mist Deposition of Conjugated Polymer on Textured Crystalline-Si for Efficient c-Si/Organic Heterojunction Solar Cells", *Phys. Status Solidi A*, **213(7)**, 1922-1925, (2016).

3.26 Gao, J.; Hao, M.; Li, W.; Xu, Z.; Mandal, S.; Nemanich, R.; Chowdhury, S. "Al_2O_3Insertion Layer for Improved PEALD SiO_2/(Al)GaN Interfaces", *Phys. Status Solidi A*, 215, 1700498, (2018).

3.27 Ren, B; Sumiya, M.; Liao, M.; Koide, Y.; Liu, X.; Shen, Y.; Sang, L. "Interface Trap Characterization of Al_2O_3/GaN Vertical-Type MO Capacitors on GaN Substrate with Surface Treatments", *Journal of Alloys and Compounds*, 767, 600-605, (2018).

3.28 Wang, Y; Wang, H.; Ye, C.; Zhang, J.; Wang, H.; Jiang, Y. "Interfacial Reaction and Electrical Properties of HfO_2 Film Gate Dielectric Prepared by Pulsed Laser Deposition in Nitrogen: Role of Rapid Thermal Annealing and Gate Electrode", *ACS Appl. Mater. Interfaces* **3**, 3813-3818, (2011).

3.29 Puźniaka, M.; Gajewskib, W.; Żelechowskib, M.; Jamrozc, J.; Gertychc, A.; Zdrojekc, M.; Mroczyńskia, R. "Technology and Optimization of Hafnium Oxynitride (HfOxNy) Thin-Films Formed by Pulsed-DC Reactive Magnetron Sputtering for MIS Devices", *Microelectronic Engineering* **228**, 111332, (2020).

3.30 Agostinelli, G.; Delabie, A.; Vitanov, P.; Alexieva, Z.; Dekkers, H.; Wolf, S. D.; Beaucarne, G. "Very Low Surface Recombination Velocities on P-type Silicon

Wafers Passivated with a Dielectric with Fixed Negative Charge", *Sol. Energy Mater. Sol. Cells* **90**, 3438-3443, (2006).

3.31 Werner, F.; Schmidt, J. "Manipulating the Negative Fixed Charge Density at the c-Si/Al_2O_3 Interface", *Appl. Phys. Lett.* **104**, 091604, (2006).

3.32 Hoex, B.; Gielis, J. J. H.; van de Sanden, M. C. M.; Kessels, W. M. M. "On the c-Si Surface Passivation Mechanism by the Negative-Charge-Dielectric Al_2O_3", *J. Appl. Phys.* **104**, 113703, (2008).

3.33 Lucovsky, G. "A Chemical Bonding Model for the Native Oxides of the III–V Compound Semiconductors", *J. Vac. Sci. Technol.* **19**, 456, (1981).

3.34 Boukhili, W.; Mahdouani, M.; Erouel, M.; Puigdollers, J.; Bourguiga, R. "Reversibility of Humidity Effects in Pentacene Based Organic Thin-film Transistor: Experimental Data and Electrical Modeling", *Synthetic Metals* 199, 3003-309, (2015).

3.35 Jeong, S. H.; Liu, N.; Park, H.; Hong, Y. K.; Kim, S. "Temperature-Dependent Electrical Properties of Al_2O_3-Passivated Multilayer MoS_2 Thin-Film Transistors", *Appl. Sci.* 8, 424, (2018).

3.36 Pradhan, N. R.; Rhodes, D.; Xin, Y.; Memaran, S.; Bhaskaran, L.; Siddiq, M.; Hill, S.; Ajayan, P. M.; Balicas, L. "Ambipolar Molybdenum Diselenide Field-Effect Transistors: Field-Effect and Hall Mobilities", *ACS Nano* **8(8)**, 7923-7929, (2014).

3.37 Kim, S.; Konar, A.; Hwang, W. -S.; Lee, J. H.; Lee, J.; Yang, J.; Jung, C.; Kim, H.; Yoo, J.; Choi, J. -Y.; Jin, Y. W.; Lee, S. Y.; Jena, D.; Choi, W.; Kim, K. "High-Mobility and Low-power Thin-Film Transistors Based on Multilayer MoS_2", *Crystals. Nat. Commun.* **3**, 1011, (2012).

3.38 Pradhan, N. R.; Rhodes, D.; Feng, S.; Xin, Y.; Memaran, S.; Moon, B. -H.; Terrones, H.; Terrones, M.; Balicas, L. "Field-Effect Transistors Based on Few-Layered α-$MoTe_2$", *ACS Nano* **8(6)**, 5911-5920, (2014).

3.39 Rajib, A.; Enamul, K. M.; Kurosu, S.; Ukai, T.; Tokuda, M.; Fujii, Y.; Hanajiri, T.; Ishikawa, R.; Ueno, K.; Shirai, H. "Synthesis of AlO_x Thin Films by Atmospheric-Pressure Mist Chemical Vapor Deposition for Surface Passivation and Electrical Insulator Layers", *J. Vac. Sci. Technol. A 38* **(3)**, 033413, (2020).

3.40 Mahata, C.; Mallik, S.; Das, T.; Maiti, C. K.; Dalapati, G. K.; Tan, C. C.; Chia, C. K.; Gao, H.; Kumar, M. K.; Chiam, S. Y.; Tan, H. R.; Seng, H. L.; Chi, D. Z.; Miranda, E. "Atomic Layer Deposited $(TiO_2)_x(Al_2O_3)_{1-x}/In_{0.53}Ga_{0.47}As$ Gate

Stacks for III-V Based Metal-Oxide-Semiconductor Field-Effect Transistor Applications", *Appl. Phys. Lett.* **100 (6)**, 2–6, (2012).

3.41 Shang, D. S.; Chen, L. D.; Wang, Q.; Yu, W. D.; Li, X. M.; Sun, J. R.; Shen, B. G. "Crystallinity Dependence of Resistance Switching in $La_{0.7}Ca_{0.3}MnO_3$ Films Grown by Pulsed Laser Deposition", *J. Appl. Phys.* **105**, 063511, (2009).

3.42 Yang, W.; Song, K.; Jung, Y.; Jeong, S.; Moon, J. "Solution-Deposited Zr-Doped AlO_x Gate Dielectrics Enabling High-Performance Flexible Transparent Thin Film Transistors", *J. Mater. Chem. C* **1 (27)**, 4275–4282, (2013).

3.43 Wang, H.; Xu, W.; Zhou, S.; Xie, F.; Xiao, Y.; Ye, L.; Chen, J.; Xu, J. "Oxygen Plasma Assisted High Performance Solution-Processed Al_2O_3 Gate Insulator for Combustion-Processed $InGaZnO_x$ Thin Film Transistors", *J. Appl. Phys.* **117 (3)**, 1–10, (2015).

3.44 Koslowski, N.; Sanctis, S.; Hoffmann, R. C.; Bruns, M.; Schneider, J. J. "Synthesis Dielectric Properties and Application in a Thin Film Transistor Device of Amorphous Aluminum Oxide Al_xO_y Using a Molecular Based Precursor Route", *J. Mater. Chem. C* **7 (4)**, 1048–1056, (2019).

3.45 Zan, H. W.; Yeh, C. C.; Meng, H. F.; Tsai, C. C.; Chen, L. H. "Achieving High Field-Effect Mobility in Amorphous Indium-Gallium-Zinc Oxide by Capping a Strong Reduction Layer", *Adv. Mater.* **24 (26)**, 3509–3514, (2012).

3.46 Luo, Y.-R. "*Comprehensive Handbook of Chemical Bond Energies",* CRC Press, 1–1687 (2002).

3.47 Ganguly, S.; Verma, J.; Li, G.; Zimmermann, T.; Xing, H.; Jena, D. "Presence and Origin of Interface Charges at Atomic-Layer Deposited Al_2O_3/III-Nitride Heterojunctions", *Appl. Phys. Lett.* **99 (19)**, 2009–2012, (2011).

3.48 Slater, J. C. "Atomic Radii in Crystals", *J. Chem. Phys.* 41, 3199, (1964).

3.49 Lin, Y. F.; Xu, Y.; Wang, S. T.; Li, S. L.; Yamamoto, M.; Aparecido-Ferreira, A.; Li, W.; Sun, H.; Nakaharai, S.; Jian, W. Bin; Ueno, K.; Tsukagoshi, K. "Ambipolar $MoTe_2$ Transistors and Their Applications in Logic Circuits", *Adv. Mater.* **26 (20)**, 3263–3269, (2014).

3.50 Schwierz, F. "Graphene Transistors", *Nat. Nanotechnol.* **5 (7)**, 487–496, (2010).

3.51 Mukherjee, R.; Chuang, H. J.; Koehler, M. R.; Combs, N.; Patchen, A.; Zhou, Z. X.; Mandrus, D. "Substitutional Electron and Hole Doping of WSe_2: Synthesis, Electrical Characterization, and Observation of Band-to-Band Tunneling", *Phys. Rev. Appl.* **7**, 034011, (2017).

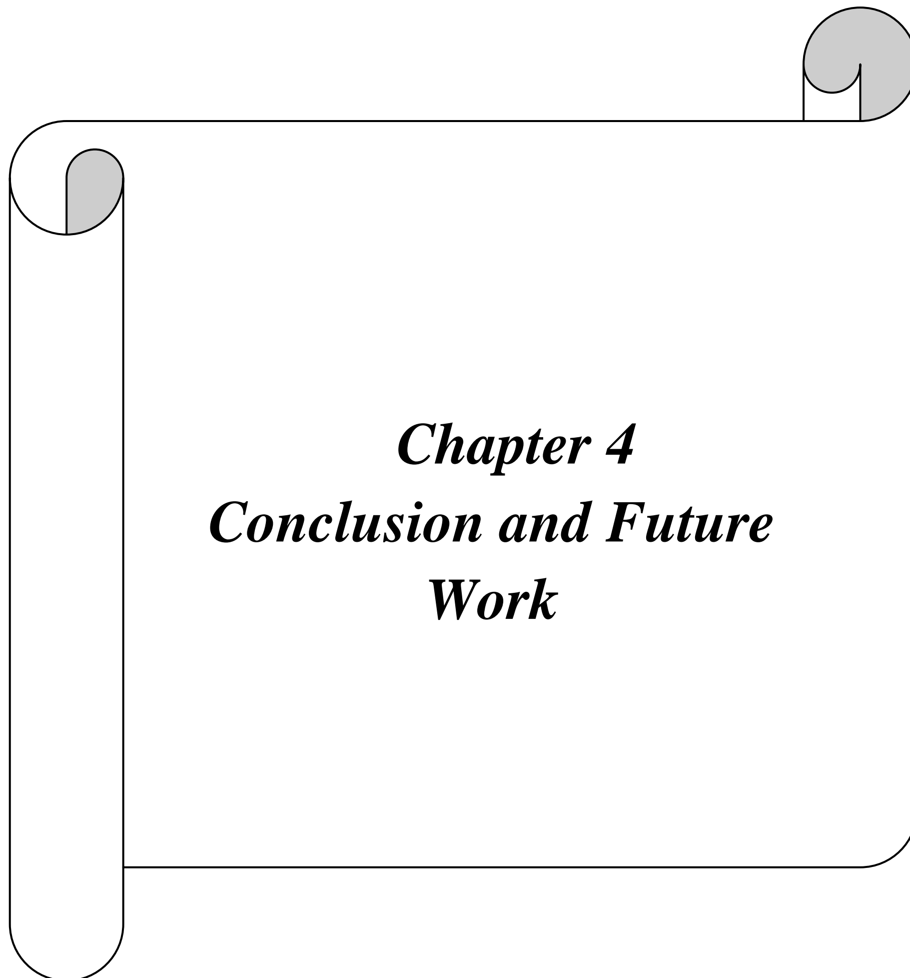
Chapter 4
Conclusion and Future
Work

Chapter 4: Conclusion and Future Work

4.1 Summary of Results

In this thesis, AlO_x based thin films by mist-CVD have been synthesized and applied as a gate insulating layer in the field-effect transistor. To understand the film properties of AlO_x thin film, the deposition parameters, including $CH_3OH:H_2O$ ratio, N_2 flow rate F_d, tabular furnace temperature T_f, mesh bias supply V_m, were optimized via the analysis of the size distribution of mist precursors using a fast scanning mobility particle analyzer. To improve the dielectric properties, TiO_2 was added with AlO_x and resulting in a higher dielectric constant was obtained by adjusting the Ti compositional ratio of 0.26. The key contributions of this work are as follows:

1. **Effect of H_2O in the synthesis of amorphous AlO_x using mist-CVD**

This work studied the effects of adding H_2O during the deposition of AlO_x thin films via mist-CVD. The $CH_3OH:H_2O$ ratio during the deposition was varied and films were also subjected to both H_2O and CH_3OH mists after fabrication. Both the density and uniformity of AlO_x thin films were improved markedly by adjusting the $CH_3OH:H_2O$ ratio with concurrent decreases in the surface roughness. The addition of H_2O during the mist-CVD of AlO_x was found to suppress the deposition rate and to promote the removal of -OH groups on the growth surface. The AlO_x with CH_3OH solvent alone includes a large amount of OH bond near the growing surface rather than the octahedral and tetrahedral AlO_x complexes. They induce surface roughness because a sticking process is dominant rather than the removal of OH bond. On the other hand, the H_2O mist scavenges the OH bond efficiently during the growth, resulting in that the octahedral and tetrahedral AlO_x complexes are formed preferentially. These results imply that H_2O mists act as a scavenger of OH bond near the growing surface. This effect, in turn, affected the extent of passivation of the Si surface, The mist-CVD of AlO_x in conjunction with $CH_3OH:H_2O$ ratio of 7:3 resulted in a highly effective minority carrier lifetime, τ_{eff}, of 718 μs, a low recombination velocity, S_{eff}, of 16 cm/s, a high breakdown field, E_{BD}, of 6.9 MV/cm and a low interface density, D_{it}, of 10^{10} $cm^{-2}eV^{-1}$. These values were close to those reported for AlO_x synthesized using ALD and PE-CVD.

2. Improve the film properties of mist-CVD deposited AlO_x thin films by optimizing the deposition parameters monitored by a fast-scanning mobility particle analyzer

In this section, the correlations among the size distribution of charged mist particles, the deposition parameters, and film properties, including junction properties at the AlO_x/n-Si interface were investigated. The correlation was studied for AlO_x thin films produced by mist-CVD via analysis of the size distribution of the mist precursors using a fast-scanning mobility particle analyzer. The findings are assembled as follows:

a) AlO_x thin film having higher *n* value with smaller surface roughness was obtained by optimizing the deposition parameters; 0.015mol/L $Al(acac)_3$, F_d of 2400 sccm, and T_f of 550 °C.

b) Further, mesh bias V_m supply during film growth effectively increased the *n*-value of AlO_x thin films by suppressing their surface roughness and improving the junction properties at the AlO_x/n-Si interface.

c) AlO_x thin films having a highly rigid network and small surface roughness were obtained at a deposition rate of 3.9 nm/min by adjusting the deposition parameters with a V_m of 9 kV.

d) A FET mobility of 41.4 cm^2/Vs was obtained with a V_{th} of 2.75 V, SS of 0.24 V/dec, and an on/off current ratio of ~10^7 for a ~50 nm thick AlO_x layer were obtained by adjusting the mesh bias supply to 9 kV.

e) Finally, the film properties of AlO_x and its junction properties at the AlO_x/n-Si interface were determined by the size distribution of the mist precursor.

These findings imply that AlO_x thin films synthesized through mist-CVD using fine mist particles by adjusting V_m are promising for the gate insulators for FETs.

3. Effect of Ti acetylacetonate addition on the synthesis of mist chemical vapor deposited $Al_{1-x}Ti_xO_y$ thin films

Further improvement of dielectric properties of AlO_x thin films, Ti acetylacetonate were added in this topic. Effect of additive TiO_2 precursor in the growth of the mist-CVD $Al_{1-x}Ti_xO_y$ thin films from $Al(acac)_3$ precursor solution using CH_3OH/H_2O (7:3)

as a solvent and on the junction property at the $Al_{1-x}Ti_xO_y$/n-Si interface has been investigated. The Ti composition ratio in the $Al_{1-x}Ti_xO_y$ thin films was controlled by tuning $Ti(acac)_4$/$Al(acac)_3$ and CH_3OH/H_2O ratios. The MIS-FETs that use mechanically exfoliated $MoSe_2$ flakes with a gold S/D electrode on $Al_{0.74}Ti_{0.26}O_y$ as a gate dielectric layer exhibited a FET mobility of 85 cm^2/Vs with a lower threshold voltage (0.92 V) and a higher on/off current ratio (~ 10^6). The leak current for MIS-FETs was suppressed efficiently for $Al_{0.74}Ti_{0.26}O_y$ thin films with bandgap energy (5.12 eV) and a dielectric constant (13.8). Ambipolar behavior of I_{DS}-V_g was observed for MIS-FETs with As-doped WSe_2 flake as a channel layer with platinum S/D electrodes. The tunability of these WSe_2-based ambipolar transistors is suitable for use in logic applications. These findings imply that $Al_{0.74}Ti_{0.26}O_y$ thin films by mist CVD act as a gate dielectric layer of 2D semiconducting 2D metal chalcogenide-based MIS-FETs.

4.2 Future Work

The MIS-FET performance mainly depends on the interface properties $Al_{1-x}Ti_xO_y$ / n-Si interface and the film properties of $Al_{1-x}Ti_xO_y$ thin film. Mist-CVD deposited amorphous AlO_x is a model substance as a dielectric layer in the MIS-FET. A set of possible approaches to improve the dielectric properties of mist-CVD AlO_x and to understand the junction properties of MOS capacitor, as well as MIS-FET, are as follows:

a) We have studied the junction properties of the $Al_{1-x}Ti_xO_y$ / n-Si interface. But to obtain the improved performance of MIS-FET, $Al_{1-x}Ti_xO_y$ /$MoSe_2$/As-doped WSe_2 interface should be taken into account.
b) In this study, the mechanically exfoliated $MoSe_2$/As-doped WSe_2 was used as a channel layer. The atomic/bi-layer of $MoSe_2/MoS_2$ is another approach to improve the performances of FETs and MOS inverter. Our group member A. Kuddus has been already concentrated on mist-CVD deposited MoS_2-based MIS-FET fabrication on $Al_{1-x}Ti_xO_y$/P++-Si substrate.
c) As mist-CVD is an open-air deposition system, the impurity may come from the air XPS study is crucial to understand the impurity concentration in the $Al_{1-x}Ti_xO_y$ thin films.

d) The dielectric properties of $Al_{1-x}Ti_xO_y$ thin film can be further improved by analyzing the structural properties of $Al_{1-x}Ti_xO_y$ thin film.
e) Introducing the mist-CVD deposited capping layer of metal oxide is another approach to improve the MOS-FET performance.